

AD-A241 298



2

EFFECTS OF WAVES ON THE WAKE OF A
SURFACE-PIERCING FLAT PLATE: EXPERIMENT AND THEORY

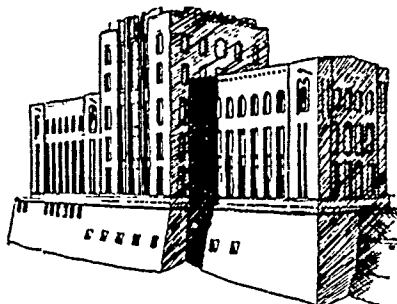
by

F. Stern, J. E. Choi, and W. S. Hwang

Sponsored by

Office of Naval Research
Contract No. N00014-88-K-0113

DTIC
SELECTED
OCT. 03 1991
S B D



91-12092



Original contains color
plates. All DTIC reproductions
will be in black and
white.

IIHR Report No. 353

Iowa Institute of Hydraulic Research
The University of Iowa
Iowa City, Iowa 52242

August 1991

Approved for Public Release: Distribution Unlimited

01 1 071

**EFFECTS OF WAVES ON THE WAKE OF A
SURFACE-PIERCING FLAT PLATE: EXPERIMENT AND THEORY**

by

F. Stern, J. E. Choi, and W. S. Hwang

Sponsored by

Office of Naval Research
Contract No. N00014-88-K-0113

IIHR Report No. 353

Iowa Institute of Hydraulic Research
The University of Iowa
Iowa City, Iowa 52242

August 1991

Approved for Public Release: Distribution Unlimited

SECURITY CLASSIFICATION OF THIS PAGE (When Data Entered)

REPORT DOCUMENTATION PAGE		READ INSTRUCTIONS BEFORE COMPLETING FORM
1. REPORT NUMBER IIHR Report No. 353	2. GOVT ACCESSION NO.	3. RECIPIENT'S CATALOG NUMBER
4. TITLE (and Subtitle) Effects of Waves on the Wake of a Surface-Piercing Flat Plate: Experiment and Theory		5. TYPE OF REPORT & PERIOD COVERED Technical Report
		6. PERFORMING ORG. REPORT NUMBER IIHR Report No. 353
7. AUTHOR(s) F. Stern, J.E. Choi, and W.S. Hwang		8. CONTRACT OR GRANT NUMBER(s) N00014-88-K-0113
9. PERFORMING ORGANIZATION NAME AND ADDRESS Iowa Institute of Hydraulic Research The University of Iowa Iowa City, IA 52242-1585		10. PROGRAM ELEMENT, PROJECT, TASK AREA & WORK UNIT NUMBERS 4322804
11. CONTROLLING OFFICE NAME AND ADDRESS Office of Naval Research 800 N. Quincy Arlington VA 22217		12. REPORT DATE August 1991
		13. NUMBER OF PAGES 118
14. MONITORING AGENCY NAME & ADDRESS (if different from Controlling Office) ONR Resident Representative Seattle WA 98105-4631		15. SECURITY CLASS. (of this report) Unclassified
		15a. DECLASSIFICATION/DOWNGRADING SCHEDULE
16. DISTRIBUTION STATEMENT (of this Report) Approved for Public Release; Distribution Unlimited		
17. DISTRIBUTION STATEMENT (of the abstract entered in Block 20, if different from Report)		
18. SUPPLEMENTARY NOTES		
19. KEY WORDS (Continue on reverse side if necessary and identify by block number) Wave/wake interaction Wave-induced separation Three-dimensional viscous/free-surface flow Computational fluid dynamics		
20. ABSTRACT (Continue on reverse side if necessary and identify by block number) Results are presented from a towing-tank experiment conducted in order to document the effects of waves on the wake of a surface-piercing body. A unique, simple model geometry is utilized which makes it possible to isolate and identify the most important features of the wave-induced effects. Measurements were made for three wave-steepness conditions: zero, medium, and large. The effects of the waves for the latter two conditions are shown to be significant. In particular, the variations of the external-flow pressure gradients		

cause acceleration and deceleration phases of the streamwise velocity component and alternating direction of the crossflow, which results in large oscillations of the displacement thickness and wake centerplane velocities as compared to the zero-steepness condition. Remarkably, the wake displays a greater response, i.e., a bias with regard to favorable as compared to adverse pressure gradients. The measurements are compared and close agreement is demonstrated with results from Reynolds-averaged Navier-Stokes calculations. Additional calculations are presented, including laminar-flow results, which aid in explicating the characteristics of the near and intermediate wake, the periodic nature of the far wake, and wave-induced separation. Previously, experimental and computational results were presented for the boundary-layer region.



Accession For	
NTIS GRA&I	<input checked="" type="checkbox"/>
DTIC TAB	<input type="checkbox"/>
Unannounced	<input type="checkbox"/>
Justification	
By _____	
Distribution/	
Availability Codes	
Dist	Avail and/or Special
A-1	

TABLE OF CONTENTS

ABSTRACT.....	ii
ACKNOWLEDGEMENTS	ii
LIST OF SYMBOLS.....	iii
I. INTRODUCTION.....	1
II. EXPERIMENTAL EQUIPMENT AND PROCEDURES	2
A. Model Geometry.....	3
B. Instrumentation	3
C. Calibration.....	4
D. Data-Acquisition System	6
E. Experimental Procedure	6
F. Experimental Uncertainty.....	7
III. COMPUTATIONAL METHOD	8
A. Approach.....	8
B. Computational Grids and Conditions	10
IV. EXPERIMENTAL AND COMPUTATIONAL RESULTS	12
A. Wave Elevations.....	12
B. Velocity Profiles.....	13
1. Without Plate.....	14
2. Zero Steepness.....	15
3. Large Steepness.....	19
4. Medium Steepness.....	25
C. Some Additional Computational Results	25
1. Turbulent Flow	26
2. Laminar Flow	29
V. CONCLUDING REMARKS.....	33
REFERENCES	36
FIGURES	40

ABSTRACT

Results are presented from a towing-tank experiment conducted in order to document the effects of waves on the wake of a surface-piercing body. A unique, simple model geometry is utilized which makes it possible to isolate and identify the most important features of the wave-induced effects. Measurements were made for three wave-steepness conditions: zero, medium, and large. The effects of the waves for the latter two conditions are shown to be significant. In particular, the variations of the external-flow pressure gradients cause acceleration and deceleration phases of the streamwise velocity component and alternating direction of the crossflow, which results in large oscillations of the displacement thickness and wake centerplane velocities as compared to the zero-steepness condition. Remarkably, the wake displays a greater response, i.e., a bias with regard to favorable as compared to adverse pressure gradients. The measurements are compared and close agreement is demonstrated with results from Reynolds-averaged Navier-Stokes calculations. Additional calculations are presented, including laminar-flow results, which aid in explicating the characteristics of the near and intermediate wake, the periodic nature of the far wake, and wave-induced separation. Previously, experimental and computational results were presented for the boundary-layer region.

ACKNOWLEDGEMENTS

This research was sponsored by the Office of Naval Research under Contract N00014-88-K-0113 under the administration of Dr. E. P. Rood whose support and helpful technical discussions are greatly appreciated. Special thanks are also given to Professors Suzuki and Tanaka, Osaka University, for their kind loan of the five-hole pitot and servo-mechanism wave probes. The assistance of Dr. Y. Toda in performing the five-hole pitot probe calibration and the wave-elevation measurements, and the IIHR mechanical and electronic shops, especially J. Goss and D. Houser, were invaluable. The first author gratefully acknowledges the gracious and generous hospitality of Professor G. Federici, Il Direttore, and his colleagues of the Dipartimento Di Ingegneria Civile, Università Degli Studi Di Firenze during the time of his sabbatical and the completion of this report.

LIST OF SYMBOLS

English

Ak	wave steepness
b	wake half width
c	foil chord length, calibration constant
C_p	pressure coefficient $[= 2(p - p_o)/\rho U_c^2]$
C,T,B,P,S	probe holes
d	foil depth of submergence
Fr	Froude number $(= U_c/\sqrt{gL})$
g	gravitational acceleration
H	shape parameter
$H_{C,T,B,P,S}$	probe-hole pressures
imax	total number of grid points
itl	total number of global iterations
k	turbulent kinetic energy
K,L,M	pitot-probe calibration coefficients
L	plate length
p	pressure
P_x, P_z	axial and depthwise external-flow pressure gradients, respectively
R	residual
Re, Re_λ	Reynolds number $(= U_c L/\nu, U_c \lambda/\nu)$
t	time
U_c	carriage speed, uniform-stream velocity
U_{cl}	wake centerline velocity
U_{cp}, W_{cp}	wake centerplane axial and crossflow velocities, respectively
U_τ	wall-shear velocity $(= \sqrt{\tau_w/\rho})$
U,V,W	velocities in the (x,y,z) directions, respectively
$V_{T,B,P,S}$	probe-hole voltages
V	calibration-velocity vector
V	magnitude of calibration-velocity vector
V_{ib}, V_v	projection of V onto X-Y and Y-Z planes, respectively
w	velocity defect

w_0	centerline velocity defect
x, y, z	global Cartesian coordinates
x^+, y^+	dimensionless distances ($= U_{\tau x}/v$, etc.)
X, Y, Z	local Cartesian coordinates for pitot-probe measurements

Greek

α	angle between V_v and X-axis
$\alpha_b, \alpha_U, \alpha_v, \alpha_w, \alpha_\beta, \alpha_p$	under-relaxation factors
δ	boundary-layer thickness
δ^*	streamwise displacement thickness
ε	rate of turbulent energy dissipation
η	wave elevation
θ	streamwise momentum thickness
λ	wave length
ν	kinematic viscosity
ν_t	eddy viscosity
ξ, η, ζ	boundary-fitted coordinates
ρ	density
τ	Reynolds shear stress
τ_w	wall-shear stress
ϕ	angle between V and V_h

Superscripts

'	local values for pitot-probe measurements
e	edge value, edge of boundary layer and wake

I. INTRODUCTION

The present work stems from two previous studies concerning the effects of waves on the boundary layer of a surface-piercing body. Initially (Stern, 1986), the boundary-value problem was formulated and order-of-magnitude estimates were derived for the boundary-layer/free-surface juncture region which show that the flow is analogous to the flow in a streamwise corner in that a consistent formulation requires the solution of higher-order viscous-flow equations. Numerical results were presented for laminar and turbulent flow for the model problem of a combination Stokes-wave/flat-plate flow field utilizing first-order boundary-layer equations and both small-amplitude-wave and more approximate zero-gradient free-surface boundary conditions. Subsequently (Stern et al., 1989), results from a towing-tank experiment were presented utilizing a unique, simple foil-plate model geometry (figure 1) which simulates the Stokes-wave/flat-plate flow field. Mean-velocity profiles in the boundary-layer region and wave profiles on the plate were measured for three wave-steepness conditions. For medium and large steepness, the variations of the external-flow pressure gradients were shown to cause acceleration and deceleration phases of the streamwise velocity component and alternating direction of the crossflow, which result in large oscillations of the displacement thickness and wall-shear stress as compared to the zero-steepness condition. The measurements were compared and close agreement was demonstrated with the results from the turbulent-flow calculations with the zero-gradient approximation for the free-surface boundary conditions. Also, wave-induced separation is discussed which is present in the experiments and the laminar-flow calculations under certain conditions.

Herein, results are presented from extensions of both the previous experimental and theoretical work. In the former case, the measurement region is extended into the wake where both mean-velocity and wave-elevation measurements are made. In the latter case, a state-of-the-art viscous-flow method is brought to bear on the present problem, in which the Reynolds-averaged Navier-Stokes equations are solved for both the boundary-layer and wake regions. A review of the literature on the present topic was provided by Stern (1986). More recently, Toda et al. (1991) and Tahara et al. (1990) provide updated reviews of relevant experimental and computational work, respectively. It should be recognized that the present study as well as those just referenced are part of a large project concerning free-surface effects on ship boundary layers and wakes. In addition to the earlier mentioned precursory work, some other related studies under this project (i.e., Toda

et al., 1991; Tahara et al., 1990) will be referenced later with regard to further details concerning the experimental equipment and procedures and the computational method.

In the presentation of the results and the discussions to follow, a Cartesian coordinate system is adopted in which the x-, y-, and z-axes are in the direction of the uniform flow, port side of the plate, and depthwise, respectively. The origin is at the intersection of the waterplane and the leading edge of the plate. The mean-velocity components in the directions of the coordinate axes are denoted by (U,V,W) and the uniform stream (i.e., carriage velocity) by U_c . Unless otherwise indicated, all variables are nondimensionalized using the plate length L, carriage velocity U_c , and fluid density ρ .

An outline of this report is as follows. The experimental equipment and procedures are described in Chapter II. Next, in Chapter III, an overview is provided of the computational method and the computational grids and conditions are described. Then, in Chapter IV, the experimental and computational results are presented and discussed, including some additional computational results for both turbulent and laminar flow, which aid in explicating the characteristics of the near and intermediate wake, the periodic nature of the far wake, and wave-induced separation. Lastly, in Chapter V, some concluding remarks are made.

II. EXPERIMENTAL EQUIPMENT AND PROCEDURES

The experiments were performed in the Iowa Institute of Hydraulic Research (IIHR) towing tank (figure 2). The towing tank is 91.4 m long and 3 m wide and deep. It is equipped with one towing carriage and two instrumented trailers, north and south, either one of which can be attached to the towing carriage for performing experiments. The model, traverse, and instrumentation are mounted to the trailers which allows for easy access and optimum viewing. For the present study, the south trailer was used. The towing carriage is cable-driven by a 15 hp motor fitted with a tachometer-feedback (analog-feedback) speed regulator. The carriage can be driven at speeds up to 3 m/s with an accuracy of ± 10 mm/s. The carriage is operated from a control panel situated on the carriage.

A. Model Geometry

The experimental model is shown in figure 1. Stern et al. (1989) provide a detailed description of the design and construction of the model; however, some modifications were made to enable the wake measurements. In particular, the plate length was shortened to $L = 1.2$ m, the leading edge was rounded, the trailing edge was tapered, the sidewall endplates were extended into the wake region, and L-beams were mounted on both sides of the plate at the top and bottom for structural stiffness. The detailed plate geometry is shown in figure 3 [cf. figure 4 of Stern et al. (1989)]. The leading- and trailing-edge modifications were based on previous flat-plate wake wind-tunnel experiments (e.g., Pot, 1979; Andreopoulos, 1980; Ramaprian et al., 1982). In order to induce turbulent flow, a row of cylindrical studs of .8 mm height and 3.2 mm diameter were fitted with 9.5 mm spacing on the plate at $x = .05$. Also, as was the case with the previous plate, a 2 x 2 cm grid was painted on the nonmeasurement side of the plate to facilitate wave-profile measurements. Lastly, the entire model was refurbished prior to initiating the present program of experiments.

B. Instrumentation

The wave elevations were measured using a Shinozuka 15 cm AC servo-mechanism wave probe on loan from the Osaka University (figure 4). The probe was mounted to the trailer and towed with the foil-plate model. Figure 5 is a photograph of the automated traverse used to position the probe. The probe could be moved in three directions of a Cartesian coordinate system. The crossplane positioning (y - z planes) was driven by two stepper motors which were controlled by a microcomputer on the carriage. The axial (x -direction) positioning was achieved by manually moving the y - z traverse system along 1.5 m rails. For large distance axial positioning, the relative position of the traverse and foil-plate model were adjusted on the trailer.

A five-hole pitot probe (modified NPL type) also on loan from Osaka University was used to measure the direction and magnitude of the mean velocity in the flow field. The probe is shown in figure 6. The same automated traverse (figure 5) was used for positioning the probe as that described earlier with regard to the servo-mechanism wave probe. The center hole of the five-hole pitot probe was connected by vinyl tubing to a branch. Four pressure tubes were divided at the branch and connected to one side of four Validyne differential pressure transducers with $\pm .3$ psi diaphragms. The surrounding four

holes were connected to the other side of the transducers. All of the tubings between the sensor holes and the diaphragm were filled with water. A block diagram of this arrangement is shown in figure 7a.

For each experiment, the voltage output from the servo-mechanism wave probe or transducers was sampled, digitized, recorded, and analyzed along with the carriage speed by a microcomputer on the carriage. The carriage speed was monitored during each carriage run by a voltage display. The time history of the five-hole pitot probe output was monitored by a single-channel pen recorder for certain carriage runs to check the response time.

C. Calibration

The servo-mechanism wave probe was calibrated by adjusting its relative position with respect to the water surface using the automated traverse. This was done each day before and after the measurements were performed. Typical calibration results are shown in figure 10 of Toda et al. (1991), which demonstrate the good repeatability of the measurements and the stability of the probe.

The differential pressure transducers were calibrated using two water tanks. One was moved up and down by the automated traverse while the other was at a fixed elevation, i.e., the pressure was measured by water head. The calibration was usually carried out before and after the measurements at a particular station. Typical calibration results are shown in figure 11 of Toda et al. (1991), which demonstrate that the curves are linear and repeatable.

The five-hole pitot probe was calibrated in the IIHR 1.07 m octagonal, open-throat test section, closed-circuit wind tunnel using the calibration device shown in figure 8. The calibration was done at a wind speed of about 16.5 m/s. The data were analyzed using a method similar to Fujita (1979). The probe-based Cartesian coordinate system (X, Y, Z) and other basic quantities used for the data analysis are defined in figure 9. Referring to figure 9, the X -axis is in the direction $O-C$ and the Y - and Z -axes are in the $T-C-B$ and $P-C-S$ planes, respectively. The origin is at the center of curvature of the tip face. The probe holes are designated $C, T, B, P,$ and S and the corresponding sensed pressures are $H_C, H_T, H_B, H_P,$ and H_S , respectively. The calibration-velocity vector is V and its projections in the $X-Y$ and $Y-Z$ planes are V_h and V_v , respectively. The angle between V_v and the X -

axis is α , and the angle between V and V_v is ϕ . H_C etc. were measured as differential pressures relative to the ambient pressure. The probes were calibrated in the range $-25^\circ \leq \phi \leq 25^\circ$ and $-25^\circ \leq \alpha \leq 25^\circ$ with five-degree steps in ϕ and α . The following calibration coefficients were then calculated:

$$M(\phi, \alpha) = [H_C - (H_T + H_B + H_P + H_S)/4]/(V^2/2g) \quad (\text{II-1})$$

$$K(\phi, \alpha) = (H_T - H_B)/[H_C - (H_T + H_B + H_P + H_S)/4] \quad (\text{II-2})$$

$$L(\phi, \alpha) = (H_S - H_P)/[H_C - (H_T + H_B + H_P + H_S)/4] \quad (\text{II-3})$$

where g is the gravitational acceleration and $V^2 = V \cdot V$. The wind-tunnel speed V and ambient pressure and temperature were monitored using a total-head tube and thermometer, respectively. These coefficients are shown in figures 10a,b.

The procedure for evaluating the mean-velocity components (U,V,W) from the local probe measurements and the calibration coefficients, (II-1) through (II-3), is as follows. Designating the local measured values with a ', the following quantities are determined:

$$v_{T,B,P,S}' = c^2(H_C' - H_{T,B,P,S}') \quad (\text{II-4})$$

$$\begin{aligned} M' &= \frac{c^2}{4}(v_T + v_B + v_P + v_S) \\ &= \frac{c^2}{4}M'' \end{aligned} \quad (\text{II-5})$$

$$K' = (v_B - v_T)/M'' \quad (\text{II-6})$$

$$L' = (v_P - v_S)/M'' \quad (\text{II-7})$$

where c will be defined later and $v_{T,B,P,S}$ corresponds to the voltage outputs from the four transducers corrected to an equivalent channel 1 voltage based on the transducer calibration curves. ϕ and α are determined from K' and L' using the calibration coefficient shown in

figure 10a. These are then used to determine M from the calibration coefficient shown in figure 10b. As a result, the following are obtained:

$$V' = \sqrt{2gM'/M} = c\sqrt{gM'/2M} \quad (\text{II-8})$$

$$U = V'\cos\phi\cos\alpha \quad (\text{II-9})$$

$$V = V'\sin\phi \quad (\text{II-10})$$

$$W = V'\cos\phi\sin\alpha \quad (\text{II-11})$$

The constant c is proportional to the slope of the dynamic calibration curve shown in figure 10c, which was obtained from measurements in uniform flow over a range of carriage speeds. Figure 7b provides a block diagram of the overall data analysis procedure. A computer program was used for data analysis in which values at desired points are obtained by third-order spline interpolation.

D. Data-Acquisition System

The data-acquisition system was an IBM PC-XT compatible microcomputer on the carriage with an 8 channel data-acquisition board. An RS-232C communication port (the serial port) was used to transmit signals to the controllers of the stepper motors. The carriage speed or sensed pressures were converted to a voltage and then filtered by a low-pass filter (including a unit gain amplifier) and sampled through the A-D converter and averaged over the measurement period. A sampling frequency of 200 Hz was used.

E. Experimental Procedure

Two types of measurements were made: wave elevations and mean-velocity profiles. In both cases, a time interval of about 12 minutes between carriage runs was necessary in order for the fluid motion induced by the previous run to be sufficiently damped.

Three wave-steepness conditions were selected for the measurements: zero, medium, and large. In each case, the experiments were conducted at the same carriage velocity ($U_c = 1.37$ m/s) such that, for the latter two cases, the wave length λ is about 120

cm, i.e., $\lambda = L$. The plate was placed at the middle of the tank and positioned longitudinally such that the trailing edge coincided with the second wave crest. The measurement locations, plate positions, and foil submergence depths are shown in figure 3.

For the wave-elevation measurements, two measurements were made per carriage run. A delay time of 5 sec was used after the carriage attained a steady speed and before the first measurement was performed. Subsequently, data was taken for a 5 sec period and then the probe position was changed by the automated traverse. A second 5 sec measurement period was initiated after a 3.5 sec delay time. Measurements were made at up to 15 axial and three transverse stations.

For the mean-velocity profiles, two and one measurements were made per carriage run for the zero- and medium-steepness conditions and the large-steepness condition, respectively. In the former case, the procedure was similar to that for the wave-elevation measurements, except a 7 sec measurement period was used. In the latter case, a 20 sec measurement period was used since the velocities in the wake region were found to be somewhat unsteady. Measurements were made at up to 12 axial stations, four on the plate and eight in the wake, and three depths, with usually about twenty transverse data points.

For the zero-steepness condition, the mean-velocity profiles were found to be symmetric with respect to the wake centerplane, although the wake centerplane deviated somewhat from the geometric centerplane. This deviation was attributed to the roughness on the port side of the plate caused by the painted grid (see Section II.A). The location of the wake centerplane was determined and the symmetry with respect to it confirmed by performing measurements on both the starboard and port sides of the wake. For the medium- and large-steepness conditions, it was found that the deviation was larger and the profiles displayed some asymmetry. Therefore, measurements were also made on both sides of the wake, although, in these cases, those on the port side were more limited.

F. Experimental Uncertainty

For the local wave-elevation measurements, the accuracy is estimated to be within $\pm .5$ mm in wave elevation, whereas for the mean-velocity measurements, the accuracy is estimated to be within 2.5% for the magnitude and 1.5 degree for the direction.

III. COMPUTATIONAL METHOD

As discussed earlier, the flow field of the foil-plate geometry simulates the Stokes-wave/flat-plate flow field for which first-order boundary-layer calculations (Stern, 1986) and comparisons with the measurements for the boundary-layer region (Stern et al., 1989) were previously performed. Although the comparisons showed close agreement and various important features of the wave-induced effects were isolated and identified, certain issues were not fully addressed due to the limitations of the first-order boundary-layer equations, e.g., the resolution of the flow very near the free surface, including the role of the free-surface boundary conditions, and the nature of wave-induced separation. Therefore, it was decided, as already mentioned, to bring to bear a state-of-the-art viscous-flow method on the present problem, in which the Reynolds-averaged Navier-Stokes equations are solved for both the boundary-layer and wake regions. In Chapter IV, the capabilities of the computational method will be evaluated through comparisons of the turbulent-flow solutions with the measurements. Also, some of the issues raised by the comparisons (i.e., the characteristics of the near and intermediate wake) and other features of the flow (i.e., the periodic nature of the far wake and wave-induced separation) will be investigated through some additional computational results for both turbulent and laminar flow.

The present computational method is similar to that of a related study, i.e., Tahara et al. (1990) in which an interactive approach is set forth for calculating ship boundary layers and wakes for nonzero Froude number, although the present work was done independently. Thus, many of the details of the method are provided by Tahara et al. (1990) and its associated references. Herein, an overview is given with the emphasis on the specific differences required for the present calculations. Also, the computational grids and conditions are described.

A. Approach

In the interactive approach of Tahara et al. (1990), two of the leading inviscid- (Rosen, 1989) and large-domain viscous-flow (Patel et al., 1988) methods are modified and extended for interactive calculations, including, in the latter case, incorporation of first-order free-surface boundary conditions. The interaction procedures are based on previous work for zero Fr (Stern et al., 1988): the match boundary is at about 2δ , where δ is the boundary-layer thickness; and the interaction law is based on the concept of displacement

thickness δ^* . Herein, the inviscid flow is prescribed as a second-order Stokes wave and the viscous-inviscid interaction is assumed negligible. Both these approximations were shown by Stern et al. (1989) to be quite good. Thus, the following overview is primarily concerned with the viscous-flow method.

In the viscous-flow method, the Reynolds-averaged Navier-Stokes equations are written in the physical domain using Cartesian coordinates (x,y,z) . Note that Tahara et al. (1990) use cylindrical coordinates for their applications. Closure is attained through the use of the standard k - ϵ turbulence model without modifications for free-surface effects. For laminar-flow calculations, the equations reduce to the Navier-Stokes equations by simply deleting the Reynolds-stress terms and interpreting (U,V,W) and p as instantaneous values. The governing equations are transformed into nonorthogonal curvilinear coordinates (ξ,η,ζ) such that the computational domain forms a simple rectangular parallelepiped with equal grid spacing. The transformation is a partial one since it involves the coordinates only and not the velocity components (U,V,W) . The transformed equations are reduced to algebraic form through the use of the finite-analytic method. The velocity-pressure coupling is accomplished using a two-step iterative procedure involving the continuity equation based on the SIMPLER algorithm.

The solution domain is shown in figure 11. The initial conditions are specified from simple flat-plate solutions. A two-point wall-function approach is used near the plate surface and, for the present application, a wake-function approach (Choi and Chen, 1988) is used near the plate trailing edge. At large depth and on the wake centerplane, symmetry conditions are imposed. On the exit plane, axial diffusion is assumed negligible and a zero-gradient condition is used for the pressure. On the outer boundary, the edge conditions for (U,W,p) are prescribed according to a second-order Stokes wave [i.e., equations (3) through (11) of Stern et al. (1989)] and a zero-gradient condition is used for (k,ϵ) . In order to insure a smooth merging of the viscous and inviscid solutions a technique was implemented whereby the edge conditions alternated during the global iterations between a Dirichlet condition $(U,W,p) = (U_e, W_e, p_e)$ and a Neumann (zero-gradient) condition $\partial(U,W,p)/\partial y = 0$. Finally, on the free-surface, calculations were performed using both first-order free-surface boundary conditions [i.e., equations (18) through (20) of Tahara et al. (1990)] and more approximate zero-gradient conditions; however, only the latter results are presented herein. Calculations using the former conditions as well as higher-order and exact treatments of the free-surface boundary conditions are in progress, as will be discussed later, and will be reported in the future.

B. Computational Grids and Conditions

The computational grids were obtained using the technique of generating body-fitted coordinates through the solution of elliptic partial differential equations. Because of the simplicity of the present computational geometry (figure 11), it was possible to specify the transverse and longitudinal sections of the computational domain as surfaces of constant ξ and ζ , respectively and, moreover, the three-dimensional grid was obtained by simply "stacking" the two-dimensional grid for the longitudinal plane. Partial views of the grids used in the calculations are shown in figures 11a,b for turbulent and laminar flow, respectively, including both longitudinal planes and typical crossplanes. For turbulent flow, in order to enable a more complete evaluation of the computational method, the plate thickness and detailed trailing-edge shape were resolved by the grid, whereas for laminar flow these details were neglected.

For turbulent flow, the inlet, exit, maximum depth, and outer boundaries are located at $x = (.05, 6)$, $z = 1.13$, and $y = 1.26\delta$, respectively, where δ is obtained from simple flat-plate solutions for the boundary-layer and wake regions; the first grid point off the plate surface is located in the range $47 \leq y^+ \leq 73$ and $x^+ = 330$ near the trailing edge; 170 axial grid points were used, with 40 over the plate and 130 over the wake; 20 radial grid points were used; and 9 depthwise grid points were used. In summary, the total number of grid points i_{max} used for the turbulent-flow calculations was $170 \times 20 \times 9 = 30600$.

For laminar flow, the grid was similar, except the exit boundary was located at $x = 10$; an even grid distribution was used in the y direction with the first point in the range $.000524 \leq y \leq .002368$ and $x = .02$ near the trailing edge; 200 axial grid points were used, with 40 over the plate and 160 over the wake; and 19 radial grid points were used. In summary, i_{max} used for the laminar-flow calculations was $200 \times 19 \times 9 = 34200$.

For turbulent flow, the calculation conditions were specified in order to simulate those of the experiments, i.e., calculations were performed for $U_c = 1.37$ m/s and three values of wave steepness $Ak = (0, .11, .21)$. Based on the latter two values, the wave length λ is 1.19 and 1.15 m, respectively, according to equation (11) of Stern et al. (1989); however, here the linear-theory value is assumed, $\lambda = 1.2$ m. Thus, $Re_\lambda = 1.64 \times 10^6 (=$

$U_c \lambda / \nu$), assuming an average water temperature of 20 deg C. On the inlet plane, the average values for δ and the wall-shear velocity U_τ are .00139 and .0498, respectively.

For laminar flow, the calculation conditions were similar, except $Re_\lambda = 2 \times 10^4$. This value of Re was selected based on the previous laminar-flow calculations of Stern (1986). On the inlet plane, the average values for δ and U_τ are .00791 and .10246, respectively.

For zero steepness, the calculations were begun with a zero-pressure initial condition for the pressure field. For nonzero steepness, the complete zero steepness solution was used as an initial condition. The solutions were built up in stages starting with small Ak values and achieving partial convergence and then incrementally increasing Ak until reaching the desired value and final convergence. The values of the time α_t , velocity $\alpha_{u,v,w}$, pressure-correction α_p , and pressure α_p under-relaxation factors and total number of global iterations itl used in obtaining both the turbulent and laminar solutions are provided in Table 1. The calculations were performed on the Naval Research Laboratory CRAY XMP-24 supercomputer. The CPU time required for the calculations was about 60 minutes for 200 global iterations.

Extensive grid dependency and convergence checks were not carried out since these had been done previously both for the basic viscous-flow method (Patel et al., 1988) and for other applications. However, some calculations were performed using both coarser and finer grids. These converged, respectively, more rapidly and slower than the present solutions. Qualitatively the solutions were very similar to the present one, but with reduced and somewhat increased resolution, respectively. The convergence criterion was that the change in solution be less than about .05% for all variables. Usually the solutions were carried out at least 50 global iterations beyond meeting this criterion. Figures 12a,b provide the convergence history of the pressure for the zero-steepness condition for turbulent and laminar flow, respectively, and are typical of the results for all the variables. In figure 12, the abscissa is the global iteration number it and the ordinate is the residual $R(it)$, which is defined as follows:

$$R(it) = \frac{\sum_{i=1}^{imax} |p(it-1) - p(it)|}{\sum_{i=1}^{imax} |p(it)|} \quad (III-1)$$

IV. EXPERIMENTAL AND COMPUTATIONAL RESULTS

Next, the detailed experimental and computational results are presented and discussed to point out the most important features of the wave-induced effects. Wherever possible, comparisons are made between the experiments and calculations, i.e., in Sections IV.A and IV.B, respectively, experimental and computational wave elevations and velocity profiles are compared. In general, the experimental results are discussed first, followed by the computational results and comparisons. Lastly, in Section IV.C, some additional computational results are provided, which are helpful in further explicating the flow physics.

A. Wave Elevations

Previously (Stern et al., 1989), comparisons were made between the measured wave profiles on the plate and the theoretical second-order Stokes-wave values. Close agreement was shown, except near the leading and trailing edges. For $x < .25$, the measured wave elevation is larger than the theoretical one due to the leading-edge effects of the plate, whereas for $x > .75$, the measured wave elevation is smaller than the theoretical one due to the damping influence of the plate. Although some minor differences were evident due to the model modifications and refurbishing, the present wave-profile measurements were very similar and consistent with the previous ones and, therefore, are not presented. Note that the wave profiles on the plate shown in figure 3 are based on these measurements.

Of greater interest to the present study are wave elevations in the wake region, which, as described earlier, were measured using the servo-mechanism wave probe. Measurements were performed for the same conditions as those described subsequently for the detailed velocity profiles, i.e., zero, medium, and large steepness and at up to 15 axial stations and three transverse locations $y = .02, .05, \text{ and } .1$. The first transverse location is about halfway across the boundary layer, the second is near the boundary-layer edge, and the third is well outside the boundary layer. The results are shown in figure 13.

For zero steepness, the wave elevations are very small in comparison to the results for medium and large steepness and only roughly follow the expected trends with regard to the free-surface shape and locations of the wave crests and troughs. In contrast, the results for medium and large steepness closely follow expectation. Interestingly, in the wake

region ($1 \leq x \leq 2$), i.e., over the second wave length, the wave elevations are somewhat larger than over the first wave length, especially near the third wave crest. This point will be discussed further later. The transverse variations are quite small, which confirms that in the measurement region the waves are nearly two-dimensional. A trend seems discernible that in regions of decreasing wave elevation, the elevations are slightly larger near the plate and wake centerplane than at greater distances, whereas the reverse holds true for regions of increasing wave elevation.

Also shown for comparison are second-order Stokes-wave elevations. The Ak values correspond to those used in the computations. Fairly close agreement is observed. The differences displayed in the wave profiles on the plate discussed earlier are not evident for medium steepness, but appear to be for large steepness.

B. Velocity Profiles

The conditions for the velocity-profile measurements were the same as those used previously (Stern et al., 1989): for large steepness, $U_c = 1.37$ m/s and foil submergence $d/c = 1.12$; and for medium steepness, $U_c = 1.37$ m/s and $d/c = 1.39$. For both conditions, $\lambda = 120$ cm, such that $Re_\lambda = 1.64 \times 10^6$ ($= U_c \lambda / \nu$), assuming an average water temperature of 20 deg C. Note that the plate length $L = \lambda$. Referring to figure 3, measurements were made for three depths $z/\lambda = (.0416, .0833, .125)$ and up to 12 axial positions $x/\lambda = (.25, .5, .75, 1, 1.125, 1.25, 1.375, 1.5, 1.625, 1.75, 1.875, 2)$. $(x, z) = (0, 0)$ is at the intersection of the plate leading edge and the undisturbed water level. As was also the case previously, an additional set of measurements were made for conditions which simulate zero steepness, i.e., a flat free surface: $U_c = 1.37$ m/s and $d/c = 2.75$. Previously (Stern et al., 1989), it was shown that this condition (i.e., the foil deeply submerged) more closely simulates a flat free surface than the condition with the foil removed. For zero steepness, measurements were made for $z/\lambda = 0.833$. $x/\lambda = (.8333, 1.042)$ in addition to the earlier values, and on both the starboard and port sides of the plate. For medium and large steepness, most of the measurements are for the starboard side, with some limited data obtained for the port side in order to determine the location of the wake centerplane and document the extent of the asymmetry. The discussions are primarily concerned with the measurements on the starboard side; however, consideration is given to issues related to the wake asymmetry and port-side measurements.

In the following, first, some limited results are presented for the without-plate condition and discussed in conjunction with the wave elevations, edge velocities, and Stokes-wave values to reach conclusions concerning the characteristics of the foil-plate model-wave system. Then, the detailed results for zero steepness are discussed, followed by those for large and medium steepness. For each condition, results are shown for the edge velocity (U_e, W_e), wake centerplane axial U_{cp} and crossflow W_{cp} velocity distributions, streamwise U , transverse V , and crossflow W velocity profiles, streamwise displacement thickness δ^* , and other quantities of interest. The experimental edge values were determined by fitting least-square splines to the data. All integral parameters (δ^* , etc.) were determined by trapezoidal rule integration. The accuracy of the integration is not as good for the experimental profiles as it is for the calculated ones due to the smaller number of data points obtained for the former. In the figures, the experimental values are shown by symbols and the calculated values by solid or dashed curves. In the velocity-profile figures, the outermost point is at 1.2δ , where the velocity components have their edge values. This point was a boundary condition in the calculations, but, in general, not a measurement point.

In most cases, only results for the wake region ($1 \leq x \leq 2$) are presented; since, previously Stern et al. (1989) provided results and discussion for the boundary-layer region. The present measurements for the boundary-layer region were obtained primarily to confirm the model modifications and refurbishing (see Section II.A) and were found, in all cases, to be similar and consistent with the previous data.

1. Without Plate

Measurements were made with the plate removed in order to determine the wave-making characteristics of the submerged foil without the interference and wavemaking effects of the plate, especially since data of this type were not obtained previously by Stern et al. (1989). The results are shown in figures 14a,b for large and medium steepness, respectively, including, in both cases, the zero-steepness results for comparison.

The results are very consistent with those described earlier for the wave elevations, i.e.: the wave effects are minimal for zero steepness, whereas for large and medium steepness they are significant and the trends closely follow expectation; the wave-induced velocities are somewhat larger in the wake than in the boundary-layer region; and the results show close agreement with the Stokes-wave values, including the depthwise

variations. As mentioned earlier, edge velocities will be shown later for each of the wave-steepness conditions. Comparison of the without-plate and edge velocities indicates close agreement between the two, although there are some apparent differences. In particular, the plate has a damping influence such that the wave-induced effects are somewhat increased for the without-plate condition and the plate interference and wavemaking influence the flow field such that the data are not as smooth and the agreement with the Stokes-wave values is not quite as good for the with-plate condition. However, the differences are not significant and it is concluded that the theoretical Stokes- and physical foil-plate model wave systems are in close agreement.

2. Zero Steepness

The primary purpose of the zero-steepness measurements is to aid in ascertaining the wave-induced effects through comparisons later with the results for large and medium steepness. In addition, it is of interest to compare the present results with benchmark results from wind-tunnel experiments for flat-plate turbulent wakes (e.g., Pot, 1979; Andreopoulos, 1980; Ramaprian et al., 1982) in order to evaluate the differences due to the present non-ideal conditions, i.e., free-surface effects and relatively low Re . The discussions and comparisons to follow also serve the purpose of summarizing the major conclusions from these earlier studies, which is useful in putting the present work in perspective. First, consideration is given to some global properties of the wake and then the detailed results.

As described in Section II.A, a 2 x 2 cm grid was painted on the port side of the plate to facilitate wave-profile measurements. The original intention was to only perform detailed velocity-profile measurements on the starboard side of the wake; however, it was found that the wake centerplane did not coincide with the foil-plate model geometric centerplane, which, no doubt, is attributable to the roughness of the paint. Therefore, detailed measurements were made on both the port and starboard sides of the plate for zero steepness in order to document the extent of the asymmetry.

Figure 15 displays the location of the wake centerplane. This was determined by fitting a third-order spline to the U -velocity component and evaluating the location of the minimum value. The wake is seen to drift slightly to the port side, i.e., the painted-side of the plate. The magnitude of the maximum drift is about $y = .004$. Although both the direction and magnitude of the drift are similar to results for the asymmetric wake of

roughened flat plates (e.g., Andreopoulos, 1980; Ramaprian et al., 1981), as will be shown next, the effects on the velocity profiles when referenced to the wake centerplane are, in fact, insignificant.

Figure 16 shows the usual overall properties for describing the wake: the half-width b/θ , the centerline velocity defect $w_o = 1 - U_c$, and the shape parameter $H = \delta^*/\theta$, where θ is the streamwise-momentum thickness. Note that in figure 16 the abscissa is x/θ and referenced to the trailing edge. Values are shown for both the port and starboard sides of the wake. Two values of w_o are shown since x/θ is different for each side. Also shown for comparison are Pot's (1979) and Ramaprian et al.'s (1982) data. The port- and starboard-side results are seen to be nearly identical, which indicates that the asymmetry is not significant. Also, the trends for all three parameters closely follow both Pot's and Ramaprian et al.'s data, in this case, confirming the suitability of the foil-plate model geometry for wake measurements.

The half width and centerline velocity defect are plotted using similarity variables in figure 17, i.e., $(b/\theta)^2$ and $(U_c/w_o)^2$ vs. x/θ . According to the assumptions in the far wake of small velocity defect ($w = 1 - U \ll 1$) and similarity [$w/w_o = f(y/b)$], both these quantities should vary linearly with x/θ . The additional assumption of a constant eddy viscosity ν_t turbulence model enables the evaluation of the proportionality constants (e.g., Schlichting, 1968), i.e.

$$(b/\theta)^2 = 16 \ln 2 (\nu_t / U_c \theta) (x/\theta) \quad (IV-1)$$

$$(U_c/w_o)^2 = 4\pi (\nu_t / U_c \theta) (x/\theta) \quad (IV-2)$$

Equations (IV-1) and (IV-2) with the experimental value for $\nu_t / U_c \theta = .032$ (Ramaprian et al., 1982) and the data of Pot (1979) and Ramaprian et al. (1982) are also shown in figure 17. Ramaprian et al. (1982) used a similar presentation in conjunction with velocity profile plots using inner-variable coordinates to identify three regions of the wake: near, intermediate, and far. In the near-wake region ($1 \leq x/\theta \leq 25$), the flow is characterized by the development of an inner wake, whose properties are governed by the details of the near-wall layers of the upstream boundary layers. The growth and decay rates are considerably larger than the asymptotic values. In the immediate neighborhood of the trailing edge (about $200t$, where t is the trailing-edge thickness), the flow is influenced by the geometry and thickness of the trailing edge. In the intermediate-wake region ($25 \leq x/\theta$

≤ 350), the wake evolves as a free turbulent flow, with coherent structures associated both with the small-scale mixing of the upstream inner wake and large-scale structures of the outer boundary layers. The growth and decay rates are smaller than the asymptotic values. In the far-wake region ($x/\theta > 350$), the flow attains similarity and the asymptotic growth and decay rates are realized. Here again, the present data shows close agreement with both Pot (1979) and Ramaprian et al. (1982). It is apparent that most of the present data is in the intermediate-wake region.

Figure 18a shows the asymptotic velocity-defect profiles w/w_0 vs. y/b for the starboard side of the wake. Although not included on figure 18a, the present results are in close agreement with both asymptotic theory and Pot's data.

The detailed velocity profiles for the starboard side of the wake are shown in figure 19. Consistent with the global properties, the U-velocity component displays a rapid recovery in the near-wake region ($1 < x < 1.375$), followed by a more gradual approach to uniformity. The edge values display the growth rate as well as the presence of free-surface effects since the values deviate somewhat from $U = 1$. The V-velocity component shows significant trailing-edge effects for $x = 1$ and 1.042, i.e., very large values near the wake centerplane associated with the flow convergence towards the wake centerplane. Subsequently, the profiles diffuse and display a rapid recovery such that near the end of the measurement region the values are quite small and nearly constant across the wake. The W-velocity component, which, of course, is zero for truly two-dimensional flow, displays small nonzero values ($W/U_c < 2.5\%$). Here again, this is attributed to free-surface effects.

Next, the computational results are considered, including the comparisons with the data. As is the case with the experiments, benchmark computational studies have been performed for flat-plate turbulent (and laminar) wakes. In fact, in this case, the number of studies are far too numerous to attempt a review or summary here. However, a few studies are of particular relevance to the present work and will be discussed next prior to presenting the results. These references can be consulted for further references on this topic.

Patel and Scheuerer (1982) showed that the major characteristics of symmetric and asymmetric flat-plate turbulent wakes could be predicted by the boundary layer equations with the $k-\epsilon$ turbulence model with wall functions, except for the far wake where the asymptotic growth rates were underestimated. Subsequently, Patel and Chen (1987) reconsidered the symmetric case using the complete Reynolds-averaged Navier-Stokes

equations and k - ϵ turbulence model with the objective of including the viscous-inviscid interaction and determining the influence of the terms neglected in the boundary-layer equations. Also, two different treatments were considered for the near-wall region, i.e., a two-point wall-function approach and a two-layer model in which a simple eddy-viscosity distribution is used for the wall region. Relatively minor differences are seen as a result of the inclusion of the viscous-inviscid interaction and the complete equations; however, the two-layer model improves the resolution of the flow close to the plate and in the near wake. The level of underestimation of the asymptotic growth rates is the same as that shown by Patel and Scheuerer (1982). Lastly, with regard to previous computational studies, Choi and Chen (1988) showed that a wake-function approach leads to a similar improvement for the global properties of the near wake as was obtained by Patel and Chen (1987) through the use of their two-layer model.

As described in Section III.A, the present computational method is based on that of Patel et al. (1988), which is essentially the same method as used by Patel and Chen (1987) for their turbulent flat-plate wake study; therefore, the present results for zero steepness are very similar to their results using wall-functions, except for a few important modifications: the use of a small computational domain without accounting for the viscous-inviscid interaction; the inclusion of the detailed plate geometry, i.e., plate thickness and detailed trailing-edge shape; and the use of a wake-function approach. The purpose of the following discussion is to verify the present computational procedures through comparisons with the data and establish the differences due to the aforementioned modifications.

Referring to figure 16, in general, close agreement is displayed between the computations and the data for the overall wake properties. However, the half-width is slightly underpredicted in the near wake and overpredicted in the intermediate wake and the centerline velocity defect and shape parameter are somewhat underpredicted in both the near and intermediate wake. In the far wake, the half-width is underpredicted and the centerline velocity defect and shape parameter are slightly overpredicted.

In order to further display the differences between the calculations and the data, the wake centerline velocity $U_{c1} = 1 - w_0$ vs. x is shown in figure 20 (curve 4). Also shown for comparison are calculations without the wake-function approach and the detailed plate geometry (curve 1), with the detailed plate geometry and without the wake-function approach (curve 2) and vice versa (curve 3), and the two-layer results from Patel and Chen

(1987). Curve 1 is essentially the same as the wall-function result from Patel and Chen (1987). Curve 2 shows a slight improvement, but not nearly as much as that reported by Choi and Chen (1988). Next, curve 3 indicates that the inclusion of the detailed plate geometry leads to results nearly identical to those from the two-layer model. Lastly, the present results predict even lower values in the near wake and display the closest agreement with the data.

The asymptotic results shown in figures 17 and 18 clearly display the earlier mentioned deficiency of the k - ϵ turbulence model in the far wake. As expected, the present results are similar and consistent with those of Patel and Chen (1987). Note that the results in the near and intermediate wake show rather close agreement with the data.

Referring to figure 19, the detailed velocity profiles show good agreement with the data; however, there are some important differences. In general, the U -velocity component is overpredicted and recovers faster than the data. Some of the differences can be attributed to the differences in edge values, i.e., $U_e = 1$ in the calculations, whereas in the experiments due to free-surface effects U_e departed somewhat from this value. The V -velocity component shows the same tendency as the data, but the trailing-edge effects are confined to $x \leq 1.042$ subsequent to which V is nearly zero. The W -velocity component is, of course, zero in the calculations. Also shown in figure 19 is the turbulent kinetic energy, although it was not possible to obtain data for comparison.

It can be concluded that, for conditions that simulate zero steepness, the wake development shows the typical characteristics of a two-dimensional flat-plate turbulent wake; however, there are some differences, which are attributable to the effects of the free surface. The agreement between the calculations and the measurements is generally quite good.

3. Large Steepness

The large-steepness wave elevation is shown in figure 13 and was discussed earlier in Section IV.A. Note that Stern et al. (1989) provide photographs of the wave profile on the plate for the large-steepness condition, which highlight the leading-edge effects [Stern et al. (1989) figure 16] and wave-induced separation [Stern et al. (1989) figures 6 and 8a] present near the free surface for $.8 \leq x \leq 1$. In the following, here again, first some global

properties of the wake are discussed and then the detailed results. In the former case, the zero-steepness values are shown on the figures for comparison.

The location of the wake centerplane for large steepness is also shown in figure 15. The magnitude of the drift is considerably larger than for zero steepness. The drift increases for $1 \leq x \leq 1.6$ and then reduces towards the zero-steepness value at $x = 2$. The magnitude of these trends increases with decreasing depth, i.e., the largest drift is near the free surface, which indicates that the wave-induced effects exacerbate the wake asymmetry. As mentioned earlier, some limited data was obtained for the port side to determine the just discussed location of the wake centerplane and document the extent of the wake asymmetry. Consistent with the increased drift of the wake centerplane for large as compared to zero steepness, the wake asymmetry was found to be somewhat more pronounced, i.e., some differences were evident in the edge values and integral parameters, but, here again, these were not significant when referenced to the wake centerplane. Also, the trends and general conclusions with regard to the free-surface effects on the wake are identical; therefore, in the following, it is sufficient to only consider the results for the starboard side.

The measured edge-velocity distribution is shown in figure 21. The results for $0 \leq x \leq 1$ are similar and consistent with those of Stern et al. (1989), i.e., the measurements display the typical characteristics of a two-dimensional wave, although the second wave crest is somewhat smaller than the first due to the damping influence of the plate. The results for $1 \leq x \leq 2$ are similar to those on the plate; however, as noted earlier, quite apparent is the fact that the wave elevations in the wake are larger than those on the plate. This is especially true in the region near the third wave crest. The zero-steepness values are seen to be negligibly small in comparison to those for large steepness and only roughly follow the expected trends.

Also shown on figure 21 are the second-order Stokes-wave values for $Ak = .21$. This value of Ak was selected to give the best overall agreement between theory and experiment and is the same as that used previously by Stern et al. (1989) for this same condition. As discussed earlier (Section IV.B.1) the theoretical and experimental values are in close agreement. Lastly, with regard to figure 21, note that the axial P_x and depthwise P_z external-flow pressure gradients can be discerned from the edge velocities, which distinguish regions of adverse and favorable gradients [see Stern et al. (1989) equations (9) and (10) and figure 5], i.e.: P_x is favorable for $0 \leq x \leq .5$ and $1 \leq x \leq 1.5$ and adverse for

.5 $\leq x \leq 1$ and 1.5 $\leq x \leq 2$; and P_z is favorable for 0 $\leq x \leq .25$, .75 $\leq x \leq 1.25$, and 1.75 $\leq x \leq 2$ and adverse for .25 $\leq x \leq .75$ and 1.25 $\leq x \leq 1.75$.

Figure 22 displays the wake centerplane axial U_{cp} and crossflow W_{cp} velocity distributions. Initially, for 1 $\leq x \leq 1.125$, U_{cp} is smaller near the free surface than at the two larger depths and all three values are below that for zero steepness. Apparently the axial flow has not yet recovered from the effects of the upstream adverse P_x . Subsequently, for 1.25 $\leq x \leq 1.5$, the effects of the favorable P_x are clearly visible, i.e., U_{cp} increases towards the free surface with values considerably larger than those for zero steepness. Finally, for 1.5 $\leq x \leq 2$, the effects of the adverse P_x in this region are evident such that the trend reverses, i.e., the velocities near the free surface become smaller than at larger depths and for zero steepness; however, the variation is not nearly as large as that observed upstream in the region of acceleration and appears to diminish with increasing x . The trends for W_{cp} are seen to correlate with P_z and follow those for W_e , but, interestingly, with increased magnitude, i.e., W_{cp} overshoots W_e . Also, the downward velocities for 1 $\leq x \leq 1.5$ and $x = 2$ are significantly larger than the upward velocities for 1.625 $\leq x \leq 1.875$. Note the nonzero downward values for $x = 1.5$ and 2, which clearly indicate the magnitude of the overshoot. The zero-steepness values are negligibly small and appear to follow the trends of the zero-steepness W_e .

The trends of the calculated values of U_{cp} and W_{cp} closely follow those just described for the measurements; however, there are some quantitative differences. The calculated U_{cp} indicates slightly larger values than the measurements in the region of favorable P_x , whereas the calculated W_{cp} indicates smaller values than the measurements over the entire region of the measurements.

The streamwise displacement thickness δ^* is shown in figure 23. Here again, the results for 0 $\leq x \leq 1$ are similar and consistent with those of Stern et al. (1989), i.e., for 0 $\leq x \leq .5$, δ^* is smaller near the free surface than at larger depths, whereas for .5 $\leq x \leq 1$ the reverse holds true. Note that the present values at $x = 1$ are considerably larger than the previous ones due to the plate modifications for the wake measurements, i.e., the tapered trailing edge. Stern et al. (1989) explicated these trends as a direct result of the influences of the external-flow pressure gradients P_x and P_z . The trends in the wake are similar, but with some important differences. In the region of favorable P_x , the flow acceleration near the free surface is very large which results in a significant reduction in δ^* . For $z = .0416$, the reduction is the greatest and the value remains nearly constant throughout this region,

whereas, for $z = .0833$ and $.125$, the amount of reduction is not as large and is basically monotonic with the minimum value occurring at $x = 1.625$. In the region of adverse P_x , δ^* increases; however, in this case, the minimum value is still near the free surface, i.e., the increase due to the adverse P_x is insufficient to overcome the effects of the upstream favorable P_x and cause a reversal of trend, as occurs on the plate.

The trends of the calculated values of δ^* are quite similar to those just described for the measurements. In the plate region, this is true both qualitatively and quantitatively; however, in the wake region, quantitative differences are apparent. In particular, the calculated reduction in δ^* is greater than the measurements and has a wave-like appearance, which closely correlates with the influences of both P_x and P_z . Interestingly, here again, as δ^* increases, the values near the free surface still remain smaller than those at larger depth.

The global results display a remarkable aspect of the wave-induced effects on the wake, i.e., the flow appears to be considerably more responsive to the effects of the favorable as compared to the adverse external-flow pressure gradient. This and other aspects of the solution will be further discussed next with regard to the detailed results.

The velocity profiles for $1 \leq x \leq 2$ and all three depths are shown in figure 24. First, the results at the smallest depth $z = .0416$ (figure 24a) are considered. The U-velocity component at $x = 1$ is similar to that presented by Stern et al. (1989), but with larger effects of the flow deceleration for reasons noted earlier. Subsequently, for $x = 1.125, 1.25, 1.375,$ and 1.5 , the profiles clearly display the effects of the flow acceleration, i.e., the inner part of the profiles undergo a rapid recovery such that by $x = 1.5$ the profile is nearly flat. Finally, for $x = 1.625, 1.75, 1.875,$ and 2 , the profiles remain relatively flat as the flow decelerates and the wake width increases. As already pointed out, there is a small reduction in U_{cp} in this region such that δ^* increases. A comparison of the results just described with those for zero steepness (figure 19) dramatically underscores the profound wave-induced effects on the wake development.

The V-velocity component also displays quite different behavior than that described earlier for zero steepness. At $x = 1$, the profile indicates flow convergence towards the wake centerplane, but with only a hint of the trailing-edge effects near the wake centerplane, which are dominant at this location for zero steepness, and a rapid reduction at the wake edge to its edge value. Subsequently, for $x = 1.125$ and 1.25 , the profiles reduce

in magnitude and undergo diffusion such that their shape is arc like. Then, for $x = 1.375$, 1.5 , and 1.625 , the magnitude increases and the profiles become relatively flat in the outer part of the wake. Finally, for $x = 1.75$, 1.875 , and 2 , the profiles again reduce in magnitude, beginning with the inner part of the profile, such that at $x = 2$ the profiles are nearly flat and of very small magnitude, i.e., nearly zero.

The W -velocity component at $x = 1$ is nearly the same as that presented by Stern et al. (1989). Subsequently, for $x = 1.125$ and 1.25 , W undergoes a rapid acceleration, especially for the inner part of the profile, such that the earlier noted overshoot of W_{cp} is quite pronounced. Then, for $x = 1.375$, 1.5 , 1.625 , and 1.75 , W decelerates and changes sign, however, in this case, the profiles become and remain relatively flat, i.e., the inner part of the profile does not overshoot W_e . Finally, for $x = 1.875$ and 2 , W again undergoes acceleration, but with only a hint of an increased response for the inner part of the profile as compared to the profiles near the plate trailing edge.

The results at the greater depths $z = .0833$ (figure 24b) and $.125$ (figure 24c) show very similar trends to those just described, but with reduced amplitudes in their deviation from two-dimensional flow (i.e., the zero-slope condition) due to the decay of the external-flow pressure gradients.

As has been the case throughout, the trends for the calculations are quite similar to those just described for the measurements. First considering the results for $z = .0416$, initially, for $x = 1$, the calculated U -velocity component is in fairly close agreement with the data. Subsequently, for $x = 1.125$, 1.25 , 1.375 , and 1.5 , consistent with the earlier discussion of the overprediction of U_{cp} , the inner part of the calculated profiles display considerably larger velocities than the data. Also, the calculated profiles indicate an overshoot in the outer part of the profiles, which occurs for $x = 1.125$ at about $3/4\delta$ (where, in this case, δ is the wake thickness) and then for $x = 1.25$, 1.375 , and 1.5 at about $1/2\delta$. The experimental data only hint at this type of an overshoot. Finally, for $x = 1.625$, 1.75 , 1.875 , and 2 , the profiles are relatively flat and show good agreement with the data; however, they indicate an even faster recovery. Although the trends for the calculated V -velocity component are similar to the measurements, the magnitude is considerably less and many of the details are lacking. For $x = 1$, 1.125 , and 1.25 , the W -velocity component closely follows the data in the outer part of the wake, but, here again, consistent with the earlier discussion of the underprediction of W_{cp} , the inner part of the calculated profiles display smaller values than the measurements. For $x = 1.375$, 1.5 ,

1.625, and 1.75, the shape of the calculated profiles is nearly the same as the measurements, but there appears to be a phase shift, i.e., the calculated profiles respond sooner than the measurements to the changes in P_z . Also, the calculations show smaller magnitudes than the measurements. For $x = 1.875$ and 2, the calculated profiles display the effects of the favorable P_z , but, here again, underpredict the acceleration of the inner part of the profile. Also shown on figure 24a is the calculated turbulent kinetic energy. A comparison with the profiles shown in figure 19 for the zero-steepness condition indicates that, initially, for $x = 1$ and 1.042, the maximum value is reduced and occurs more towards the middle of the boundary layer due, no doubt, to the effects of the upstream adverse P_x . Subsequently, for $x = 1.25$ and 1.375, the centerline value shows a large increase such that, for $x = 1.5, 1.625, 1.75,$ and 1.875, the profiles are relatively flat with somewhat larger values in comparison to zero steepness. The results at the greater depths $z = .0833$ and $.125$, show the same tendencies as those described earlier for the measurements.

In summary, the large-steepness results clearly display very significant wave-induced effects on the characteristics of the flat-plate wake, i.e., the influences of the external-flow pressure gradients, P_x and P_z , completely alter the nature of the wake development for the large- as compared to the zero-steepness condition. As found previously for the boundary-layer region (Stern et al., 1989), the variations of P_x and P_z cause acceleration and deceleration phases of the streamwise velocity component and alternating direction of the crossflow, which results in large oscillations of the displacement thickness and, in this case, the wake centerplane velocities as compared to the zero-steepness condition. In fact, the trends are even more pronounced for the wake than for the boundary-layer region. Furthermore, remarkably, the wake is seen to have a greater response, i.e., a bias with regard to the favorable as compared to the adverse pressure gradients. This important finding will be discussed further later in Section IV.C.1 in conjunction with some additional turbulent-flow computational results. No doubt, the aforementioned increase in wave elevation over the second in comparison to the first wave length is attributable to this bias. In general, the computations display good agreement with the data, but there are some important differences, which will be elaborated upon later in Chapter V. Note that, as was the case with the previous turbulent-flow calculations for $Ak = .21$ (Stern et al., 1989), wave-induced separation is not predicted, although, as mentioned earlier, it was exhibited in the experiments near the free surface for $.8 \leq x \leq 1$ for this same condition. The subject of wave-induced separation will also be discussed further later in Section IV.C.2 with regard to some additional laminar-flow computational results.

4. Medium Steepness

The medium-steepness wave elevation is shown in figure 13 and was discussed earlier in Section IV.A. The location of the wake centerplane for medium steepness is also shown in figure 15. The trends are similar to those for large steepness, but with reduced magnitudes at all depths. Here again, only the results for the starboard side of the wake are considered, which are shown in figures 25 through 28 using the same format as that used previously for the large-steepness condition. The second-order Stokes-wave values shown on figure 25 and used in the calculations are for $A_k = .11$. Here again, this value of A_k was selected to give the best overall agreement between theory and experiment and is the same as that used previously by Stern et al. (1989) for this same condition.

In general, the medium-steepness experimental and theoretical trends are similar and consistent with those for the large-steepness condition, except with reduced deviations from the zero-steepness values due to the smaller A_k . Thus, the medium-steepness results support the earlier discussed conclusions concerning the wave-induced effects on the wake, including the influences of the external-flow pressure gradients and the remarkable fact that the wake has a bias with regard to the favorable as compared to the adverse pressure gradients. In fact, these trends appear to be more exaggerated for the medium- as compared to the large-steepness condition.

C. Some Additional Computational Results

In this section, some additional computational results are considered for both turbulent and laminar flow. Of particular interest is the aforementioned bias of the near and intermediate wake, the periodic nature of the far wake, and wave-induced separation. The analysis of the results is facilitated by color graphics through the use of PLOT3D; however, the cost of color reproduction precludes a complete presentation of the color figures, i.e., only selected figures have been provided in color and the remainder are in black and white. The complete set of color figures is available from IIHR upon request for the cost of reproduction. Recall that the computational grids and conditions for both the turbulent and laminar solutions were described in Section III.B.

1. Turbulent Flow

The entire extent of the turbulent-flow calculations (figure 11a) encompasses not only the plate and near- and intermediate-wake regions, which were discussed earlier with reference to the data and comparisons, but also the far-wake region, i.e., the exit boundary extends to $x = 6$ (5 plate lengths beyond the plate trailing edge). It should be mentioned that obtaining solutions with large exit boundaries proved to be fairly difficult, i.e., preliminary calculations with the exit boundary at $x = 4.5$ were found to be relatively easier to obtain convergence and, in fact, to be accurate from the viewpoint of the resolution of the plate and near- and intermediate-wake regions; however, they did not enable the evaluation of the far wake. Thus, although difficult to obtain, such solutions were deemed necessary.

First, we consider the large-steepness results, which are provided in figures 29 through 37. U_{cp} , W_{cp} , and δ^* are shown in figure 29, including, in this case, the far wake region ($2 \leq x \leq 6$). Recall that the earlier discussions were primarily concerned with the near- and intermediate-wake regions ($1 \leq x \leq 2$), with some limited reference to the boundary-layer region ($0 \leq x \leq 1$). The results in the near and intermediate wake clearly display the earlier discussed fact that the flow is considerably more responsive to the effects of the favorable as compared to the adverse external-flow pressure gradients, i.e., the magnitude of the overshoots in response to favorable P_x and P_z are considerably larger than those in response to adverse P_x and P_z . This bias is evident even into the far wake ($2 \leq x \leq 4$), i.e., the maximum amplitudes are larger than the minimum amplitudes; however, the differences decay such that ultimately the wake achieves a periodic state in which U_{cp} , W_{cp} , and δ^* all appear to oscillate with equal maximum and minimum amplitudes about the deep (i.e., two-dimensional) solution. These trends are evident at all depths, but with reduced amplitudes. The erroneous growth of δ^* near the exit boundary is due difficulties in accurately evaluating δ^* over such large areas. Also, the results, in general, showed some influence of the exit conditions over about the last half wave length.

Next, we consider the characteristics of the solutions through the use of the PLOT3D color graphics. Figures 30 and 31 provide U- and - W-velocity component crossplane contours for the boundary-layer and near- and intermediate-wake regions. Figures 32 and 33 are similar, but are for the mean free surface and include, in the latter case, the complete solution domain. The color coding for the contour levels are shown on the figures. Note that - W is shown to facilitate the use of PLOT3D, i.e., in this case,

negative values (blue colors) correspond to downward flow and positive values (red colors) to upward flow. Figures 34, 35, and 36 provide velocity vectors and streamlines for the plate and wake centerplane, crossplane, and mean free-surface flows, respectively. The streamlines were generated through the use of the particle-trace capability of PLOT3D. As will be apparent through the subsequent discussions, PLOT3D has proved to be an indispensable asset for the study of three-dimensional flows.

Figure 30 vividly displays the earlier summarized wave-induced effects on the boundary layer, which were described in detail by Stern et al. (1989). The U- and W-velocity contours clearly display their acceleration and deceleration phases, including the depthwise decay of the wave-induced effects. The nature of the W-velocity component is quite remarkable. Note the strong downward flow near $\lambda/4$, the indication of S-shaped profiles near $\lambda/2$, and the strong upward flow near $3\lambda/4$.

Figure 31 just as vividly displays the wave-induced effects on the near- and intermediate-wake described earlier with regard to the present data and comparisons with the calculations. Considering the U-velocity component contours first. The deep solution provides a reference for the characteristics of the recovery of the usual flat-plate wake, whereas near the free surface, the wave-induced effects are evident. Note the predominance of red and yellow indicating relatively high velocity and the associated bias of the U-velocity component with regard to the favorable P_x . The largest amplitudes (most intense colors) are near the free surface and wake centerplane. Next, we consider the W-velocity component contours. In this case, note the predominance of blue and green indicating downward flow and the associated bias of the W-velocity component with regard to the favorable P_z . Here again, the largest amplitudes are near the free surface and wake centerplane. A comparison of figures 30 and 31 clearly displays that the wave-induced effects are larger and propagate to greater depths for the wake in comparison to the boundary-layer region.

Figures 32 and 33 exhibit the previously described wake trends in extreme. The U-velocity component is mostly red, whereas the W-velocity shows more blue than red. The latter figure shows the complete solution domain and, thus, provides from the perspective of the mean free surface, a display of both the nature of the periodic far wake and the manner in which the periodic state is ultimately attained. In the near- and intermediate-wake regions, the areas of red are larger than those of yellow for the U-velocity component contours, whereas ultimately the two areas appear to be equal. Similarly, for the W-

velocity component the blue areas are larger than the yellow areas, whereas ultimately the two areas appear to be equal.

The plate and wake centerplane flow (figure 34) shows the streamline convergence and divergence associated with the acceleration and deceleration phases, respectively. The crossplane flow (figure 35) shows the upward and downward flow patterns for the crossflow. The mean free-surface flow (figure 36) is essentially straight with no discernible displacement effect. Finally, the plate surface-pressure (figure 37a) and wake centerplane-pressure (figure 37b) contours display the regions of favorable and adverse P_x and P_z and their depthwise decay for these regions.

Figures 38 through 46 are similar in presentation to those just discussed, but for the medium-steepness condition. The PLOT3D presentations clearly display all of the previous conclusions with regard to the medium- as compared to the large-steepness condition, i.e.: the trends are similar and consistent with those for large-steepness, except for reduced deviations from zero-steepness due to the smaller Ak ; and the bias of the near and intermediate wake with regard to favorable as opposed to adverse pressure gradients is more exaggerated such that, in this case, the periodic state is not quite achieved at the exit boundary.

In summary, the additional turbulent-flow computational results facilitated the further study of the characteristics of the wake. The near- and intermediate-wake regions display a bias with regard to the favorable as opposed to the adverse pressure gradients such that the overshoots in response to the favorable gradients are considerably larger than those in response to the adverse gradients. Subsequently, there is a transition region where the differences decay such that ultimately the far wake achieves a periodic state in which U_{cp} , W_{cp} , and δ^* all appear to oscillate with equal maximum and minimum amplitudes about the deep (i.e., two-dimensional) solution. These trends are evident at all depths but with reduced amplitudes. Although the magnitude of the wave-induced effects are smaller for medium as compared to large steepness, the aforementioned trends appear more exaggerated. Recall that the data confirm the computational trends for the extent for which it was possible to perform the experiments.

Thus far, we have retained the terminology "near-wake region," "intermediate-wake region," and "far-wake region," which usually refers to and is based on the two-dimensional definitions given earlier in Section IV.B.2; however, it appears that these

regions are not particularly relevant for conditions under which wave-induced effects are significant. For such conditions, more appropriately, we redefine the near wake as the region over the first wave length ($1 \leq x \leq 2$) in which the extreme acceleration occurs; the intermediate wake as the region over the next three to five wave lengths ($2 \leq x \leq 3-5$) in which the transition occurs; and the far wake as the region in which the flow ultimately attains a periodic state ($3-5 \leq x$). The smaller and larger limits, respectively, refer to the large- and medium-steepness conditions.

To the authors knowledge, this is the first time that the phenomenon of a bias for a wake with a spatially, oscillating pressure gradient has been identified. Although overshoots are not unusual, e.g., as documented previously for the boundary-layer region (Stern et al., 1989) and in other applications such as duct (e.g., White, 1974) and boundary-layer (e.g., Telionis, 1981) flows with unsteady, oscillating pressure gradients, a bias, as documented presently, appears to be quite unique and has not received particular attention in the literature. As an aid in understanding this phenomenon, some further analysis was done of Lighthill's (1954) approximate high-frequency laminar-flow solution for a flat-plate boundary layer with an unsteady, oscillating pressure gradient to include second-order terms, which shows that δ^* , in fact, displays a bias; although, in this case, it is with regard to the adverse pressure gradient. Numerical turbulent-flow solutions have shown a similar trend (e.g., Patel and Nash, 1971). Notwithstanding the differences between the two physical situations (i.e., unsteady vs. spatially oscillating pressure gradient and boundary layer vs. wake), this previous work supports the physical possibility of a bias such as the present one and suggests the conclusion that it is due to nonlinear effects.

2. Laminar Flow

The extent and conditions for the laminar-flow calculations (figure 11b) were similar to those for the turbulent-flow calculations, except for the increased exit boundary $x = 10$ and decreased $Re_\lambda = 2 \times 10^4$. The laminar-flow calculations are considered invaluable; since, they represent solutions to the exact governing equations, whereas the turbulent solutions are dependent on the choice of turbulence model. Another very significant contribution of the laminar-flow calculations is that they enable the prediction of wave-induced separation, including the flow pattern in the separation region. Although the previous laminar-flow calculations (Stern, 1986) were able to predict the wave-induced separation point, they could not be continued into the separation region due to the use and

limitations of the first-order boundary-layer equations. A detailed discussion of both the previous calculations and the experimental observations of wave-induced separation was provided by Stern et al. (1989).

First, we consider the large-steepness results, which are shown in figures 47 through 55. The format is the same as that used previously for turbulent flow. The trends for U_{cp} are similar to those for turbulent flow; however, the extent of the region of recovery for the deep solution and, consistently, the transition region are increased, which was the reason for increasing the exit boundary. The magnitude of the wave-induced effects is similar to that for turbulent flow. The depthwise variations are not as gradual as for turbulent flow, i.e., the largest variations are near the free surface and, subsequently, decay quite rapidly towards the deep solution. Interestingly, the solution just above the deep one shows a reverse trend. The situation is similar for W_{cp} and δ^* , but, in these cases, in addition, the amplitudes are significantly increased. Also, note the extremely large values of δ^* near $x = 1$, associated with the wave-induced separation in this region.

The crossplane and mean free-surface contours indicate that all of the earlier discussed trends are not only evident, but are clearly considerably magnified for laminar in comparison to turbulent flow, no doubt, due to the increased three-dimensionality and response to pressure gradients for the former condition. For the boundary-layer region, the contours near the trailing edge are altered dramatically due to the effects of wave-induced separation. Noteworthy are the large bulges in the U contours associated with the rapid thickening of the boundary layer in the vicinity of the separated-flow region, including islands of reverse flow, and the complex nature of the W contours, i.e., the downward flow near the plate and upward flow in the outer region. Recall that for the without-separation condition the flow in this region is upward both in the inner and outer regions (cf. figures 30 through 33). For the wake region, the contours are similar to those for turbulent flow, except for the aforementioned differences. Here again, the mean free-surface contours display the trends in extreme. The plate and wake centerplane, crossplane, and mean free-surface velocity vectors and streamlines strikingly display the profound effects of wave-induced separation. The plate surface-pressure and wake centerplane-pressure contours are also similar to those for turbulent flow; however, the pressure is reduced substantially in the separation region (cf. figure 37).

The study of three-dimensional separated flows is certainly one of the most difficult topics of fluid mechanics. Modern computational and experimental techniques will

hopefully ultimately enable a more complete understanding and provide a theory for the description of these complex flows; however, at present this is not the case as evidenced by the wide variety of language and interpretations given to the seemingly infinite variety of possible flow patterns. No attempt will be made here to review the vast literature on this topic, but rather deference will be made to recent review articles, i.e., Tobak and Peake (1982) and Perry and Chong (1987) and work under another IIHR project on this topic, e.g., Kim (1991). Herein, we shall simply attempt a description of the present wave-induced separation using the language and concepts of the former two references.

A saddle point is indicated on the plate at $(x,z) \approx (.791, .2361)$ and a focal point on the mean free surface at $(x,y) \approx (.705, .026)$, as displayed in figures 52 and 54, respectively. In consideration of the existence of attachment and separation lines at the leading and trailing edges, respectively, we see that the number of nodes minus the number of saddles equals two; however, we are uncertain as to a known topological rule for the present geometry, i.e., a three-dimensional body intersecting a free surface. The overall separation pattern is classified as a global flow separation. Consistent with the presence of a saddle-focus combination, the crossplane flow (figure 53) clearly exhibits the generation of a longitudinal vortex. As a further aid in understanding the nature of the separation pattern, figures 56a,b,c display, respectively, particle traces in the separation region, the limiting streamlines on the plate and mean free surface and vortex skeleton near the separation point, and location of the separation lines and vortex center. One of the separation lines originates upstream and at the mean free surface and disappears into the saddle point, whereas the other originates at the saddle point and disappears into the mean free surface and downstream. The portions of the separation lines above the saddle point constitute the downstream and upstream faces of the region of reverse flow, which is seen to be quite large. The angles between the separation lines are designated $(\alpha,\beta,\delta,\gamma)$ which have the values (121, 97, 59.5, 69) deg, respectively. On the mean free surface, the upstream face, which demarcates the separation region and upstream flow, makes an angle of about 12.5 deg with the plate, whereas downstream of the separation region the outer and separated flows merge smoothly. The location of the vortex center was estimated from the crossplane flow (figure 53). The vortical motion is counterclockwise with respect to the flow direction and towards the free surface and clockwise with respect to the flow direction and in the main stream direction above (i.e., in the reverse flow region) and below the saddle point, respectively. Note that the vortex motion below the saddle point diffuses rapidly due to the influences of viscosity and the adverse pressure gradient in this region. The nature of the vortical motion was further explored through particle traces some of

which are partially displayed in figure 56a. The trajectories correspond to the locations $(x,z) = (.8179, .1164)$ and $(.8487, .1164)$ and y values across the entire domain, although only a few of the trajectories are shown. The locations are labeled on figure 56c. At the former location, initially, for $.00212 \leq y \leq .0106$, the flow direction coincides with the limiting streamlines. Next, for $.01272 \leq y \leq .01696$, the flow changes direction and follows the main stream. Then, for $.01908 \leq y \leq .0233$, the vortical motion is displayed, which is upward towards the free surface and into the focus (white colored particle trajectories). Lastly, for $y \geq .02757$, the flow direction is the same as the main stream with the transition occurring at $y = .02545$. At the latter location, initially, for $.002154 \leq y \leq .008614$, the flow direction coincides with the limiting streamlines. Next, for $.01077 \leq y \leq .01938$, the vortical motion is displayed, which is downward and towards the trailing edge (yellow colored particle trajectories). Lastly, for $y \geq .02584$, the flow direction is the same as the main stream with the transition occurring in the region $.02154 \leq y \leq .02369$. Additionally, particle traces were made for $(x,z) = (.8179, .1969)$ and $(.8432, .1969)$, which, in both cases, showed that the flow directions close to the plate surface ($y \leq .006$) coincides with the limiting stream lines, whereas the flow directions away from the surface ($y \geq .019$ and $y \geq .017$, respectively) are the same as the main stream. Based on the particle traces, a vortex skeleton was constructed as shown in figure 56b and it was concluded that the saddle and focal points are separation and attachment points, respectively.

Figures 57 through 65 are for the medium-steepness condition and, here again, the format is similar in presentation to that used previously. As was the case for turbulent flow, the trends are similar and consistent with those for large steepness, except for reduced deviations from zero steepness due to the smaller A_k , and the bias of the near- and intermediate wake with regard to favorable pressure gradients is more exaggerated. In this case, the transition region extends beyond the exit boundary. Also, wave-induced separation occurs, but with reduced extent. The saddle point of separation and focal point of attachment are at $(x,z) = (.844, .044)$ and $(x,y) = (.805, .004)$, respectively. The location of the separation lines and vortex center for medium steepness are also shown on figure 56c.

In summary, the additional laminar-flow computational results also exhibit the earlier discussed trends with regard to the wave-induced effects on the wake, which are, in fact, magnified for laminar as compared to turbulent flow. Furthermore, the laminar-flow calculations enabled the study of wave-induced separation, including the flow pattern in the

separation region. A saddle point of separation and a focal point of attachment are indicated on the plate and mean free surface, respectively. As the wave steepness increases, the saddle point moves downwards and towards the trailing edge, whereas the focal point moves downstream and away from the plate surface. The U- and W-velocity components display, respectively, flow reversal and S-shaped profiles. A longitudinal vortex is generated in which the vortical motion is counterclockwise with respect to the flow direction and towards the free surface and clockwise with respect to the flow direction and in the main stream direction above (i.e., in the reverse flow region) and below the saddle point, respectively. The identification of these features of wave-induced separation are considered very significant and invaluable, but must be considered with some caution and to some extent preliminary due to the approximate nature of the present free-surface boundary conditions. This point will be discussed further next in Chapter V. However, some partial validity is provided by the similarity of the present results for wave-induced separation and the previous calculations and experimental observations of Stern et al. (1989). In particular, the previously predicted separation starting points are similar to those indicated presently [cf. figure 10 of Stern et al. (1989)] and the shape of the separation region on the mean free surface is similar to that observed experimentally [cf. figure 9 of Stern et al. (1989)].

V. CONCLUDING REMARKS

Detailed experimental information has been presented which documents the effects of waves on the wake of a surface-piercing body. The effects are shown to be significant. In particular, the variations of the external-flow pressure gradients cause acceleration and deceleration phases of the streamwise velocity component and alternating direction of the crossflow, which results in large oscillations of the displacement thickness and wake centerplane velocities as compared to the zero-steepness condition. In fact, the trends are even more pronounced for the wake than found previously for the boundary-layer region (Stern et al., 1989). Furthermore, remarkably, the wake displays a greater response, i.e., a bias with regard to the favorable as compared to the adverse pressure gradients.

The measurements have been compared with solutions of the Reynolds-averaged Navier-Stokes equations and close agreement demonstrated, i.e., all of the experimentally observed trends are predicted; however, there are, in fact, some quantitative differences. In particular, the calculations have a tendency of overpredicting the wave-induced effects for the axial velocity and underpredicting those for the crossflow. Consistent with the latter,

the crossflow decay rate is also overpredicted. Although some of the differences can be attributed to the differences in the prescribed and experimental edge conditions, most of the differences are considered attributable and indicative of the present numerical procedures. In particular, the approximations embodied in the free-surface boundary conditions and turbulence model and numerical diffusion. Further work is required in all these areas to make a significant improvement in the computational method. With regard to the former, laminar-flow calculations are in progress using first-, higher-order, and exact treatments of the free-surface boundary conditions, including investigations of free-surface conforming grids, which are expected to be very helpful in this regard.

Some additional computational results have been presented for both turbulent and laminar flow, which aid in explicating the characteristics of the near and intermediate wake, the periodic nature of the far wake, and wave-induced separation. The near- and intermediate-wake regions clearly display a bias such that the overshoots in response to the favorable pressure gradients are considerable larger than those in response to the adverse pressure gradients. Subsequently, there is a transition region where the differences decay such that ultimately the far wake achieves a periodic state in which U_{cp} , W_{cp} , and δ^* all appear to oscillate with equal maximum and minimum amplitudes about the deep (i.e., two-dimensional) solution. These trends are evident at all depths but with reduced amplitudes. Although the magnitude of the wave-induced effects are smaller for medium as compared to large steepness, the aforementioned trends appear more exaggerated. Based on these trends, the usual definitions for the near, intermediate, and far wake were redefined for conditions under which wave-induced effects are significant.

To the authors knowledge, this is the first time that the phenomenon of a bias for a wake with a spatially, oscillating pressure gradient has been identified. Although overshoots are not unusual, e.g., as documented previously for the boundary-layer region (Stern et al., 1989) and in other applications such as duct and boundary-layer flows with unsteady, oscillating pressure gradients, a bias, as documented presently, appears to be quite unique. Some further analysis of work done on the latter application supports the physical possibility of such a bias and suggests the conclusion that it is due to nonlinear effects.

The additional laminar-flow computational results enabled the study of wave-induced separation, including the flow pattern in the separation region, which was shown to be very complex and significantly different than that in this region for the without-

separation condition. A saddle point of separation and a focal point of attachment are indicated on the plate and mean free surface, respectively. As the wave steepness increases the saddle point moves downwards and towards the trailing edge, whereas the focal point moves downstream and away from the plate surface. The U- and W-velocity components display, respectively, flow reversal and S-shaped profiles. A longitudinal vortex is generated in which the vortical motion is counter clockwise with respect to the flow direction and towards the free surface and clockwise with respect to the flow direction and in the main stream direction above (i.e., in the reverse flow region) and below the saddle point, respectively. The identification of these features of wave-induced separation are considered very significant and invaluable, but must be considered with some caution and to some extent preliminary due to the approximate nature of the present free-surface boundary conditions.

As was the case previously for the boundary-layer region (Stern et al., 1989), we have been able to explain most of the experimental and theoretical results solely with reference to the external-flow pressure gradients and without fully taking into account the free-surface boundary conditions. Stern et al. (1989) conjecture that the effects of the former may be predominant, except for detailed structures close to the free surface such as wave-induced separation, which were felt to depend very much on the free-surface boundary conditions as well. The present study supports this point of view and, furthermore, suggests that pressure-gradient effects may also predominate many aspects of wave-induced separation. However, more detailed experiments and calculations with more exact free-surface boundary conditions and appropriate turbulence models are required to confirm this.

With regard to the direction of future work, turbulence measurements both for the boundary-layer and wake regions would be very valuable as would detailed measurements very close to the free surface and measurements of the wave-induced separation flow pattern and of the far wake. Experiments using the present foil-plate model geometry and a laser-velocimetry system are being planned to obtain this type of information, however, it should be recognized that performing measurements such as these are, in fact, quite difficult in a towing-tank environment. As already pointed out, further calculations, including more exact treatment of the free-surface boundary conditions are essential, and in progress. Lastly, analytical and numerical studies for two-dimensional boundary layers and wakes with spatially, oscillating pressure gradients may be helpful in the further understanding of the bias phenomenon identified herein.

REFERENCES

- Andreopoulos, J., (1980), "Symmetric and Asymmetric Near Wake of a Flat Plate," J. Fluid Mechanics, Vol. 100, pp. 639-668.
- Choi, S.K. and Chen, C.J., (1988), "Calculation of Turbulent Wake Past a Flat Plate by Wake Function Method," Numerical Heat Transfer, Vol. 14, pp. 393-413.
- Fujita, T., (1979), "On the Flow Measurement in High Wake Region at the Propeller Plane," J. Soc. Naval Arch. Japan, Vol. 145, pp. 1-7.
- Kim, S., (1991), "Numerical Studies of Three-Dimensional Flow Separation," Ph.D. Thesis, The University of Iowa, Iowa City, IA.
- Lighthill, M.J., (1954), "The Response of Laminar Skin Friction and Heat Transfer to Fluctuations in the Stream Velocity," Proc. Royal Soc., Vol. 224, Series A. pp. 1-23.
- Patel, V.C. and Nash, J.F., (1972) "Some Solutions of the Unsteady Turbulent Boundary-Layer Equations," Proc. IUTAM Sym. on Recent Research on Unsteady Boundary Layers, Quebec, pp. 1106-1164.
- Patel, V.C. and Scheuerer, G., (1982), "Calculation of Two-Dimensional Near and Far Wakes," AIAA Journal, Vol. 20, No. 7, pp. 900-907.
- Patel, V.C. and Chen, H.C., (1987), "Turbulent Wake of a Flat Plate," AIAA Journal, Vol. 25, No. 8, pp. 1078-1085.
- Patel, V.C., Chen, H.C. and Ju, S., (1988), "Ship Stern and Wake Flows: Solutions of the Fully-Elliptic Reynolds-Averaged Navier-Stokes Equations and Comparisons with Experiments," Iowa Institute of Hydraulic Research, The University of Iowa, IIHR Report No. 323; also J. Computational Physics, Vol. 88, No. 2, June 1990, pp. 305-336.
- Perry, A.E. and Chong, M.S., (1987), "A description of Eddying Motions and Flow Patterns Using Critical-Point Concepts," Ann. Rev. Fluid Mechanics, Vol. 19, pp. 125-155.

Pot, P.J., (1979), "Measurement in a 2D Wake Merging into a Boundary Layer," NLR, The Netherlands, Rept. TR 19063 U.

Ramaprian, B.R., Patel, V.C., and Sastry, M.S., (1981), "Turbulent Wake Development Behind Streamlined Bodies," Iowa Institute of Hydraulic Research, The University of Iowa, IIHR Report No. 231.

Ramaprian, B.R., Patel, V.C., and Sastry, M.S., (1982), "The Symmetric Turbulent Wake of a Flat Plate," AIAA Journal, Vol. 20, No. 9, pp. 1228-1235.

Rosen, B., (1989), "SPLASH Free-Surface Code: Theoretical/Numerical Formulation," South Bay Simulations Inc., Babylon, NY (proprietary report).

Schlichting, H., (1968), Boundary Layer Theory, 6th ed., McGraw-Hill, New York.

Stern, F., (1986), "Effects of Waves on the Boundary Layer of a Surface-Piercing Body," J. Ship Research, Vol. 30, No. 4, pp. 256-274.

Stern, F., Yoo, S.Y. and Patel, V.C., (1988), "Interactive and Large-Domain Solutions of Higher-Order Viscous-Flow Equations," AIAA Journal, Vol. 26, No. 9, pp. 1052-1060.

Stern, F., Hwang, W.S., and Jaw, S.Y., (1989), "Effects of Waves on the Boundary Layer of a Surface-Piercing Flat Plate: Experiment and Theory," J. Ship Research, Vol. 33, No. 1, pp. 63-80.

Tahara, Y., Stern, F. and Rosen, B., (1990), "An Interactive Approach for Calculating Ship Boundary Layers and Wakes for Nonzero Froude Number," Proc. 18th ONR Sym. on Naval Hydro., Ann Arbor, Michigan; also to appear J. Computational Physics.

Telionis, D. P., (1981), Unsteady Viscous Flows, Springer-Verlag, New York.

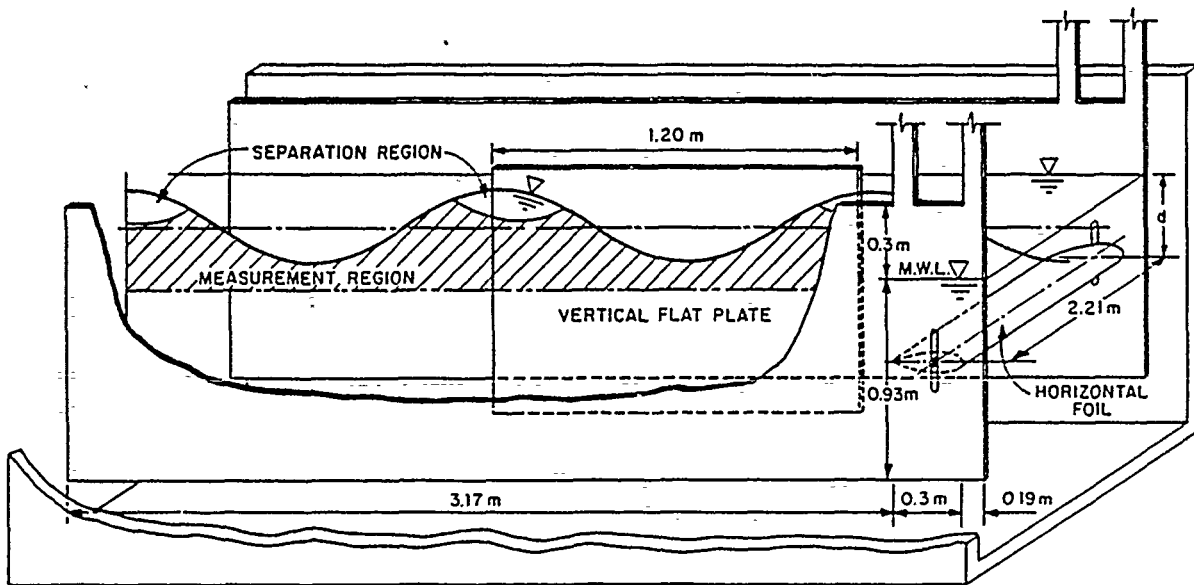
Tobak, M. and Peake, D.J., (1982), "Topology of Three-Dimensional Separated Flows," Ann. Rev. Fluid Mech., Vol. 14, pp. 61-85.

Toda, Y., Stern, F., and Longo, J., (1991), "Mean-Flow Measurements in the Boundary Layer and Wake and Wave Field of a Series 60 $C_B = .6$ Ship Model for Froude Numbers .16 and .316," Iowa Institute of Hydraulic Research, The University of Iowa, IIHR Report 352.

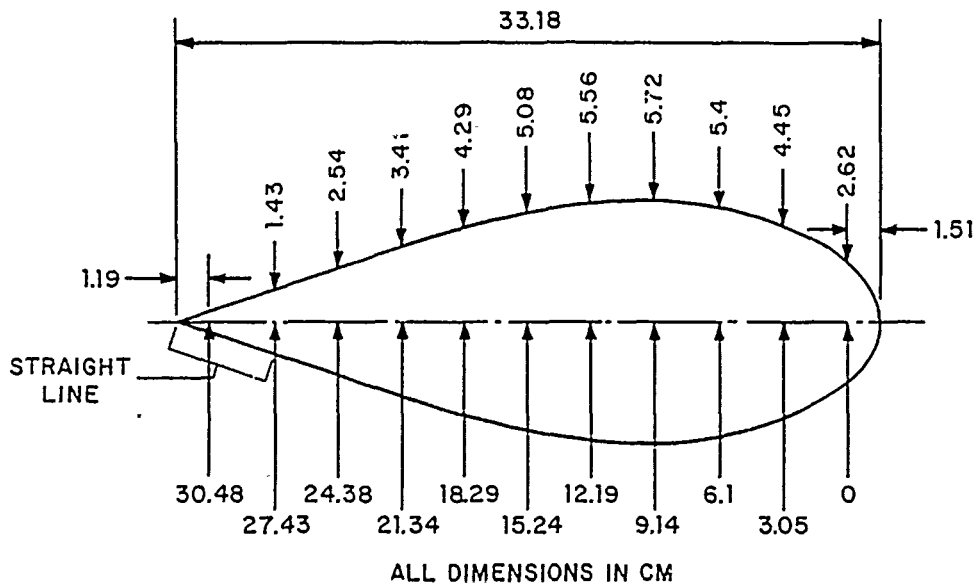
White, F. M., (1974), Viscous Fluid Flow, McGraw-Hill, New York.

Table 1. Under-relaxation factors and total number of global iterations

Parameter	Turbulent			Laminar		
Ak	0	.11	.21	0	.11	.21
α_t (plate)	.1	.01-.1	.01	.2	.001-.2	.0001-.01
α_t (wake)	.05	.002-.05	.005	.15	.001-.15	.01-.05
$\alpha_{u,v,w}$	1	.1-1	.25-.1	.1	.1-.25	.05-.5
$\hat{\alpha}_p$	1	.01-1	.01-1	.1	.1-1	.01-.1
α_p	.5	.0001-.5	.001-.01	.025	.0001-.25	.0005-.05
itl	200	1200	800	150	900	1200



(a) perspective view



(b) foil geometry

Figure 1. Foil-plate model geometry.

- | | | |
|-----------------|---------------------------|--------------------------|
| ① NORTH TRAILER | ④ SOUTH TRAILER | ⑦ STORAGE AREA |
| ② CARRIAGE | ⑤ BEACH | ⑧ SUB BASEMENT |
| ③ COMPUTER | ⑥ DRIVE AND SPEED CONTROL | ⑨ PLUNGER-TYPE WAVEMAKER |

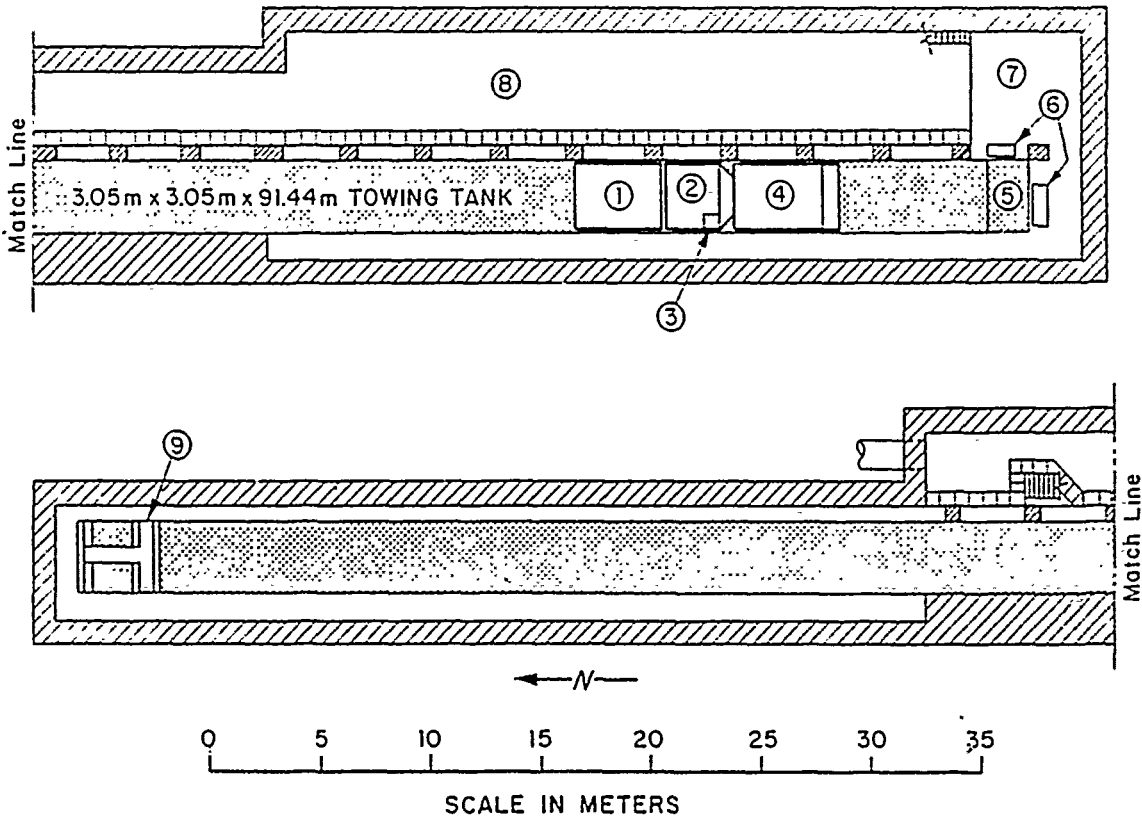
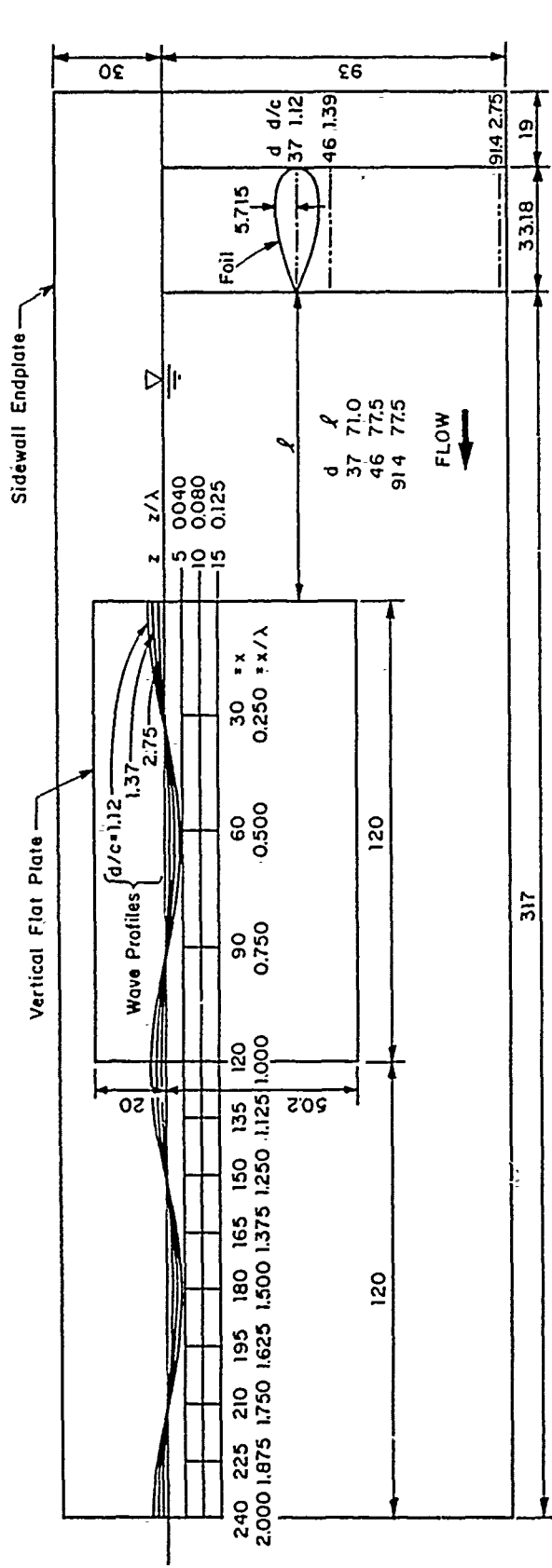
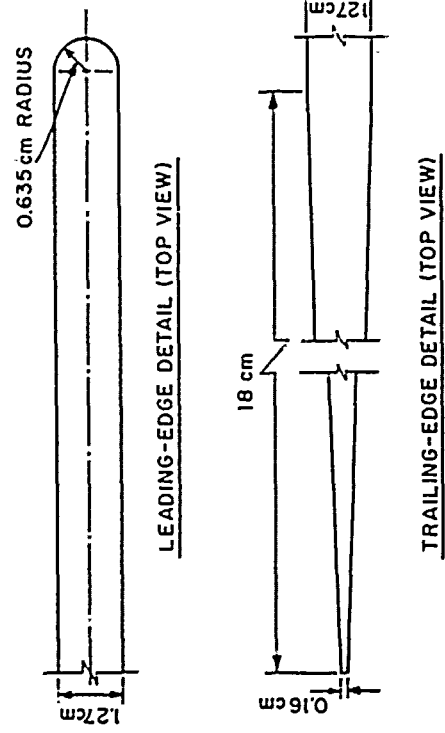


Figure 2. IIHR towing tank.



SIDE VIEW

All dimensions in cm.



OVERHEAD VIEW

Figure 3. Plate geometry and positions, measurement locations, and foil submergence depths.

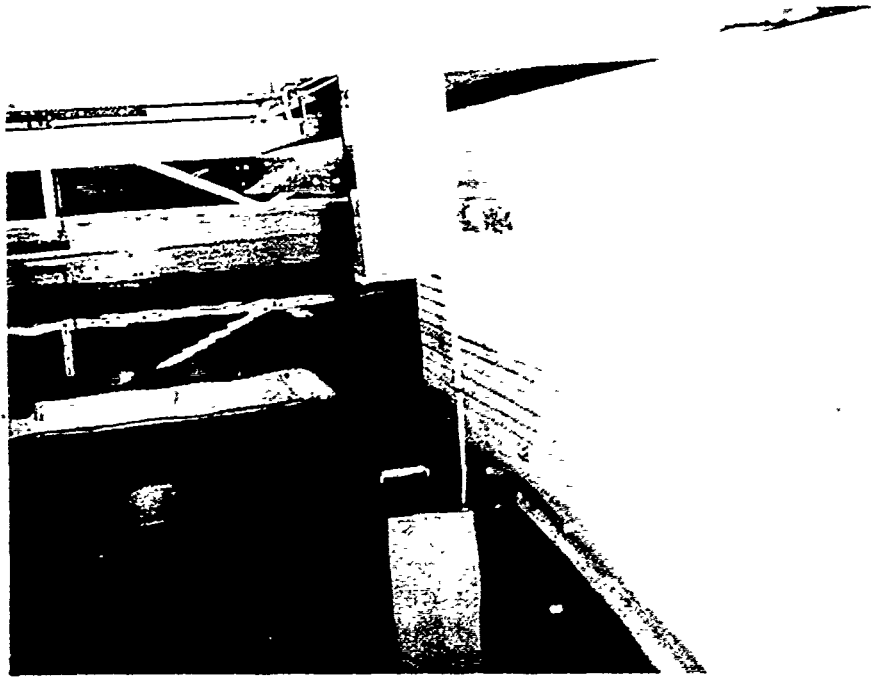


Figure 4. Servo-mechanism wave probe.

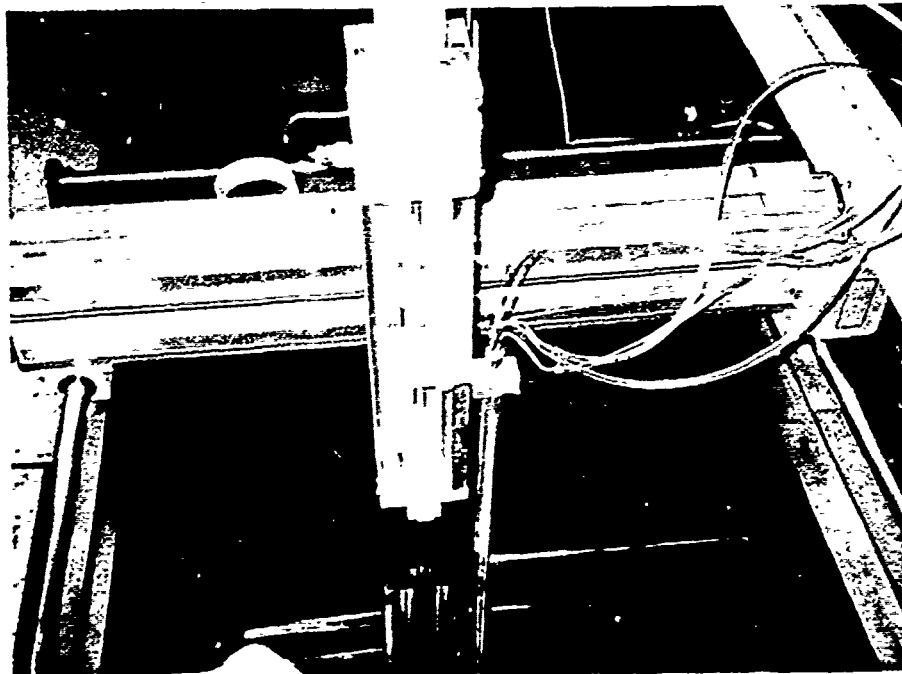


Figure 5. Automated traverse.

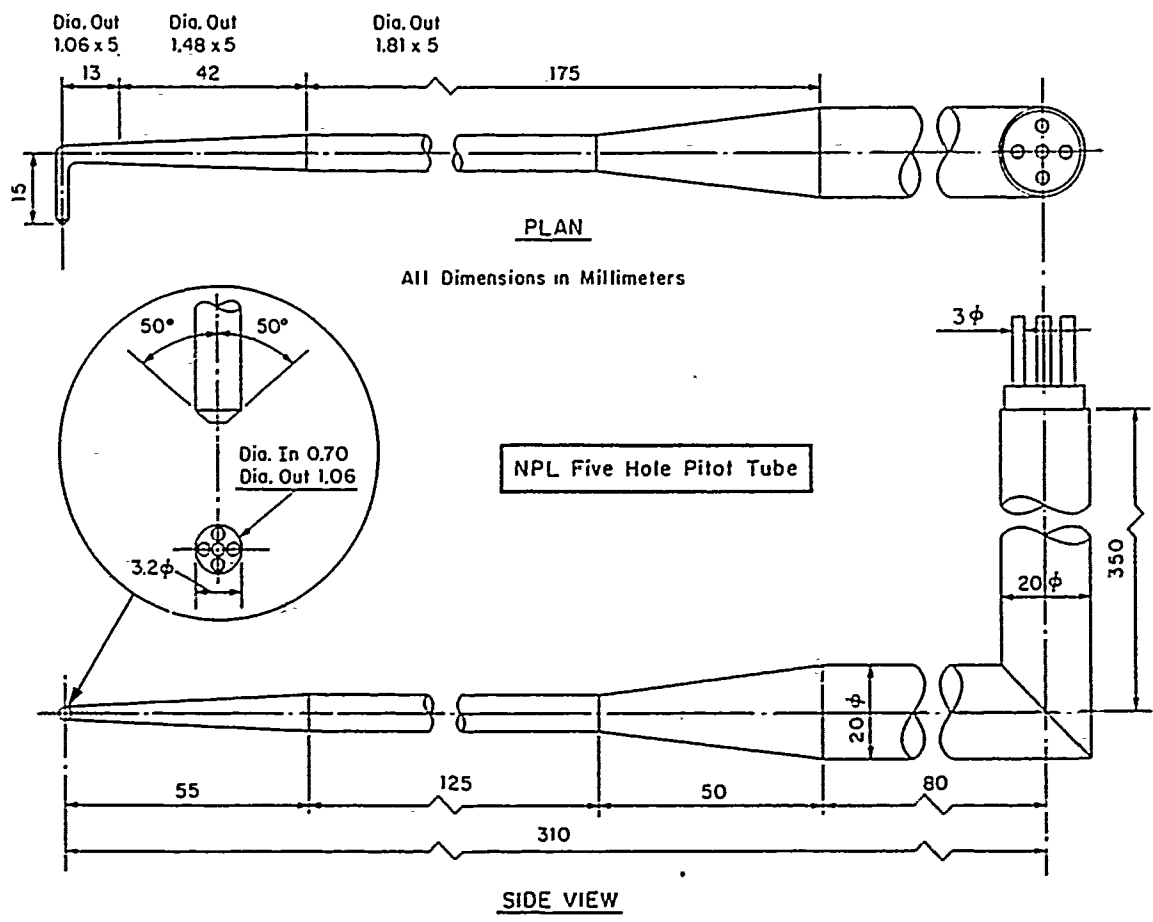
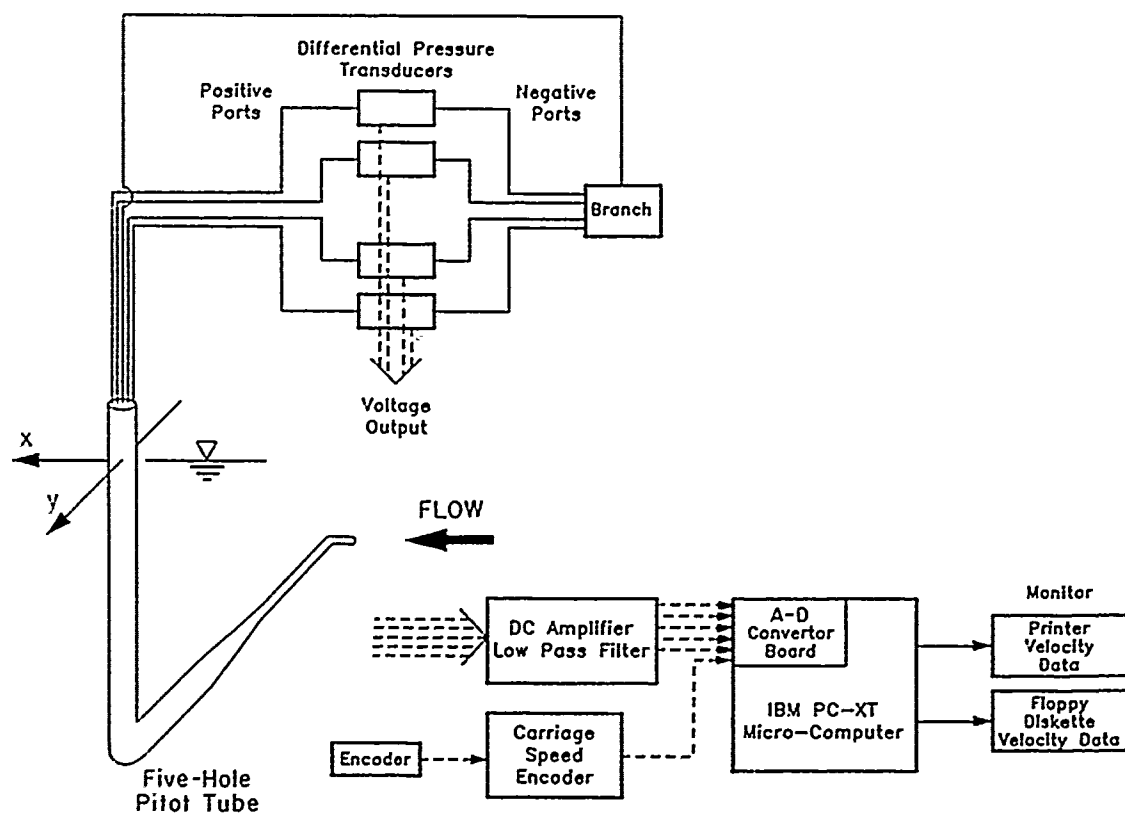
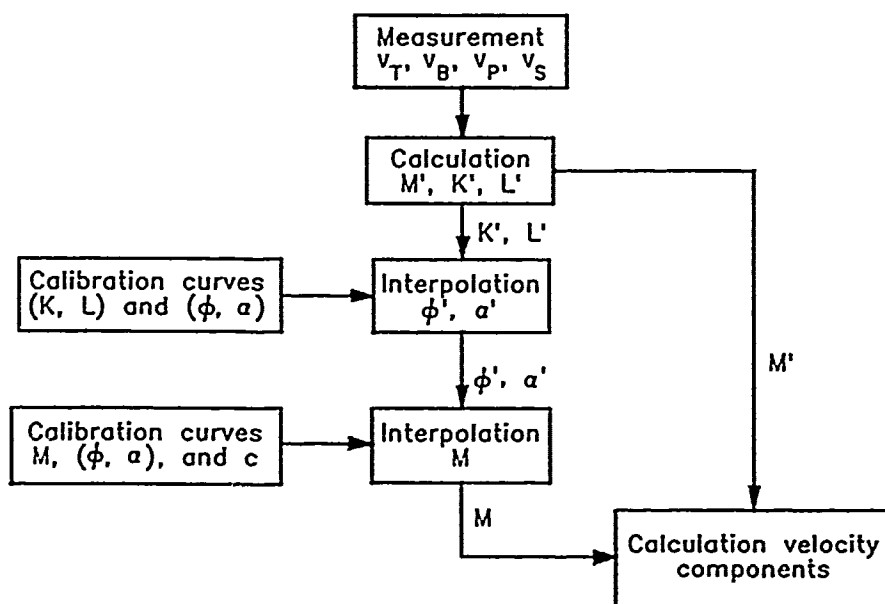


Figure 6. Five-hole pitot probe.



(a) data acquisition



(b) probe calibration

Figure 7. Block diagram for mean-velocity measurements.

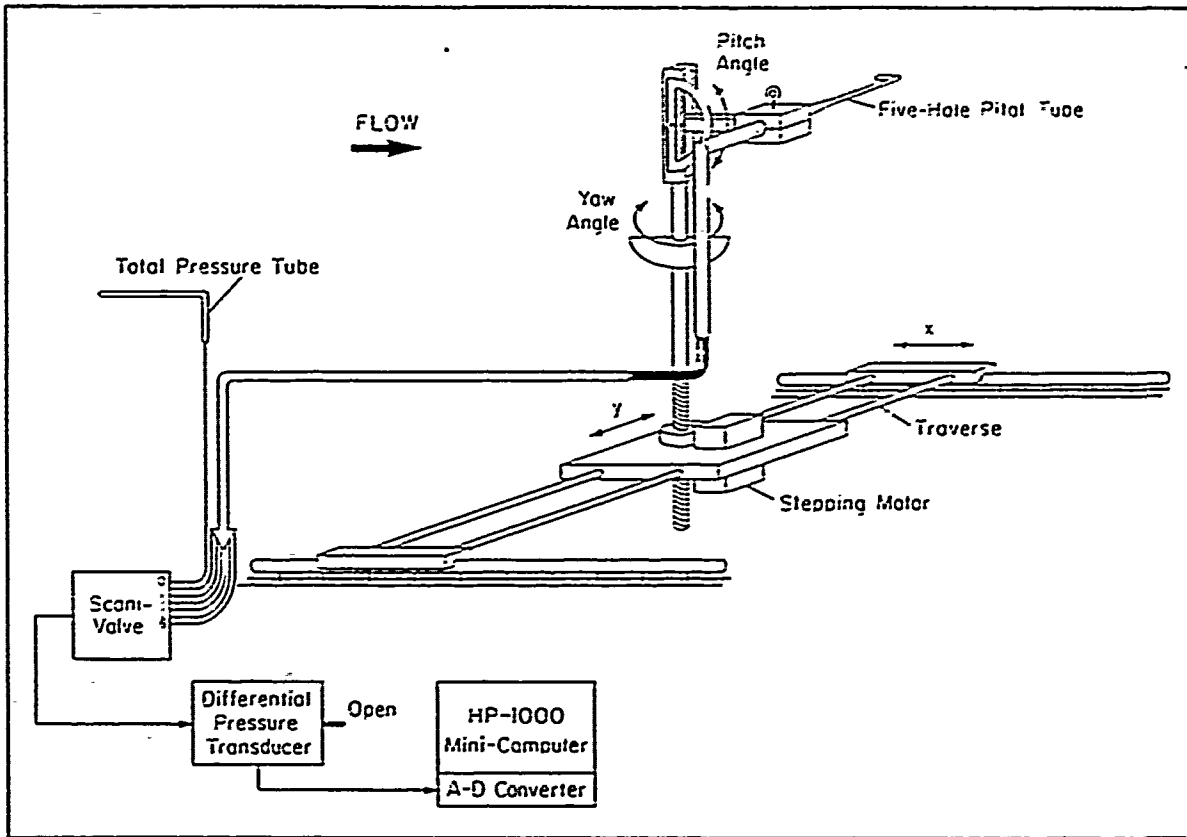


Figure 8. Calibration device.

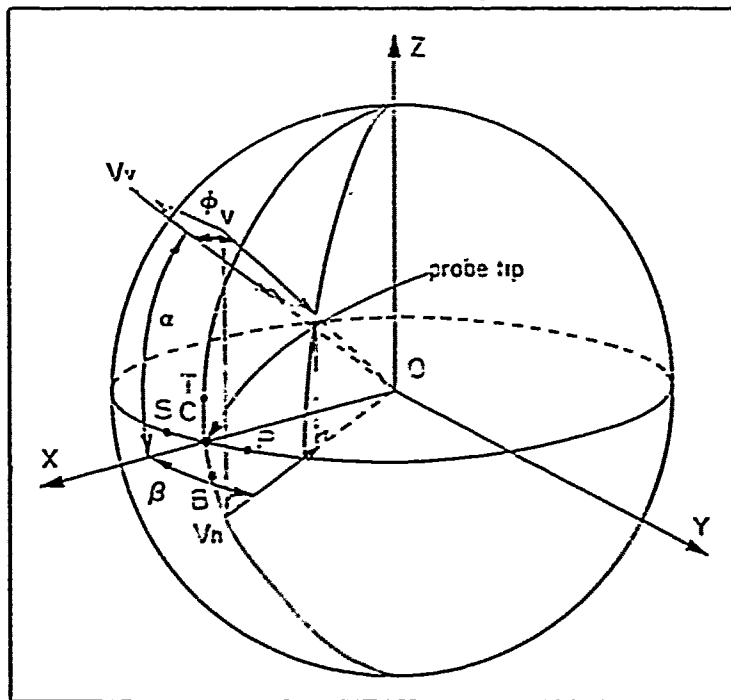
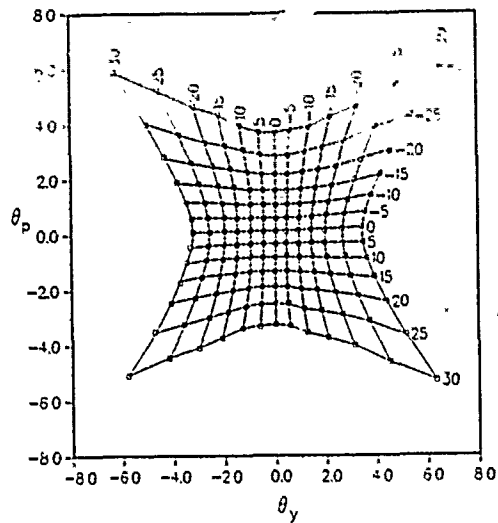
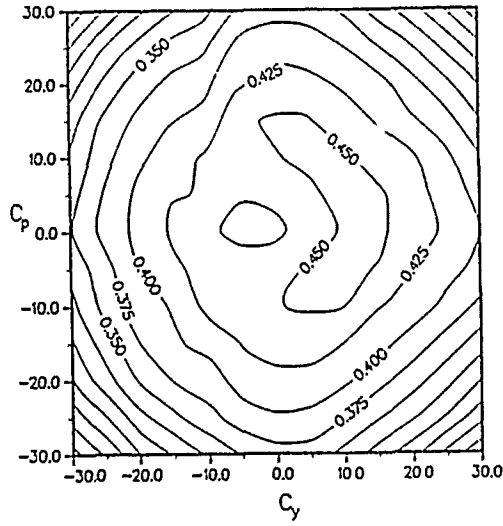


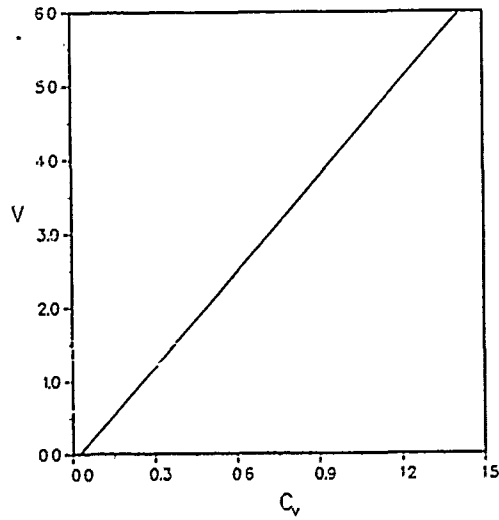
Figure 9. Five-hole pitot probe coordinate system.



(a) L vs. K

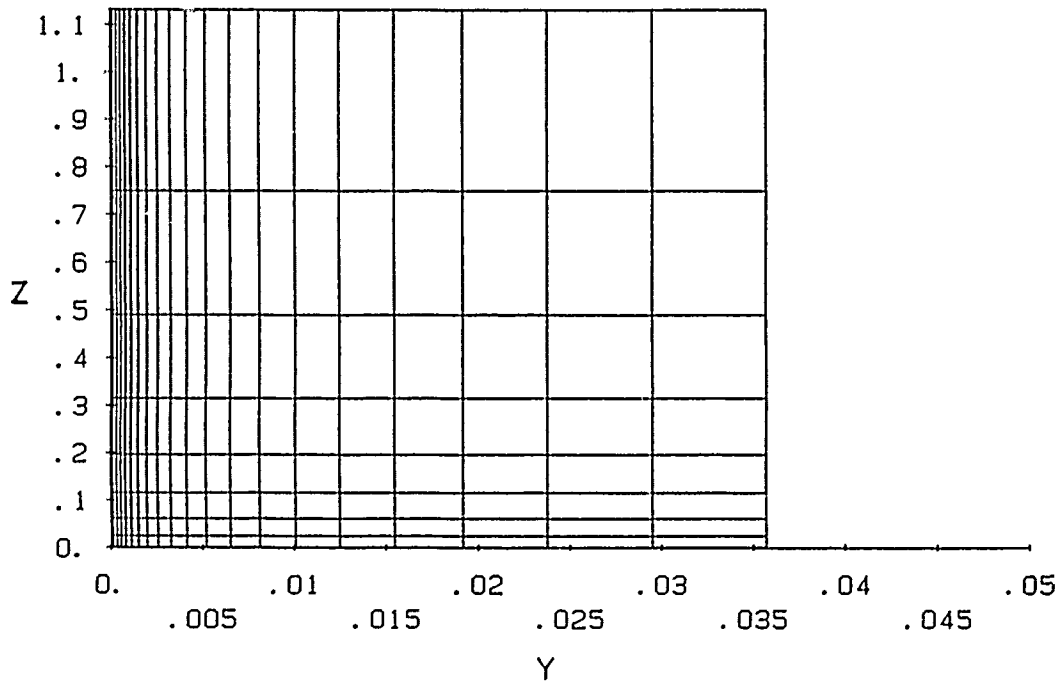
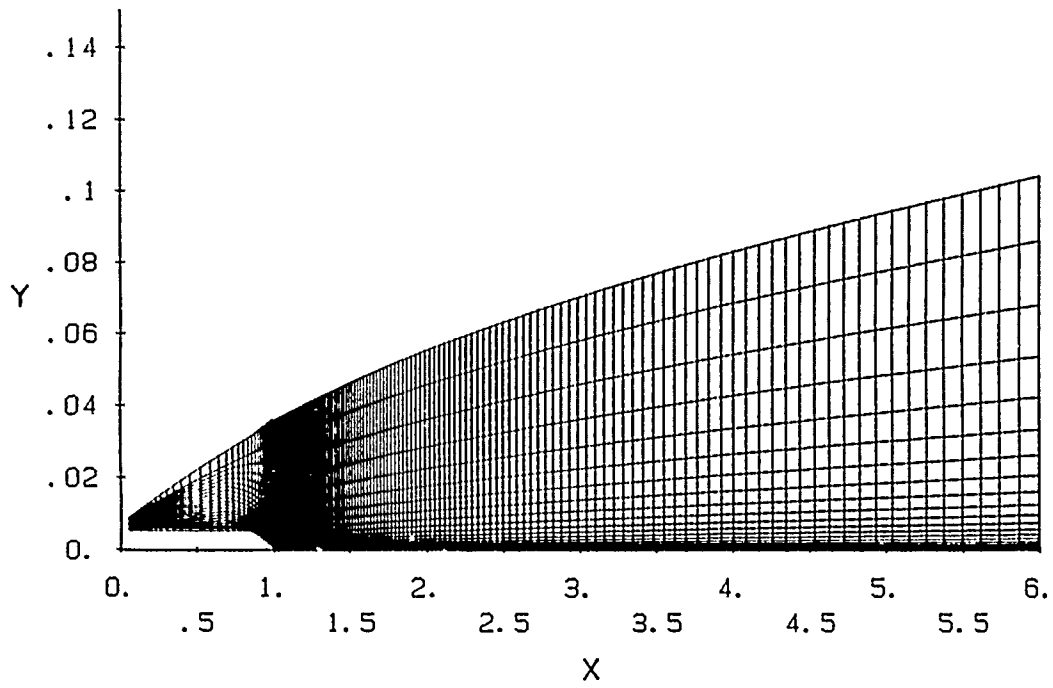


(b) M



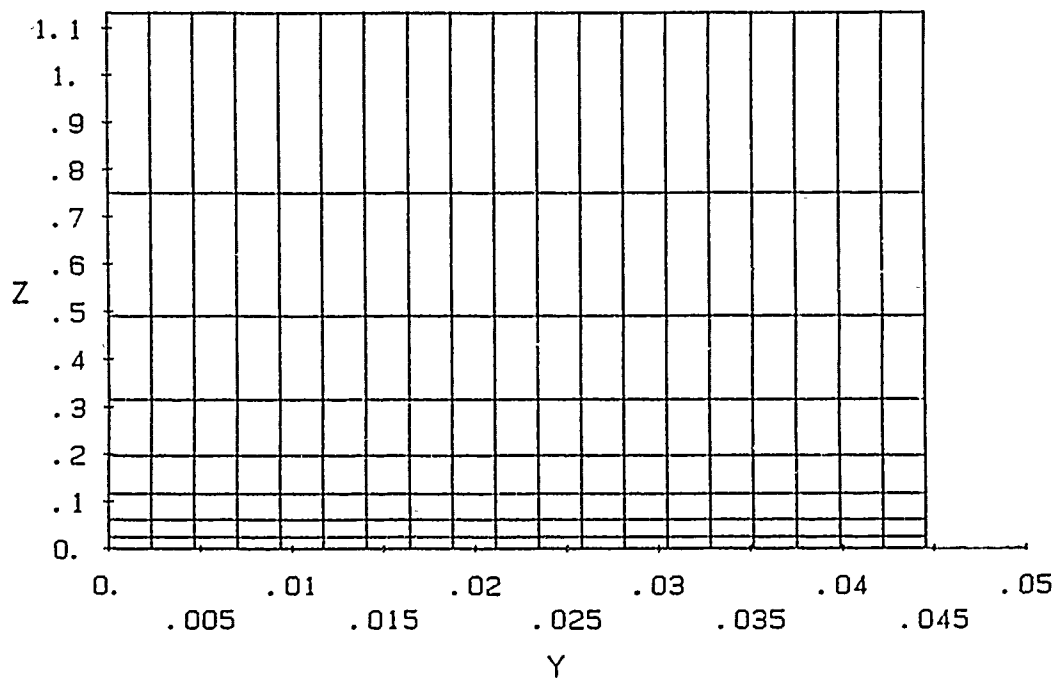
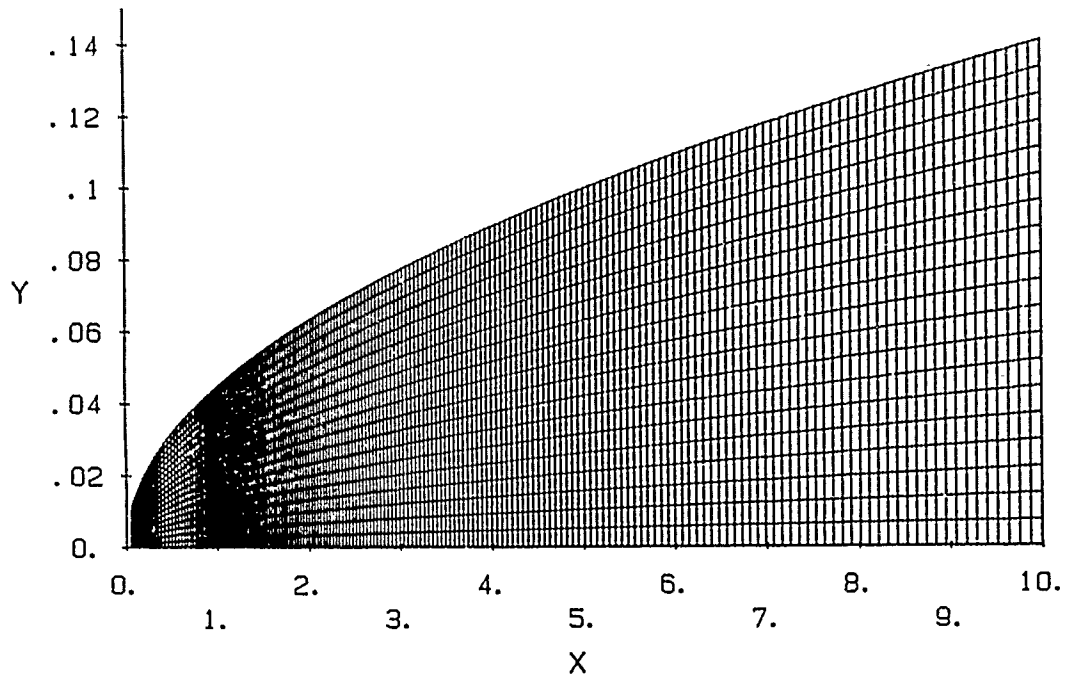
(c) dynamic calibration

Figure 10. Calibration coefficients.



(a) turbulent

Figure 11. Computational grids.

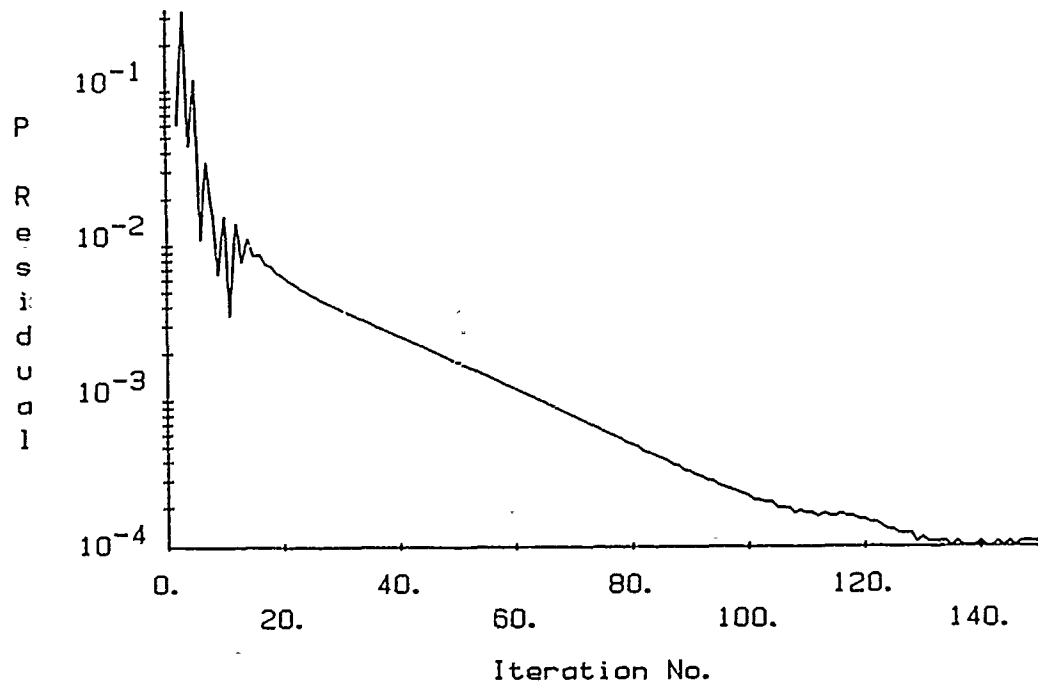


(b) laminar

Figure 11. (concluded).



(a) turbulent



(b) laminar

Figure 12. Convergence histories: $Ak = 0$.

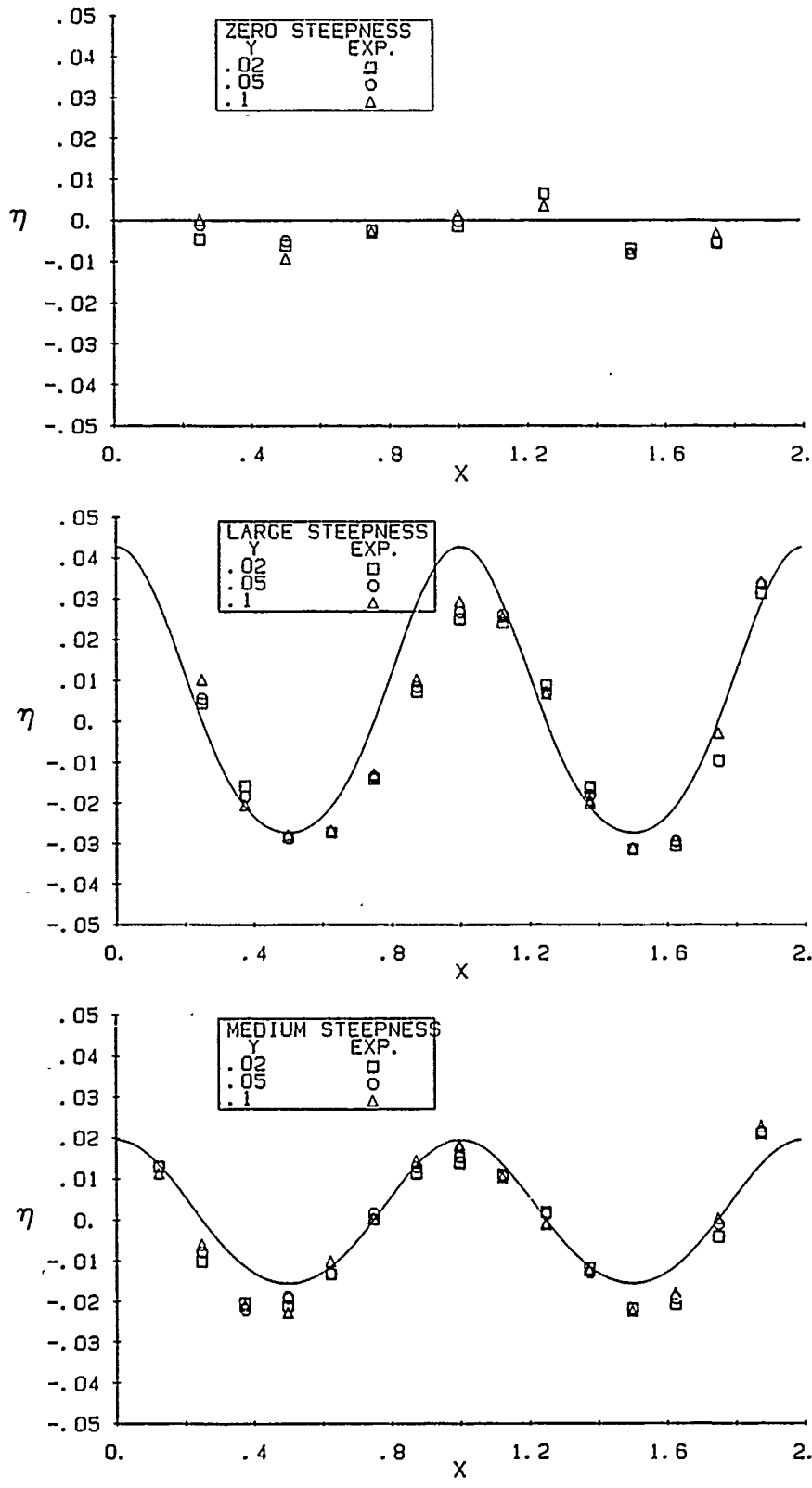
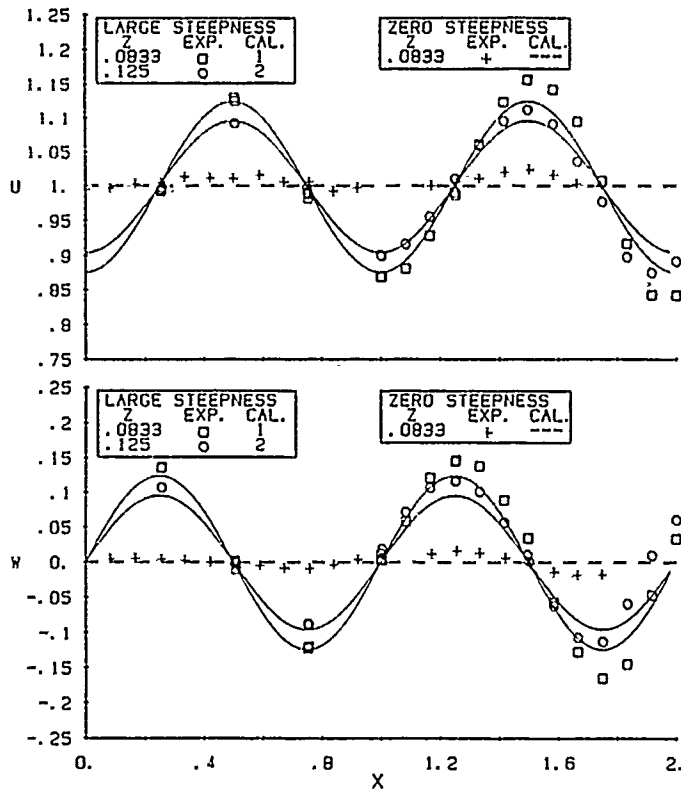
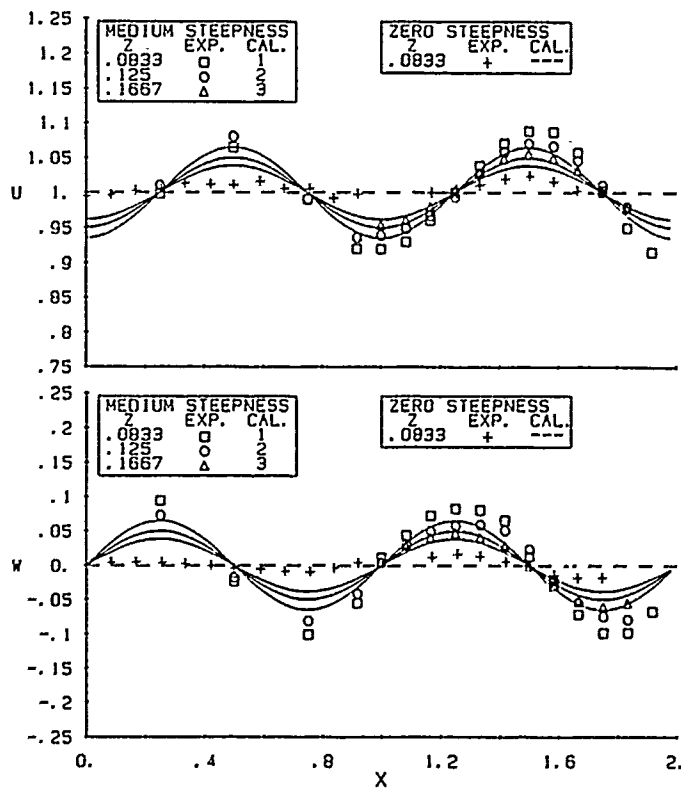


Figure 13. Wave elevations.



(a) large steepness



(b) medium steepness

Figure 14. Without-plate velocities.

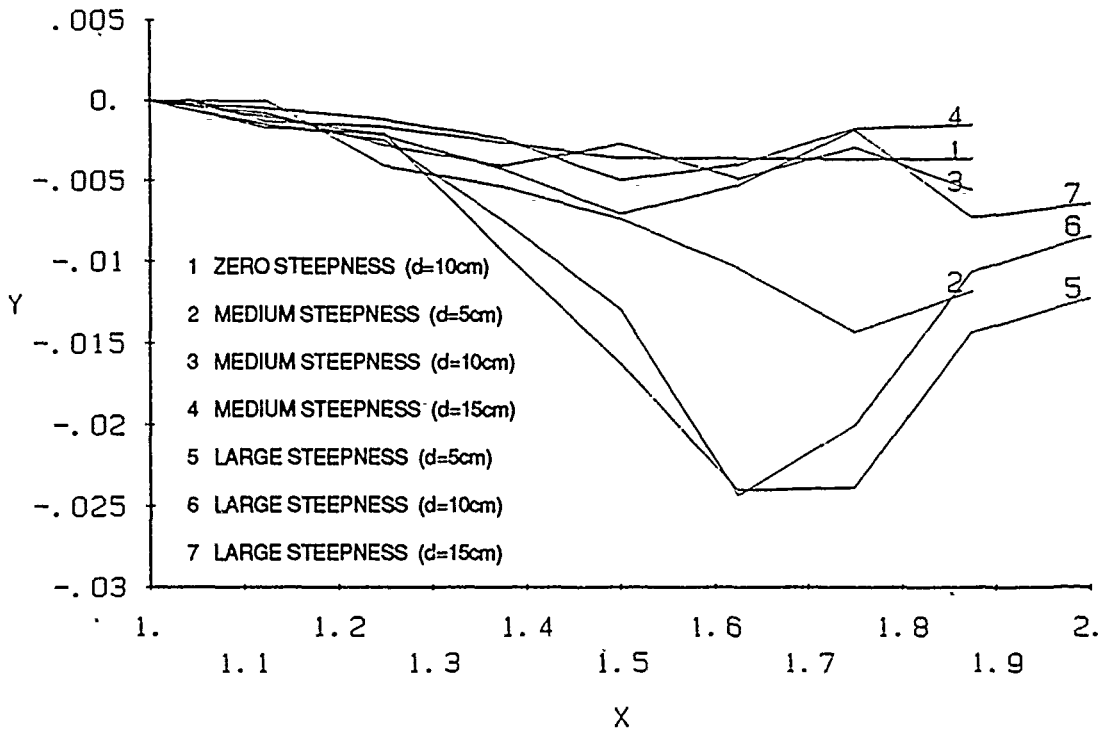


Figure 15. Location of wake centerplane.

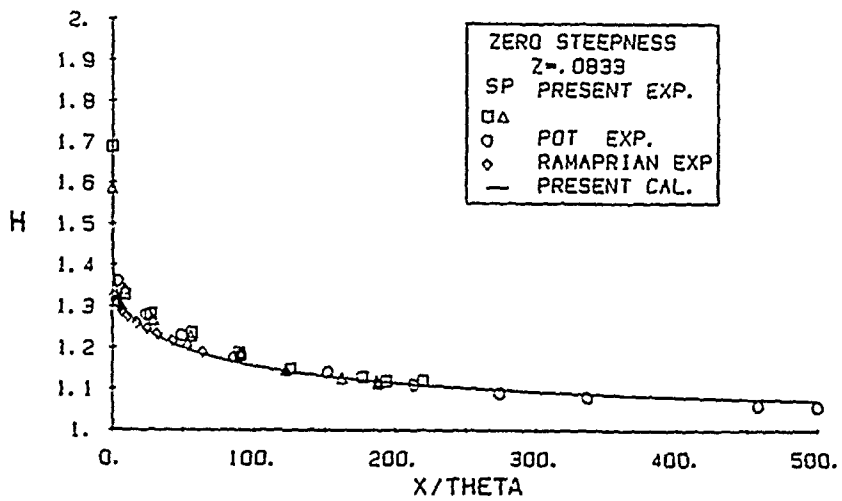
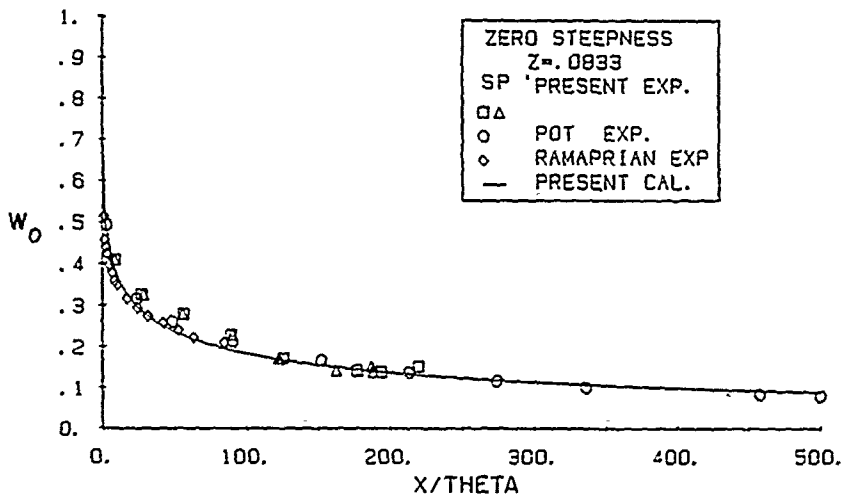
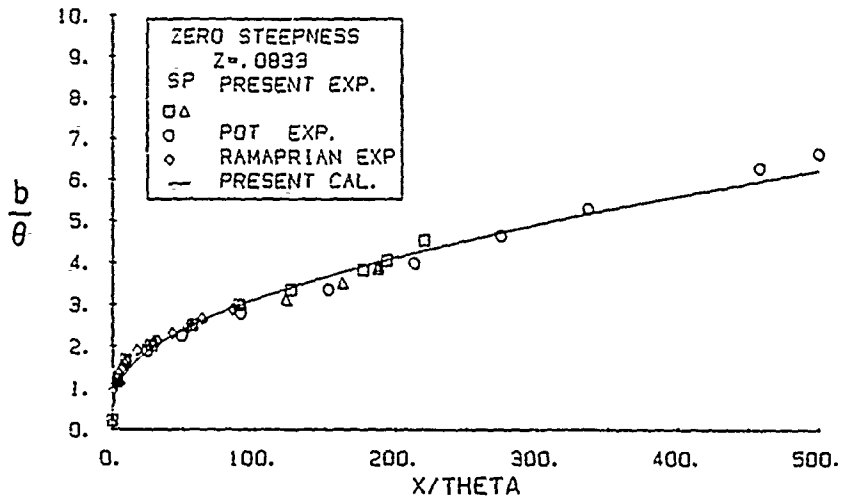


Figure 16. Wake parameters.

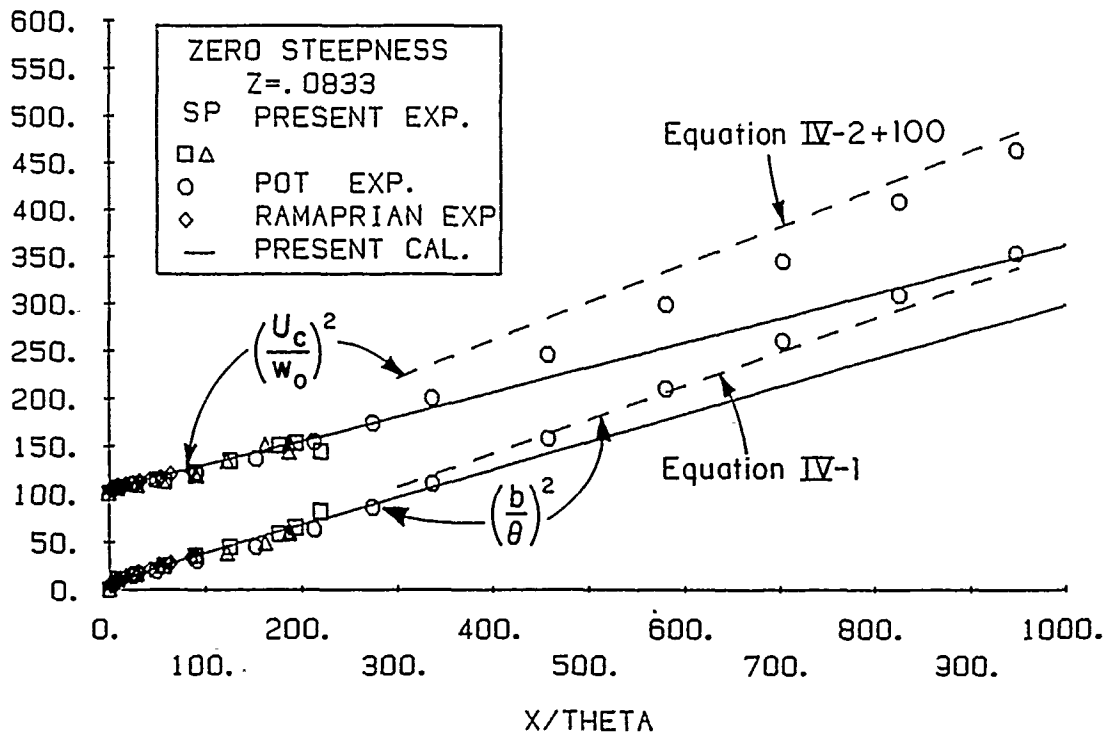
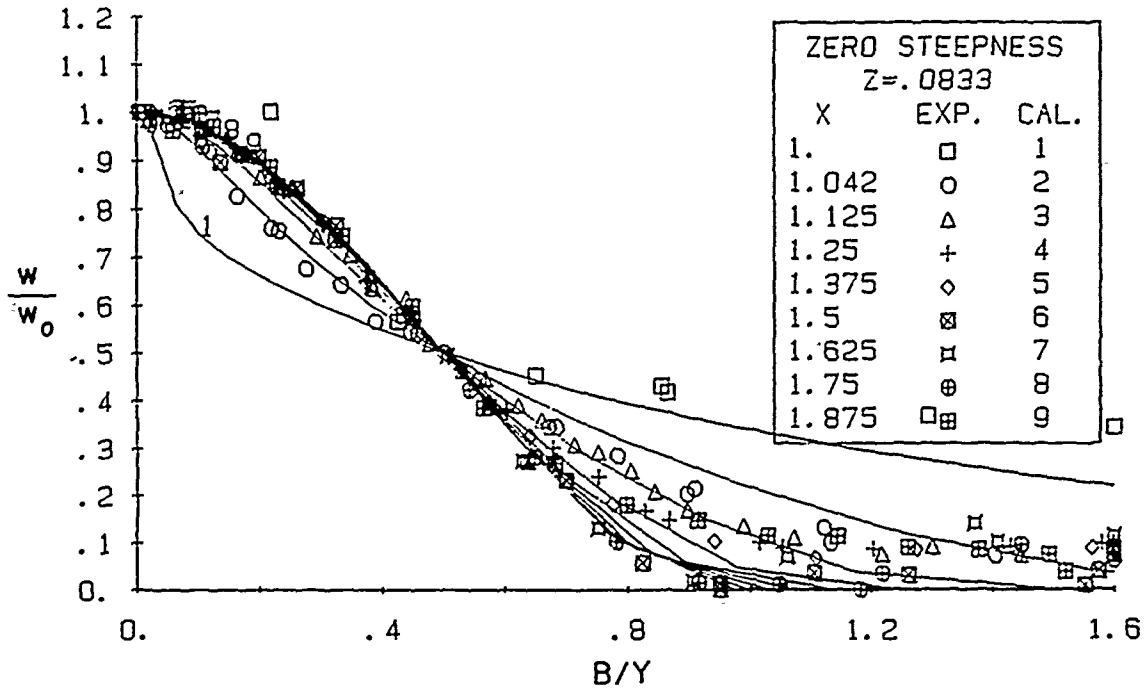
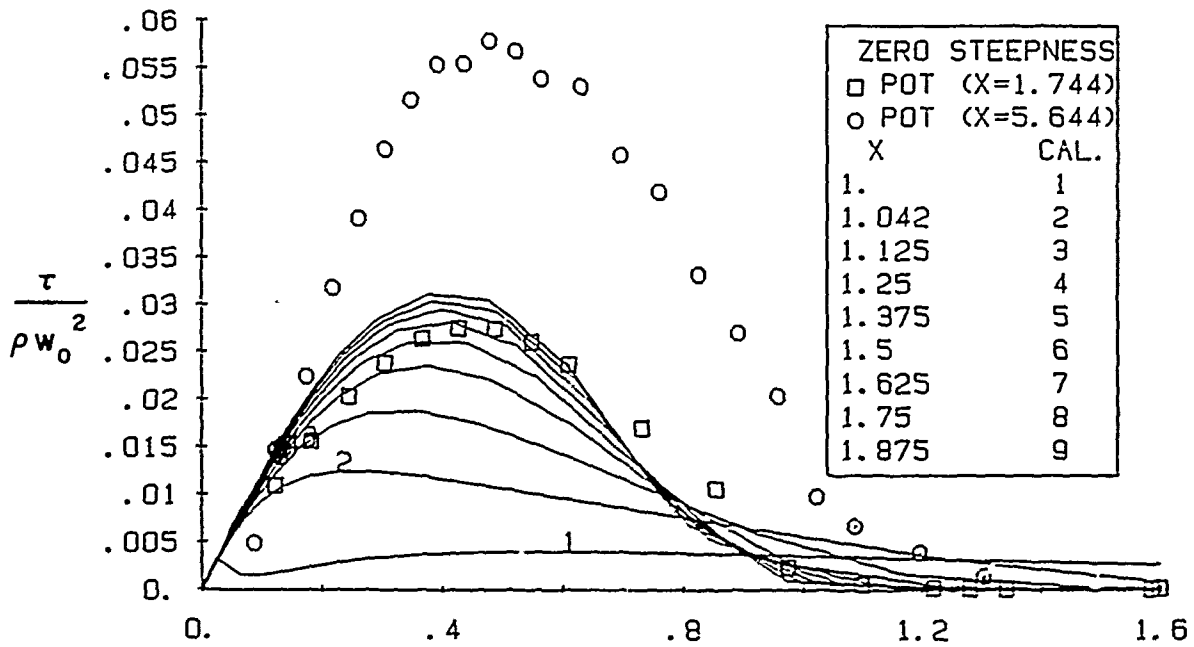


Figure 17. Asymptotic half-power laws.



(a) velocity defect



(b) stress

Figure 18. Asymptotic profiles.

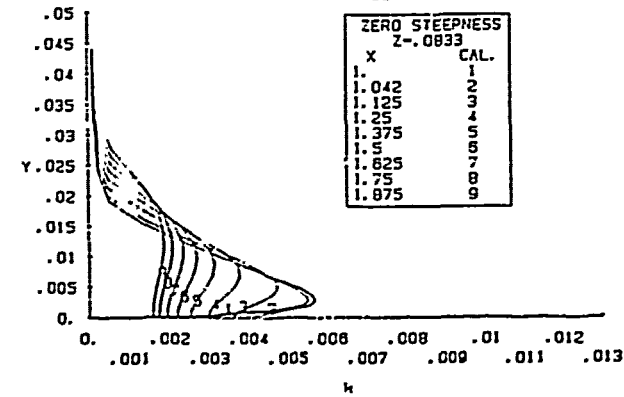
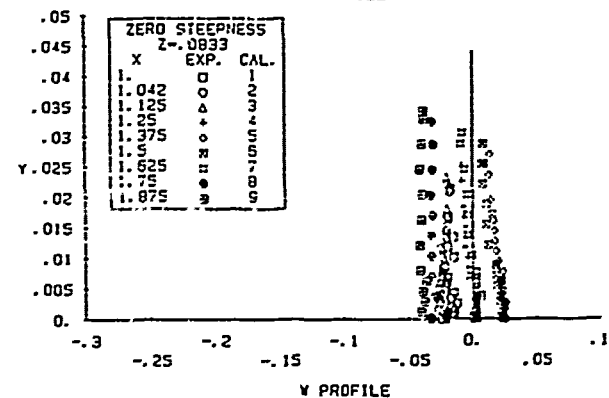
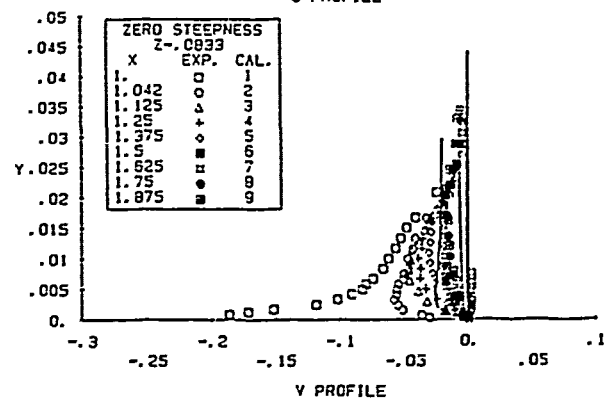
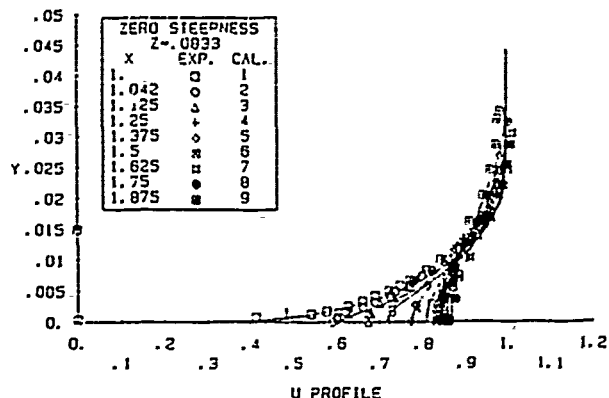


Figure 19. Velocity and turbulent kinetic energy profiles: zero steepness.

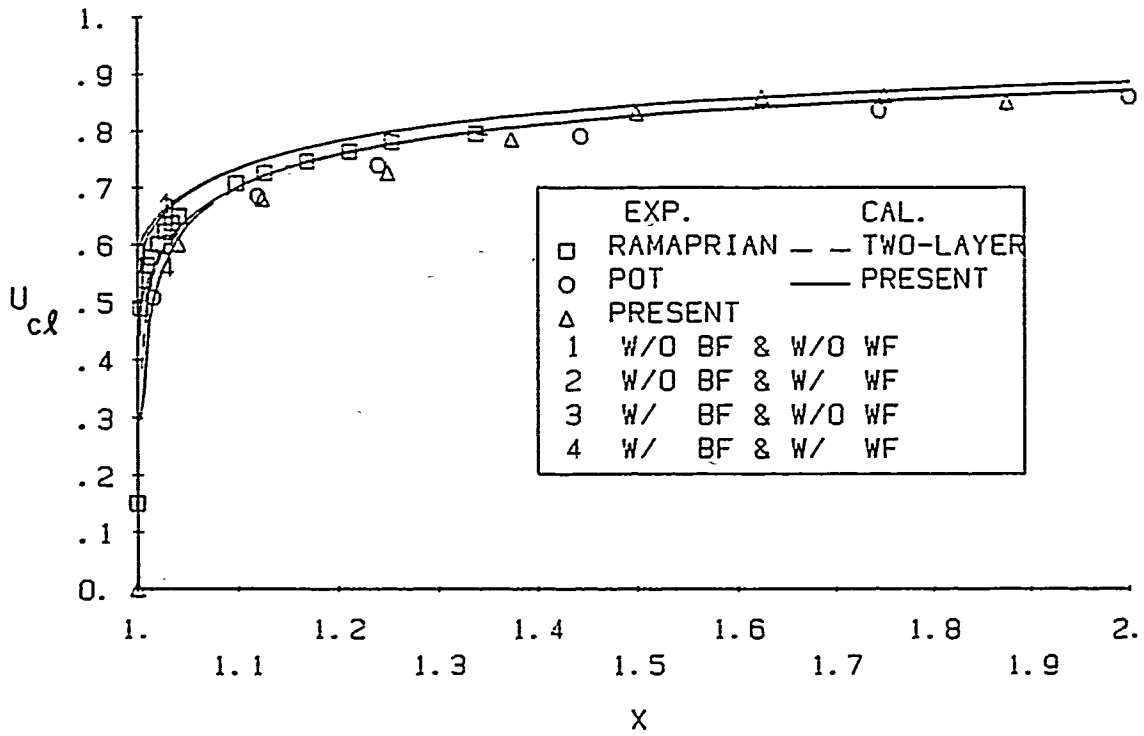


Figure 20. Wake centerline velocity.

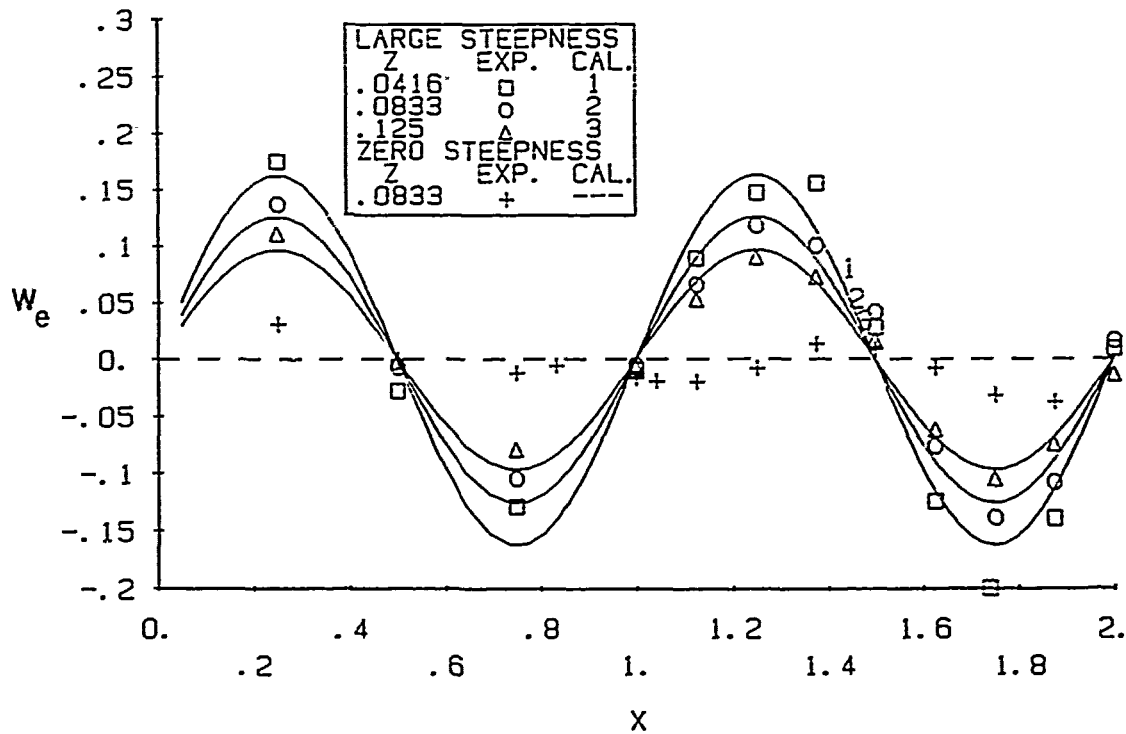
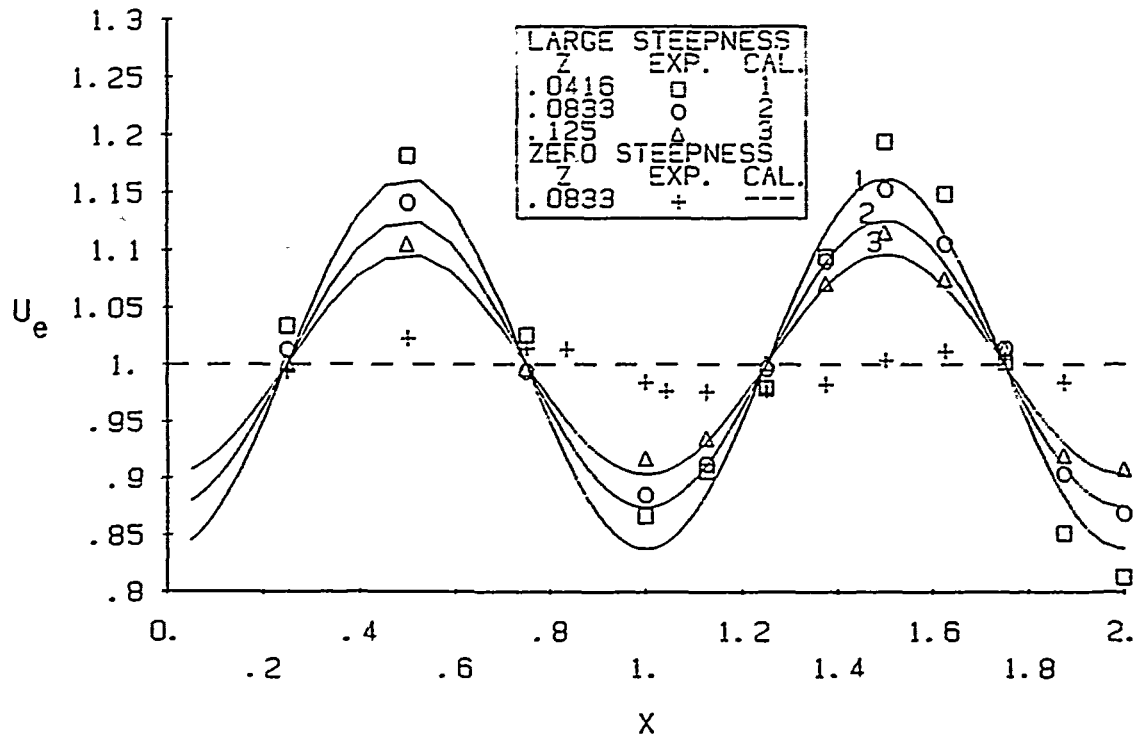


Figure 21. Edge velocities: large steepness.

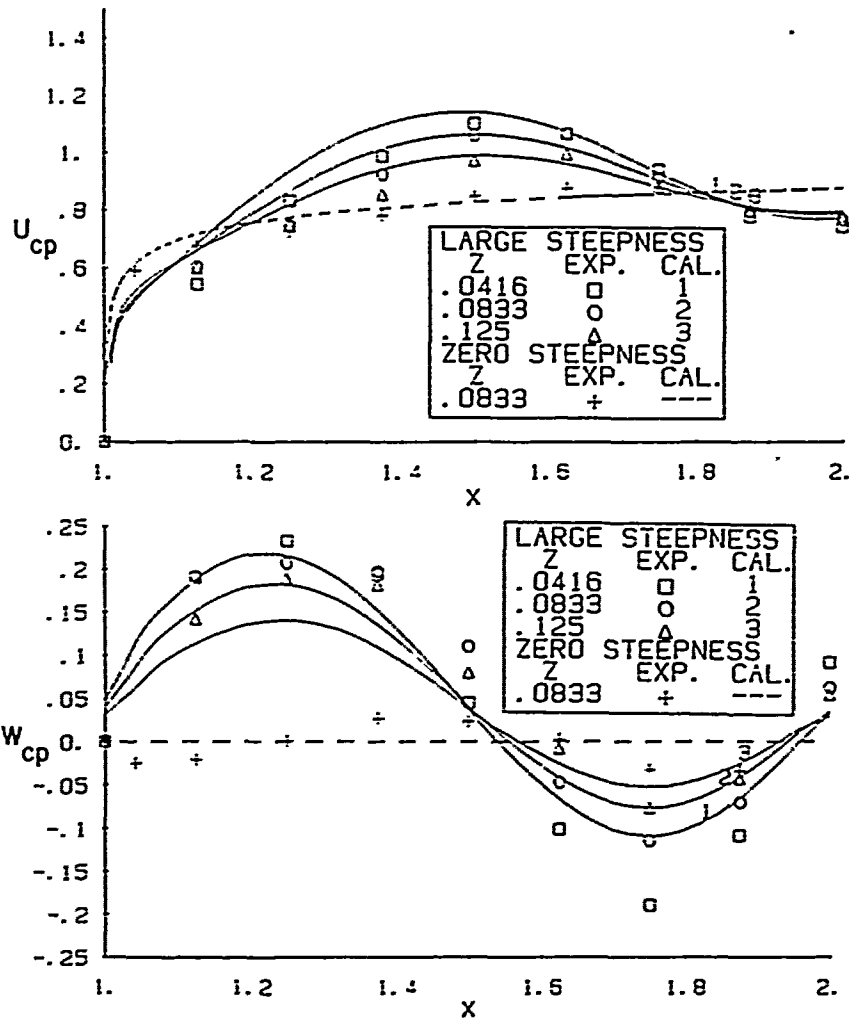


Figure 22. Wake centerplane velocities: large steepness.

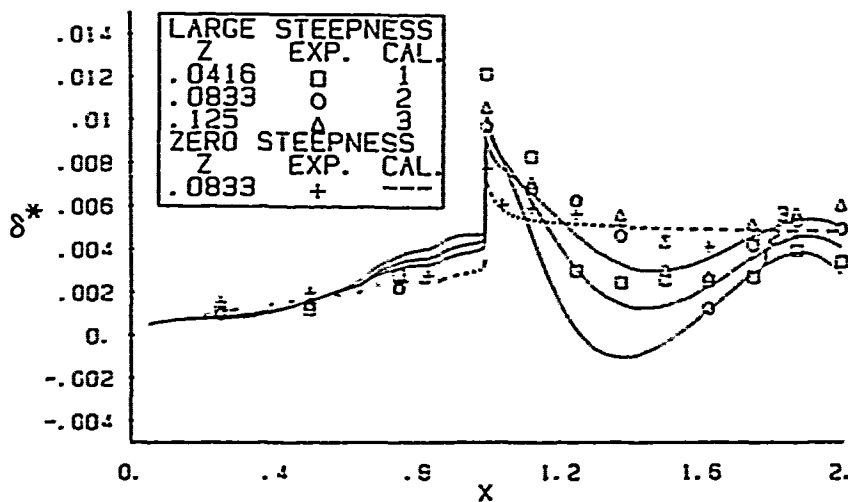
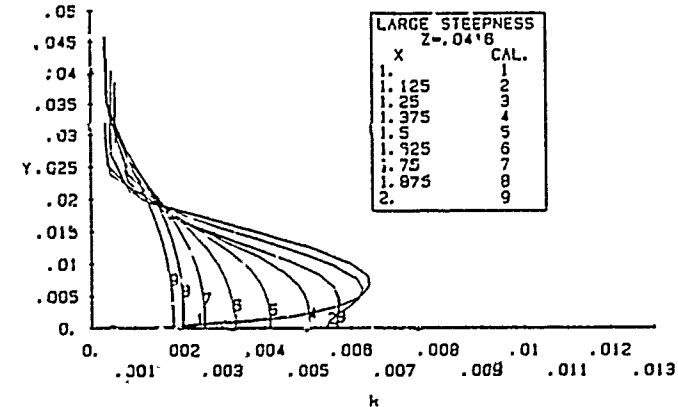
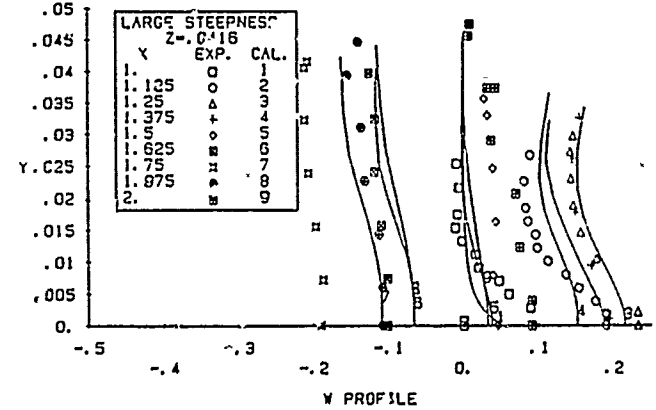
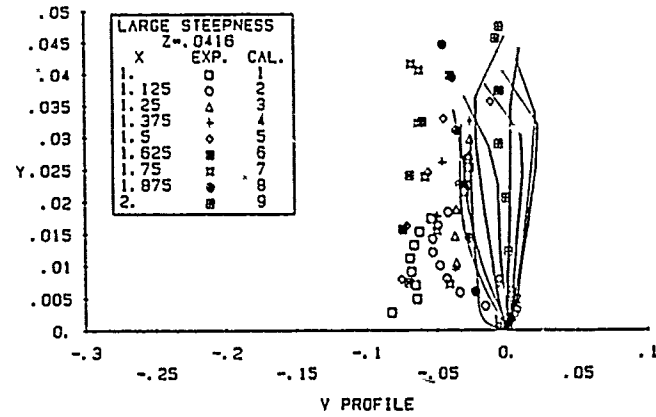
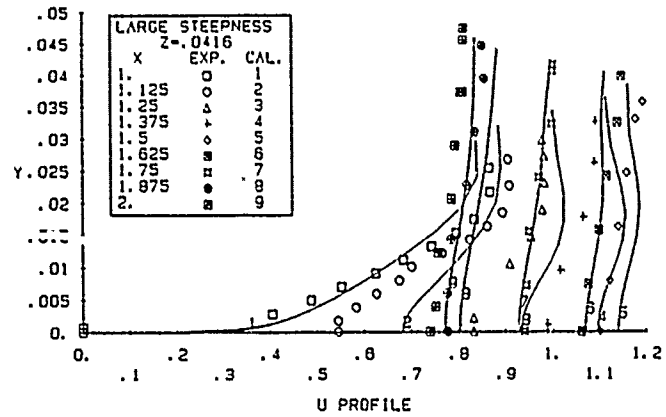
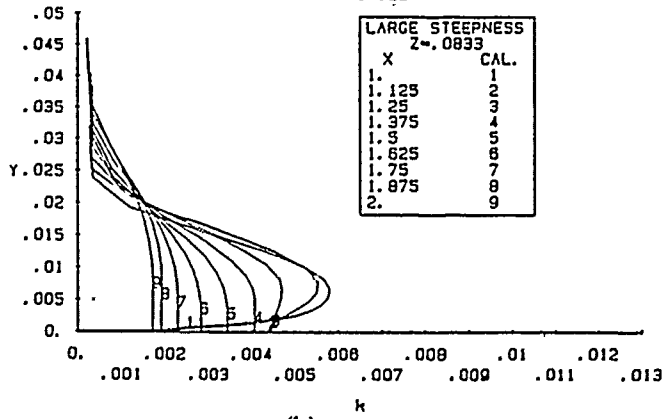
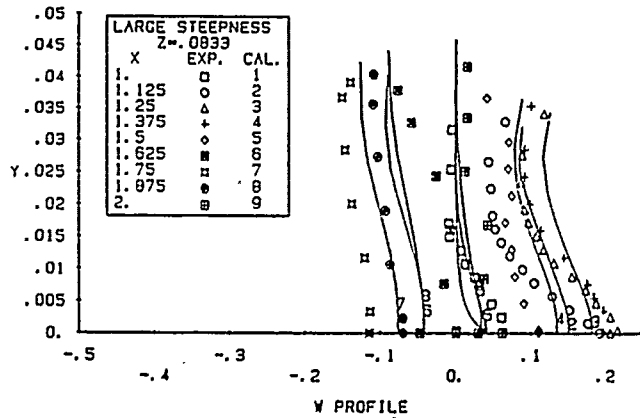
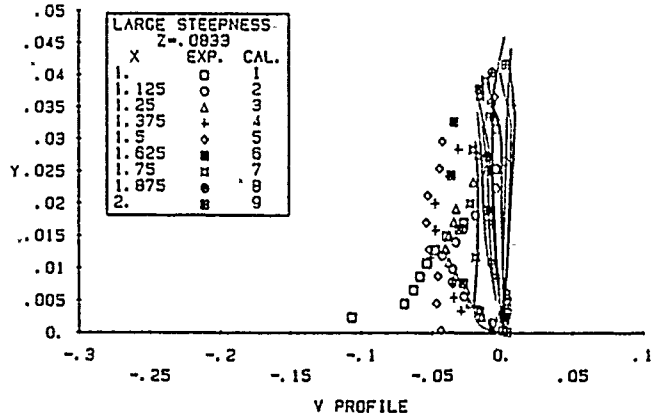
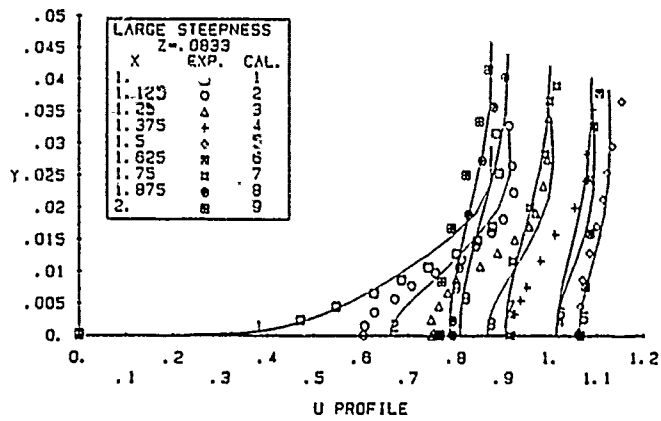


Figure 23. Streamwise displacement thickness: large steepness.



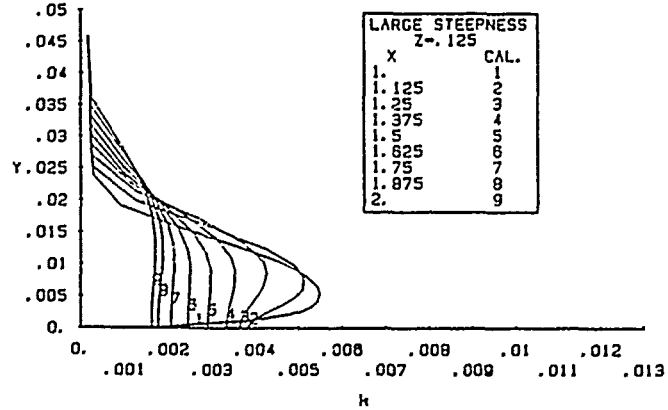
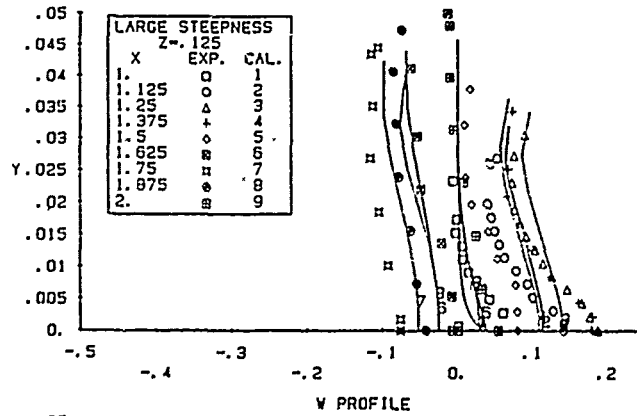
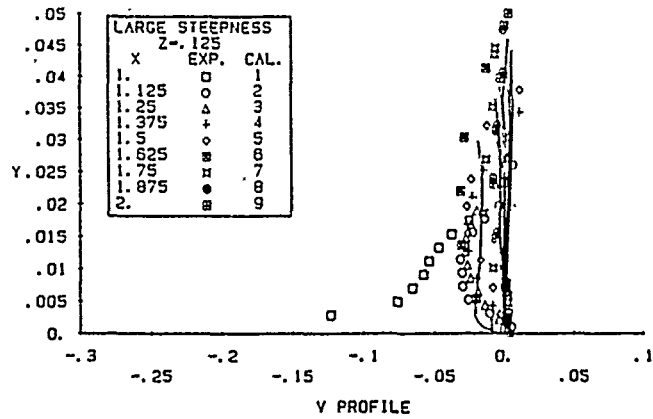
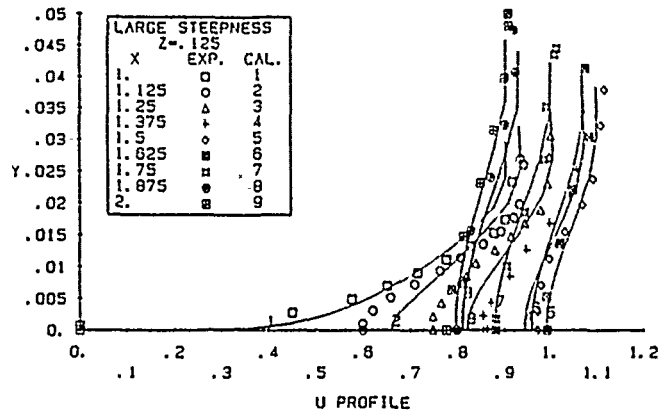
(a)

Figure 24. Velocity and turbulent kinetic energy profiles: large steepness.



(b)

Figure 24. (continued).



(c)

Figure 24. (concluded).

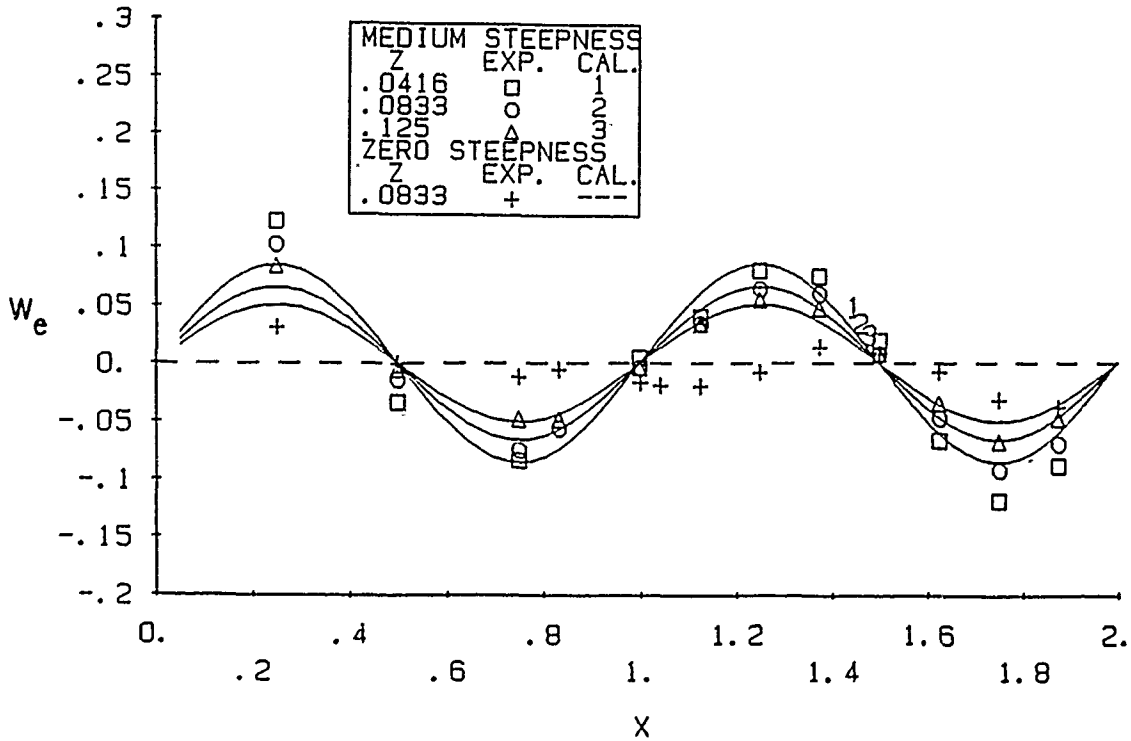
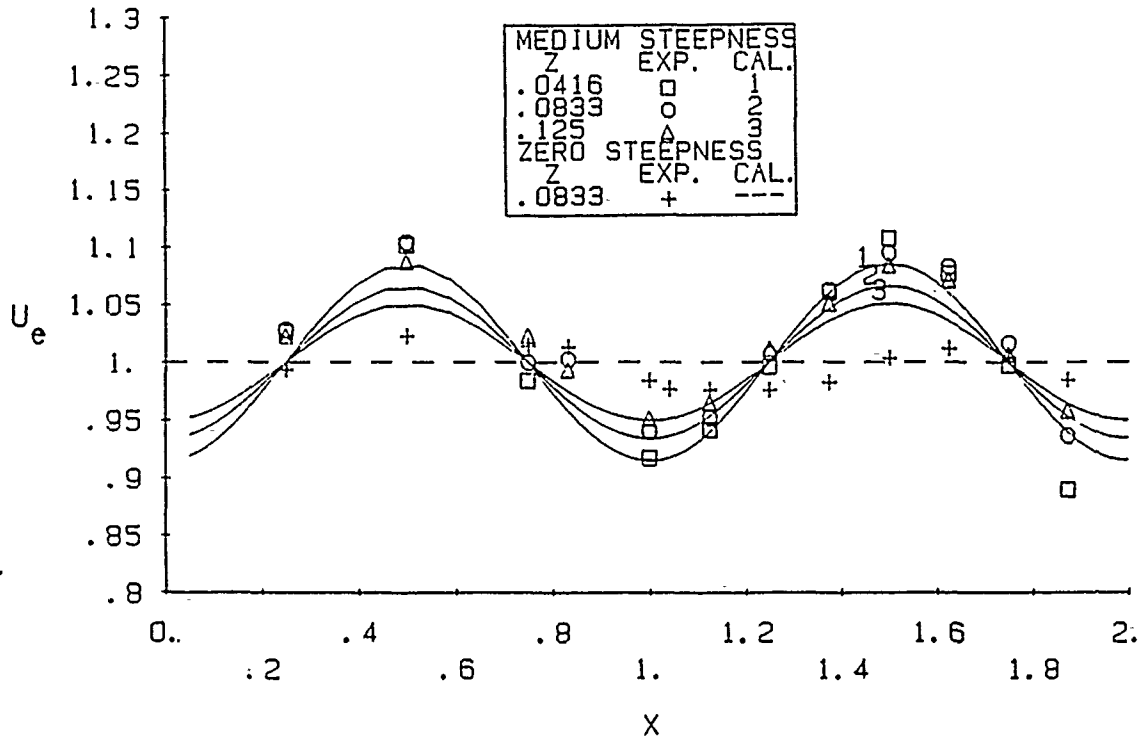


Figure 25. Edge velocities: medium steepness.

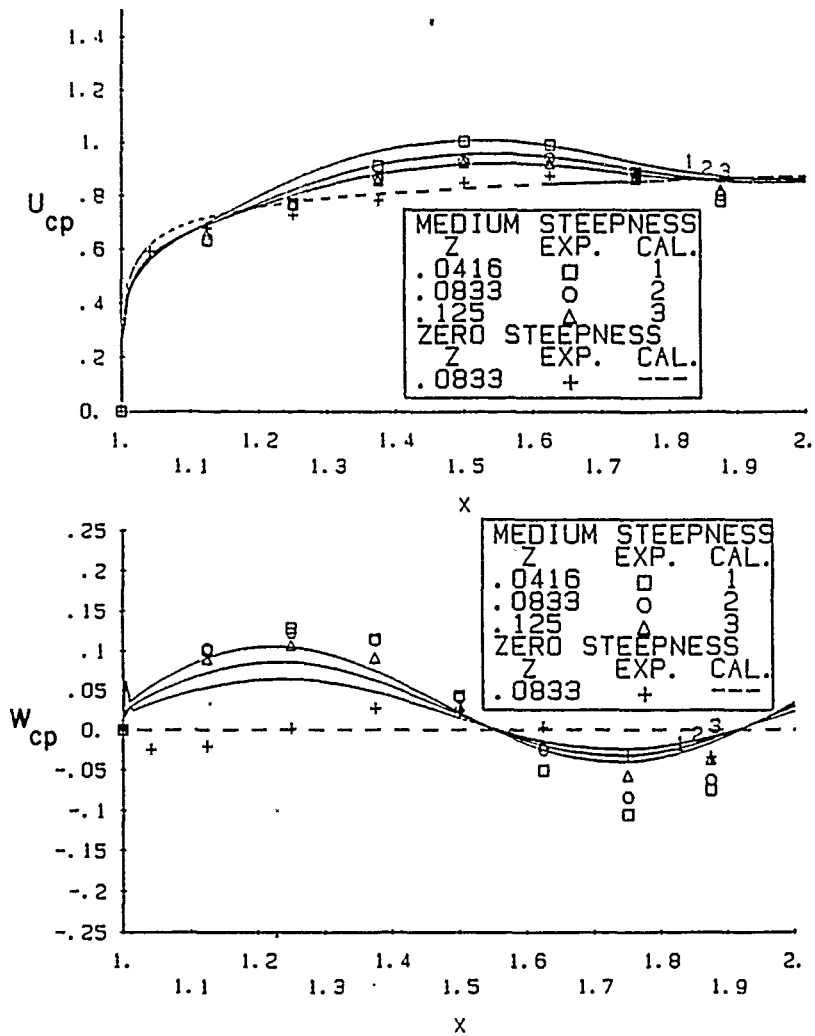


Figure 26. Wake centerplane velocities: medium steepness.

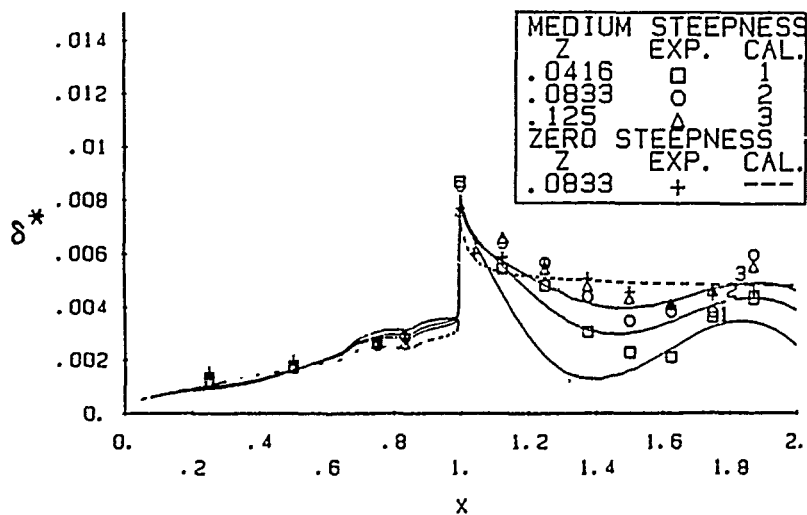
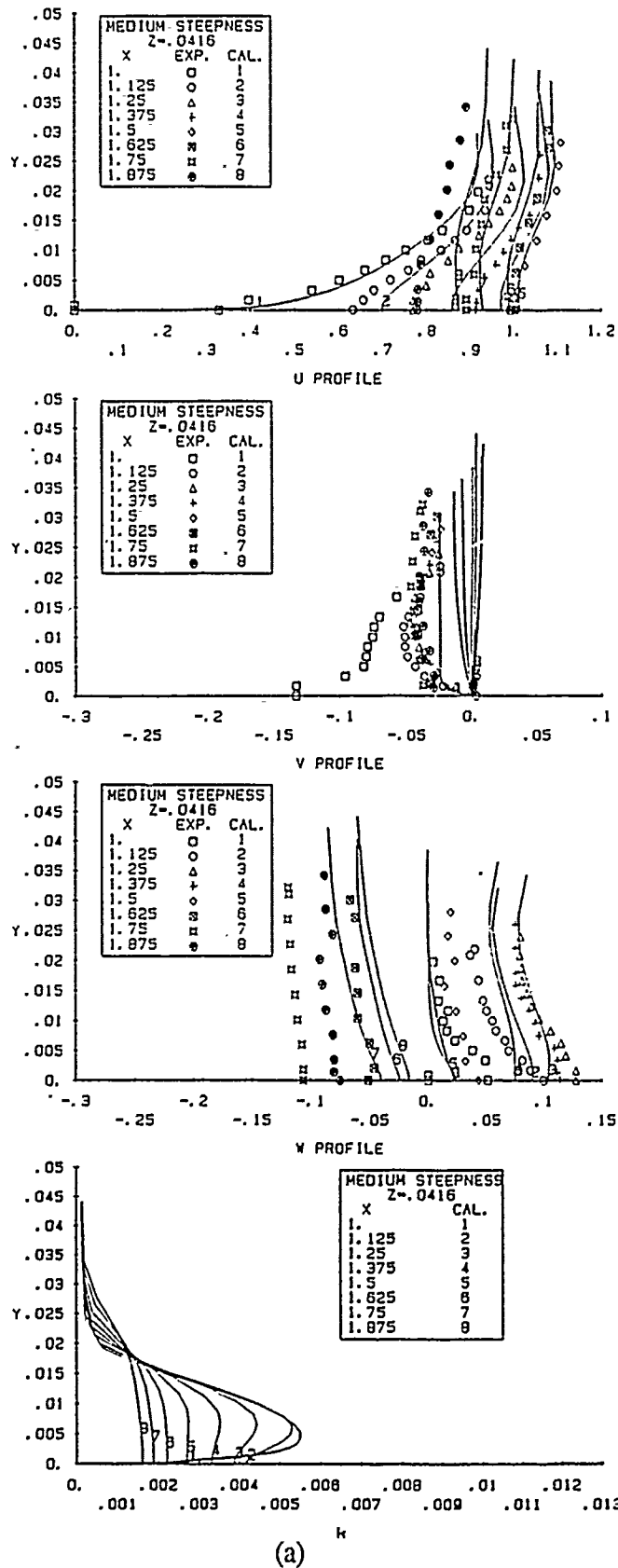
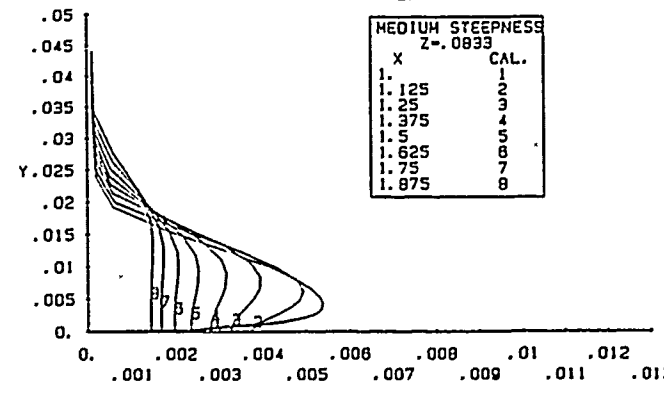
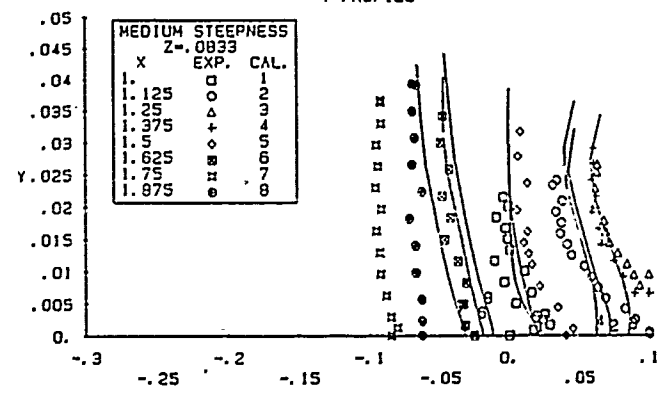
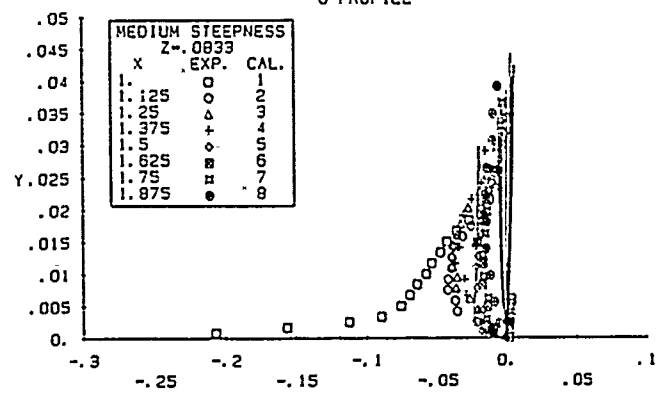
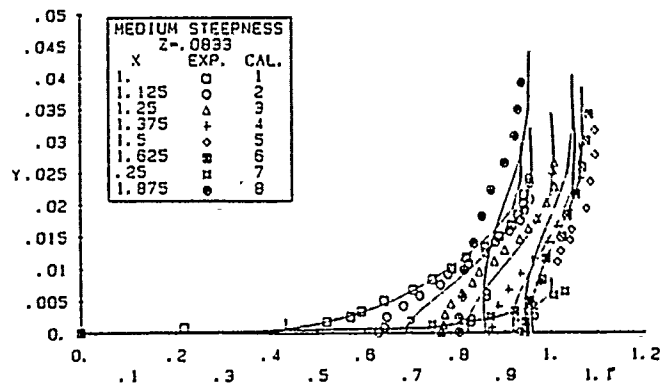


Figure 27. Streamwise displacement thickness: medium steepness.



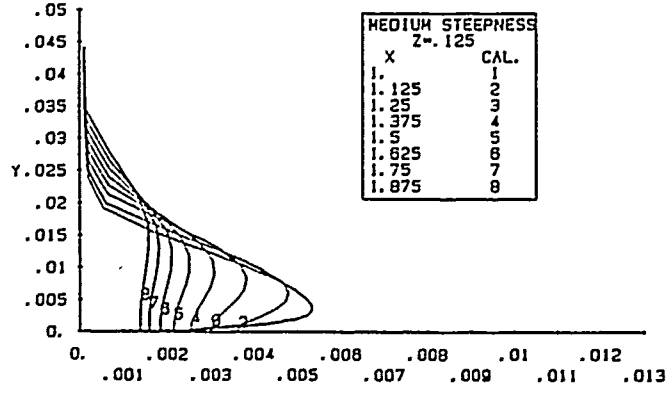
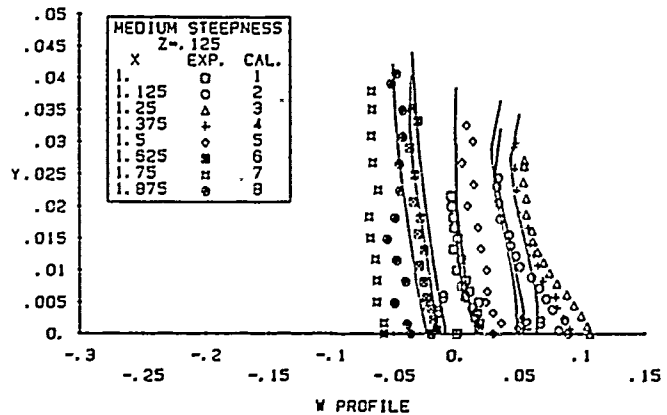
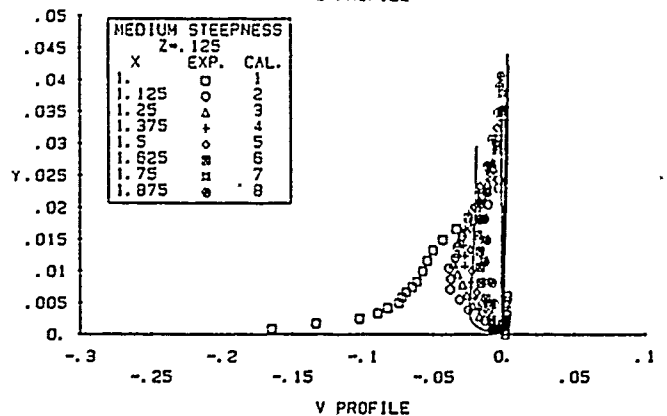
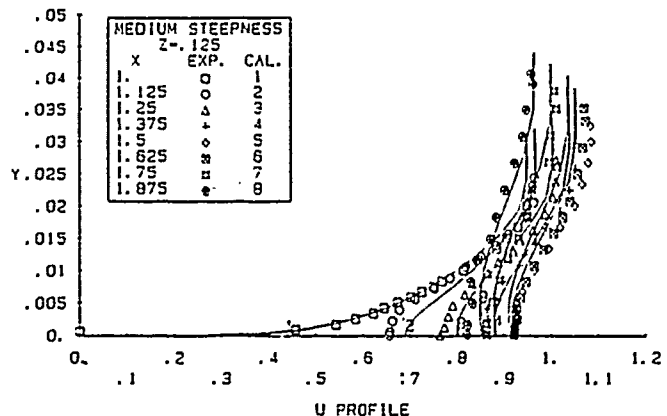
(a)

Figure 28. Velocity and turbulent kinetic energy profiles: medium steepness.



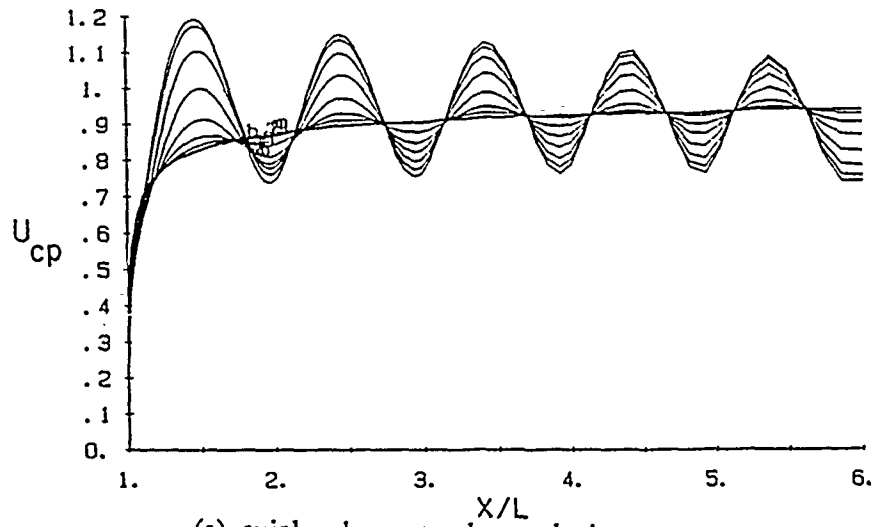
(b)

Figure 28. (continued).

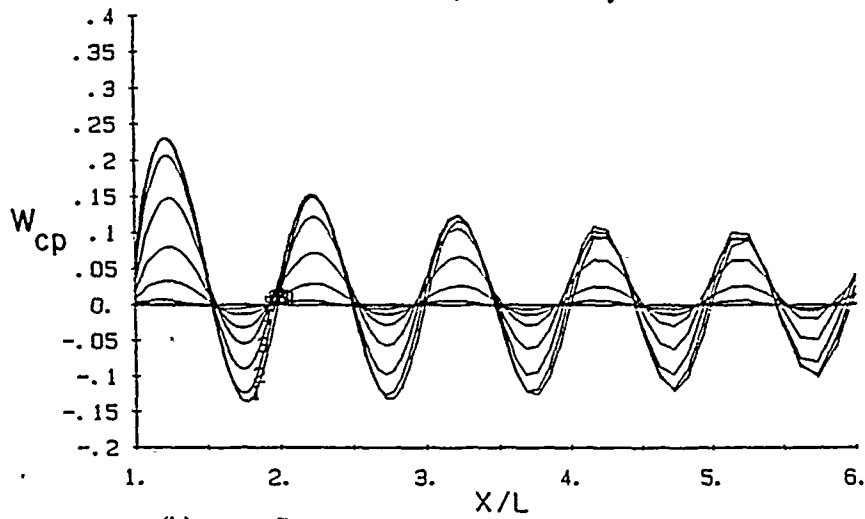


(c)

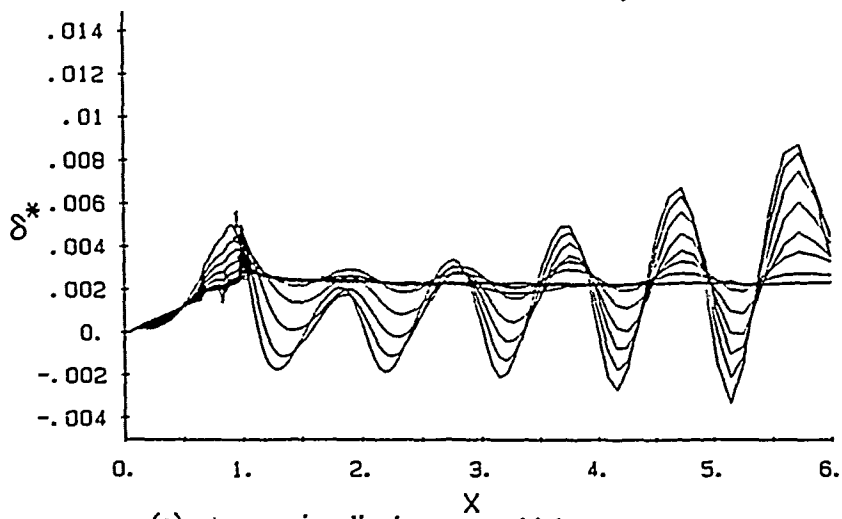
Figure 28. (concluded).



(a) axial wake centerplane velocity

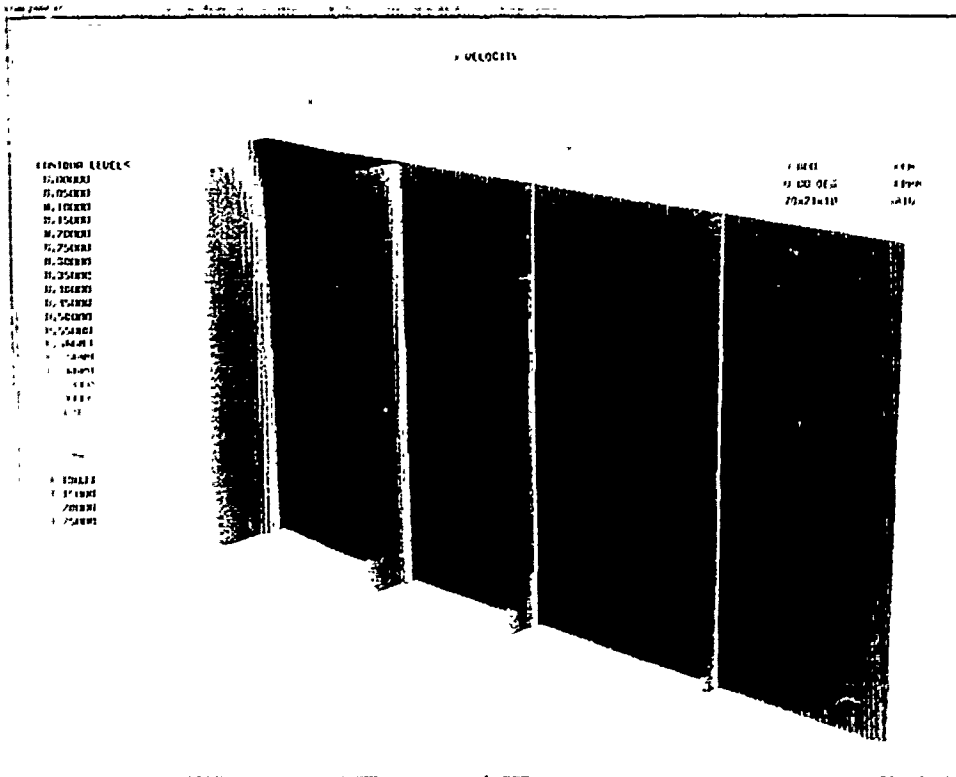


(b) crossflow wake centerplane velocity

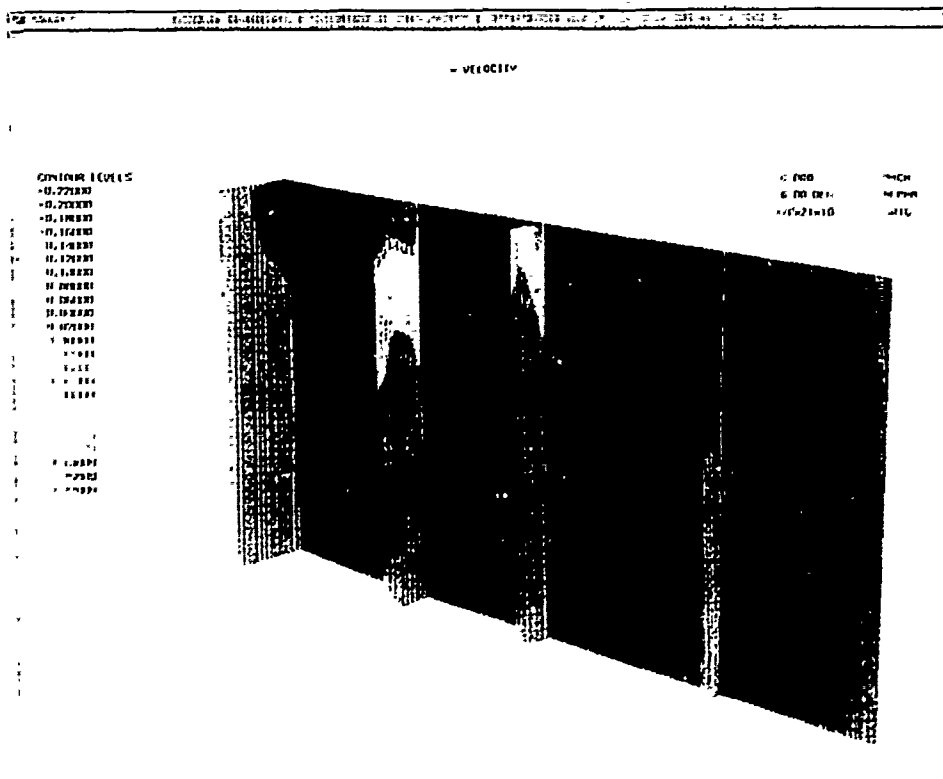


(c) streamwise displacement thickness

Figure 29. Global turbulent solution: $Ak = .21$.

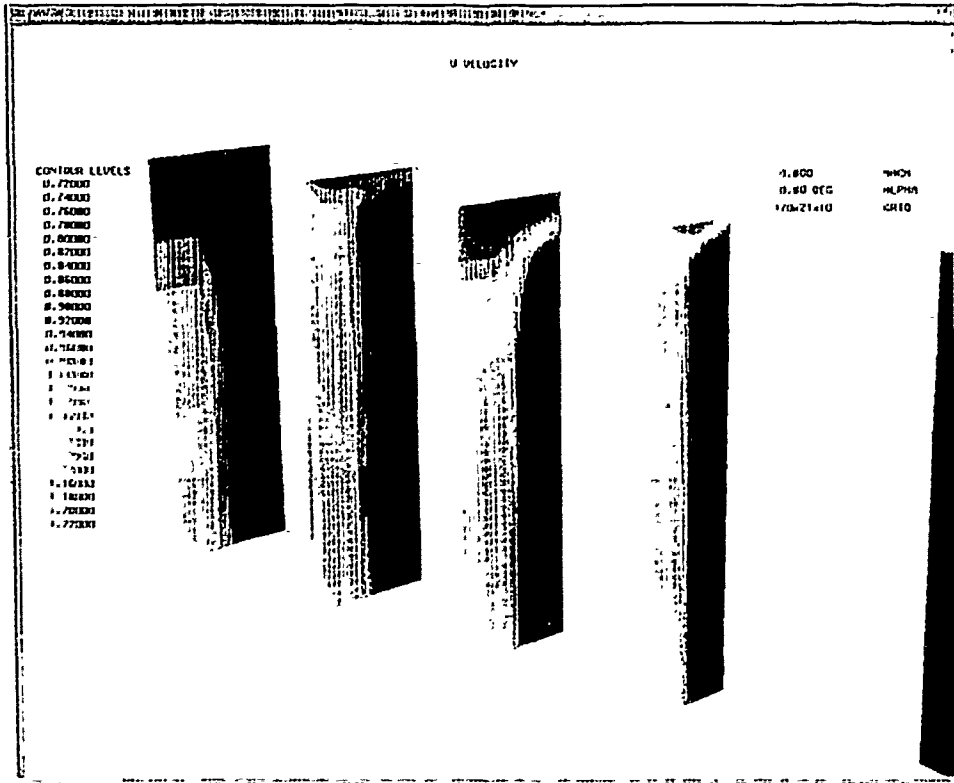


(a) axial velocity

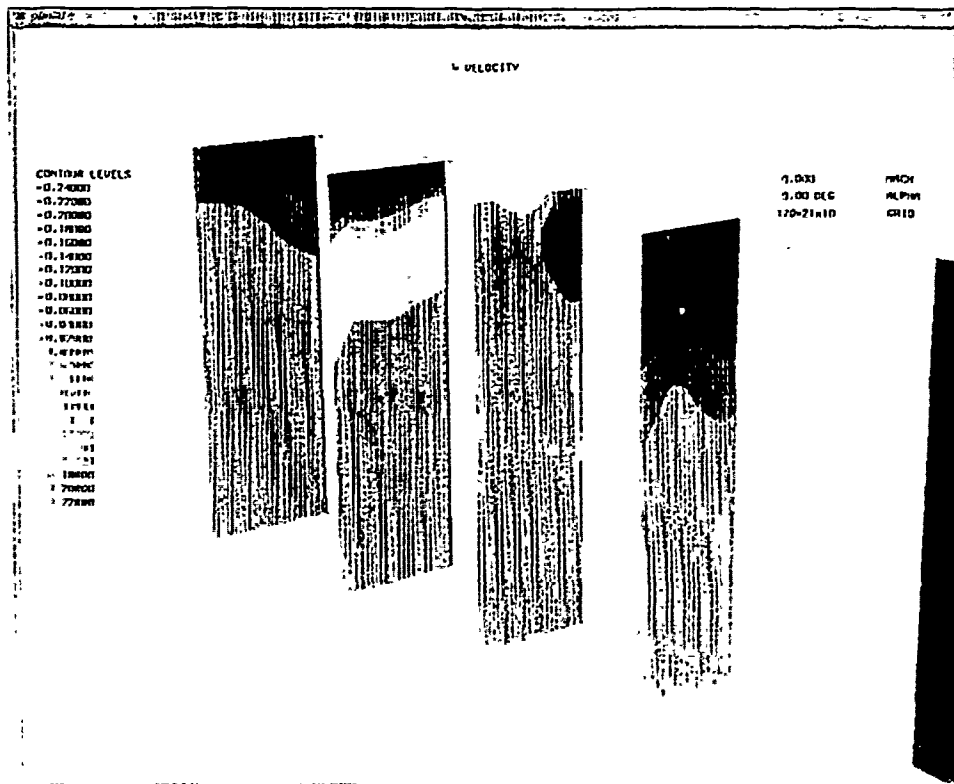


(b) crossflow velocity

Figure 30. Crossplane contours: boundary-layer region.

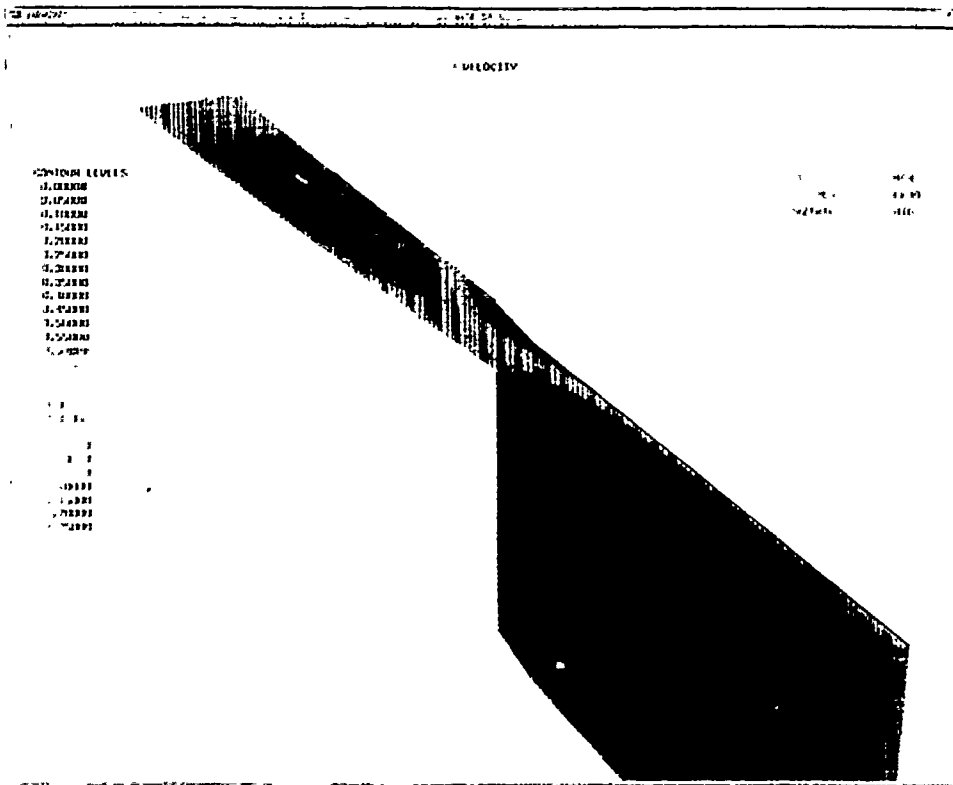


(a) axial velocity

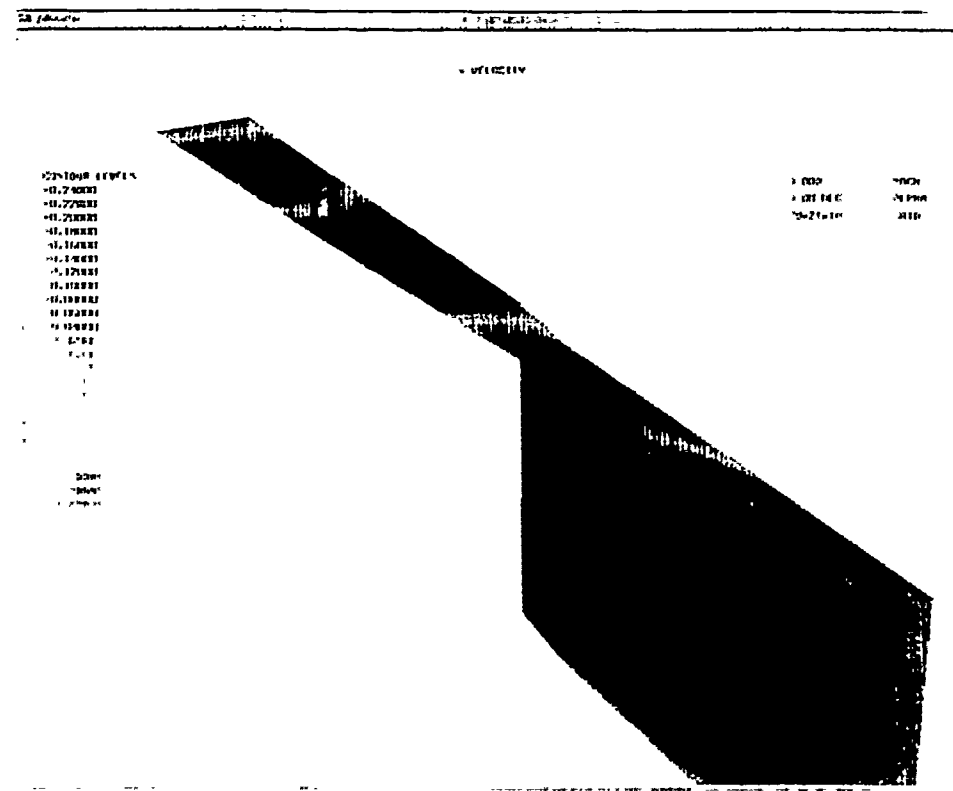


(b) crossflow velocity

Figure 31. Crossplane contours: near- and intermediate-wake regions.

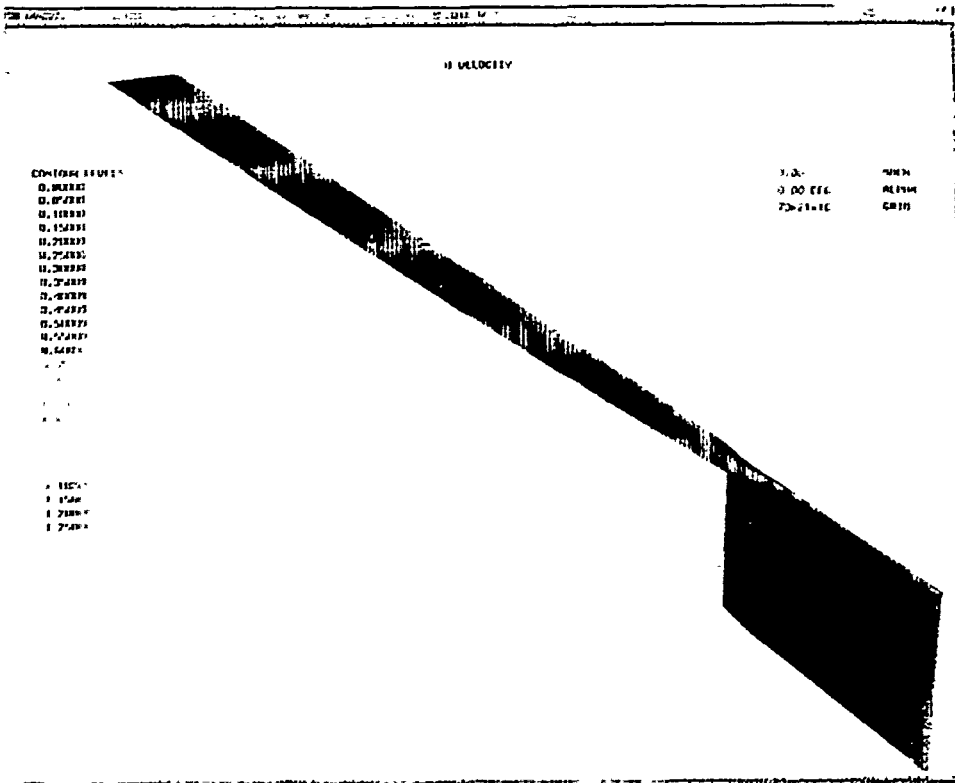


(a) axial velocity

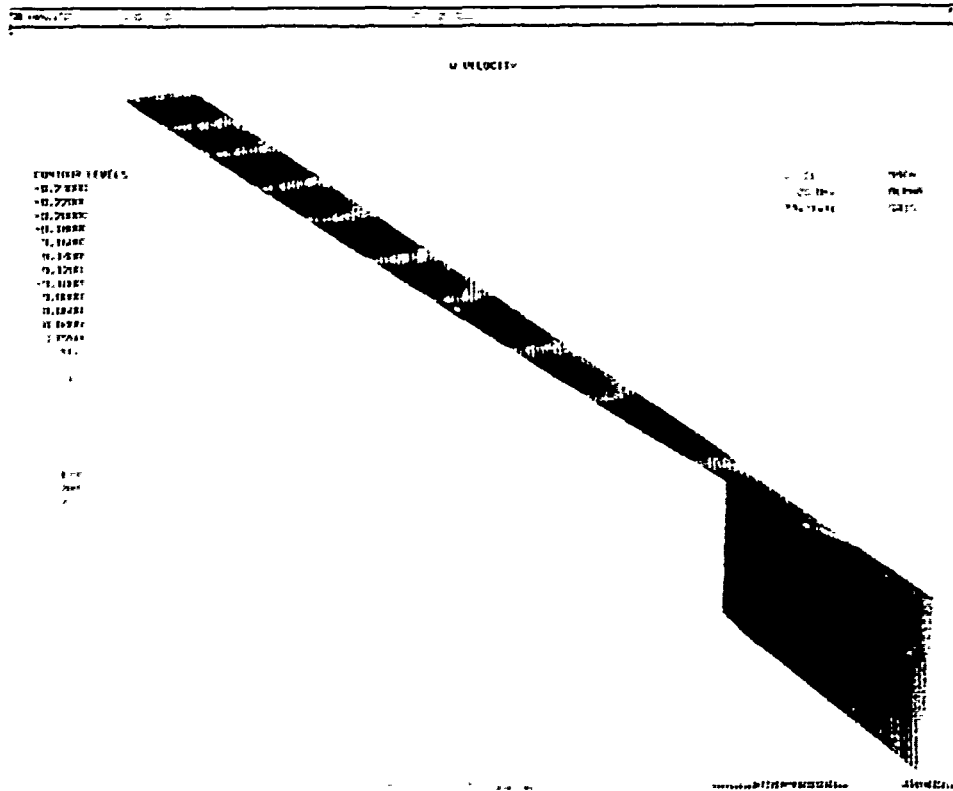


(b) crossflow velocity

Figure 32. Mean free-surface contours: boundary-layer and near- and intermediate-wake regions.

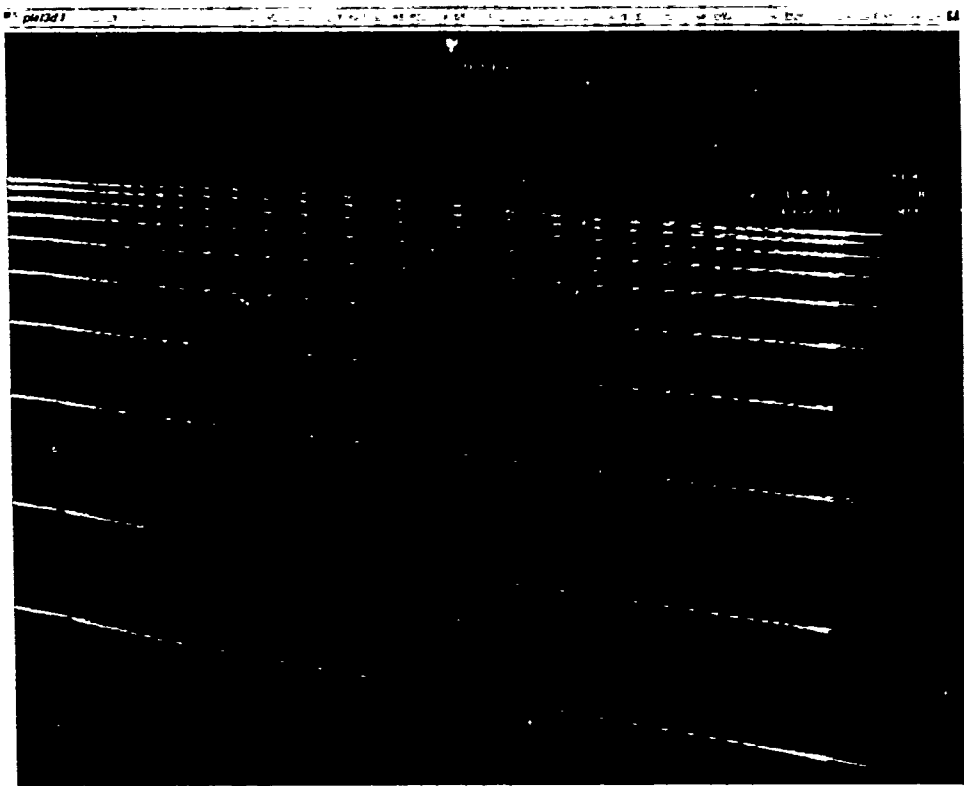


(a) axial velocity

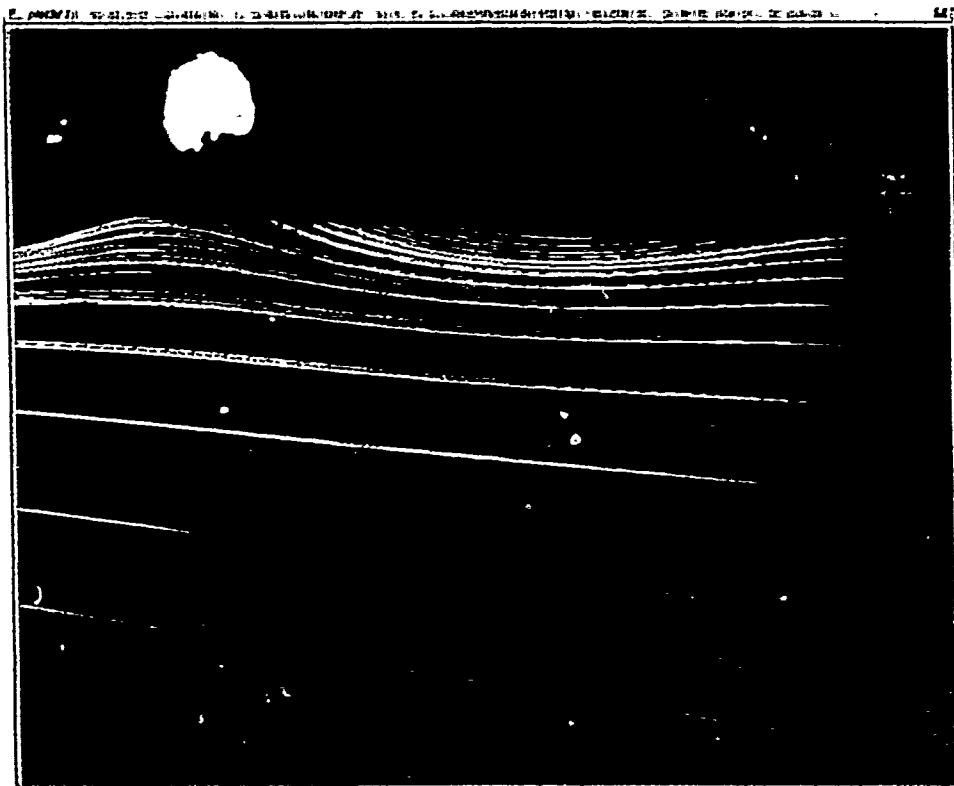


(b) crossflow velocity

Figure 33. Mean free-surface contours: complete solution domain.



(a) velocity vectors

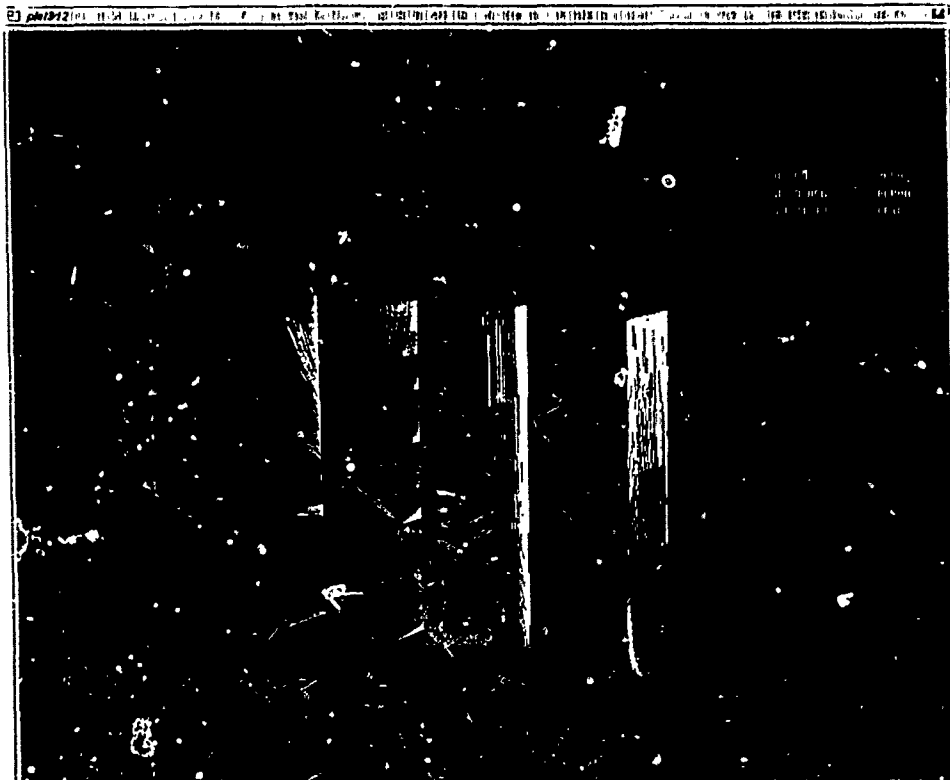


(b) streamlines

Figure 34. Plate and wake centerplane flow.

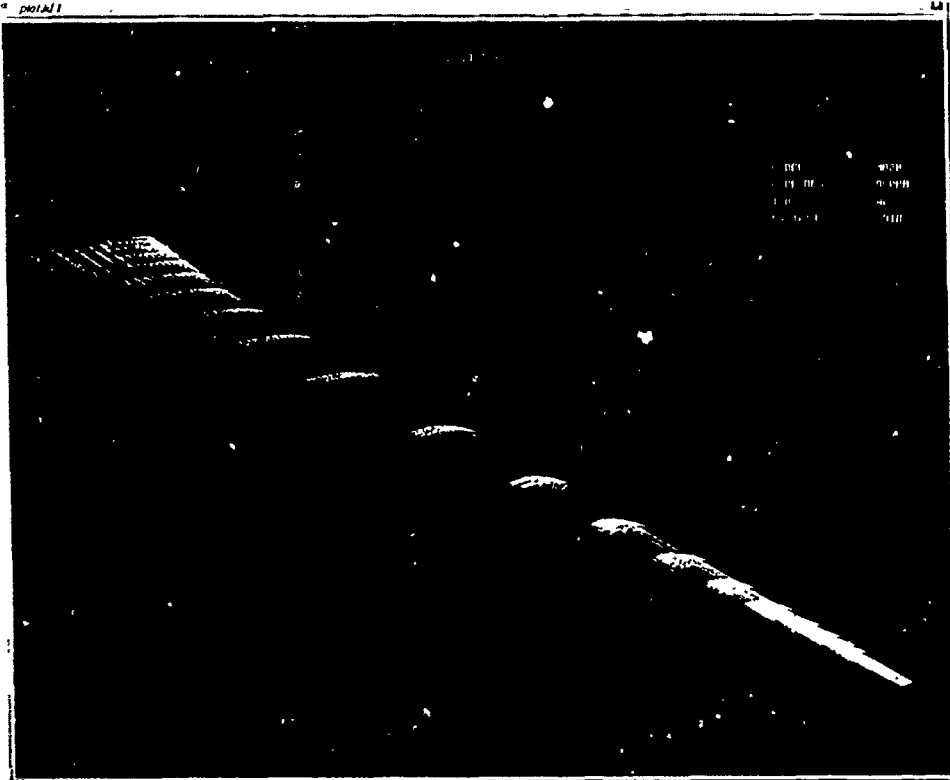


(a) velocity vectors



(b) streamlines

Figure 35. Crossplane flow

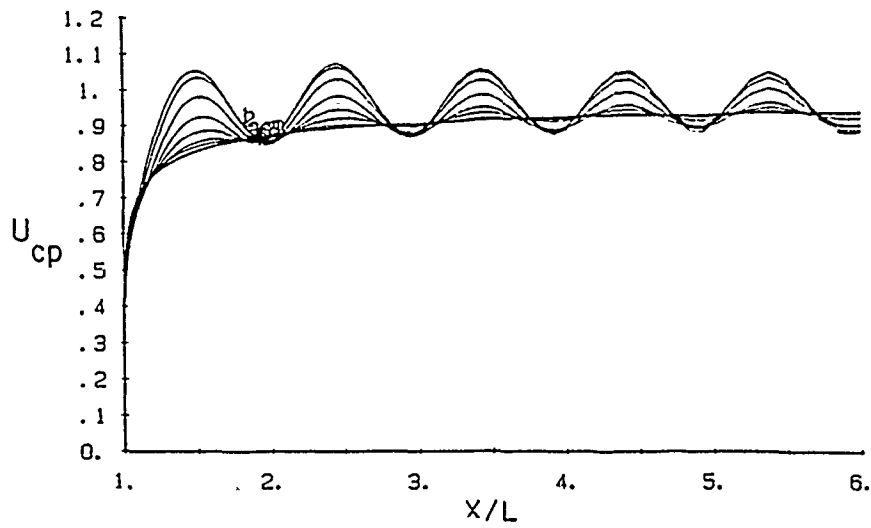


(a) velocity vectors

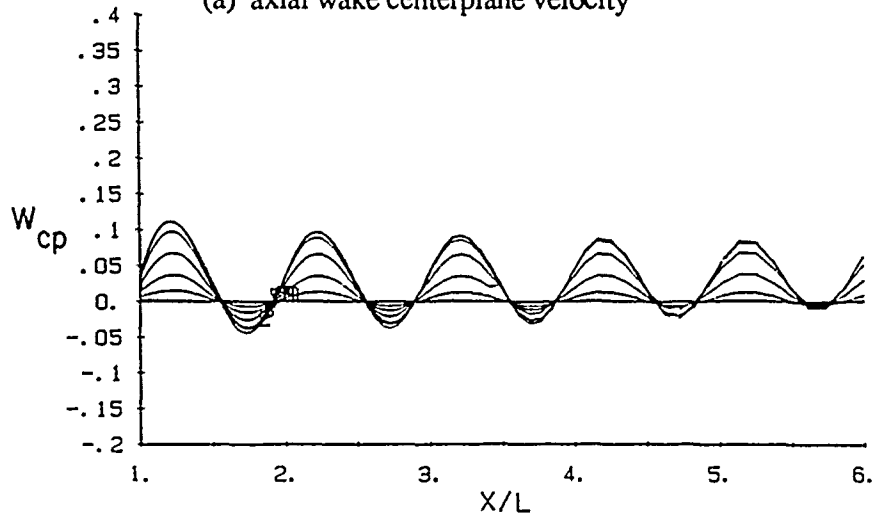


(b) streamlines

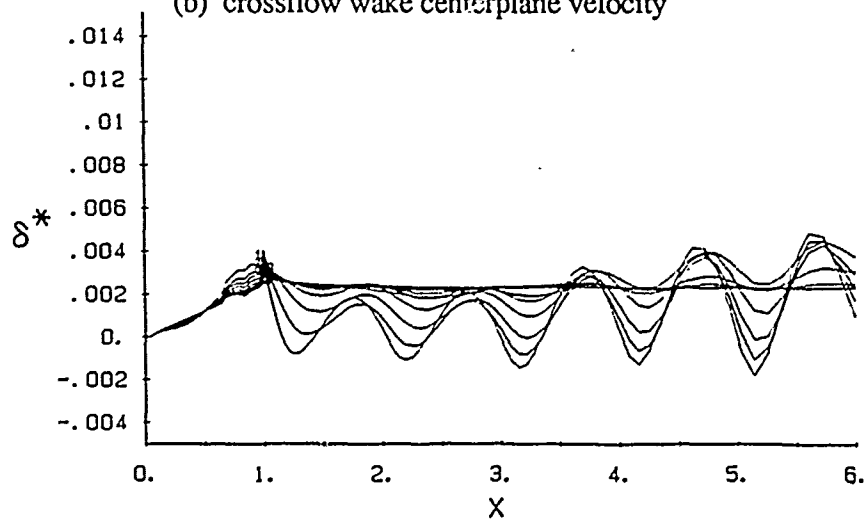
Figure 36. Mean free-surface flow.



(a) axial wake centerplane velocity

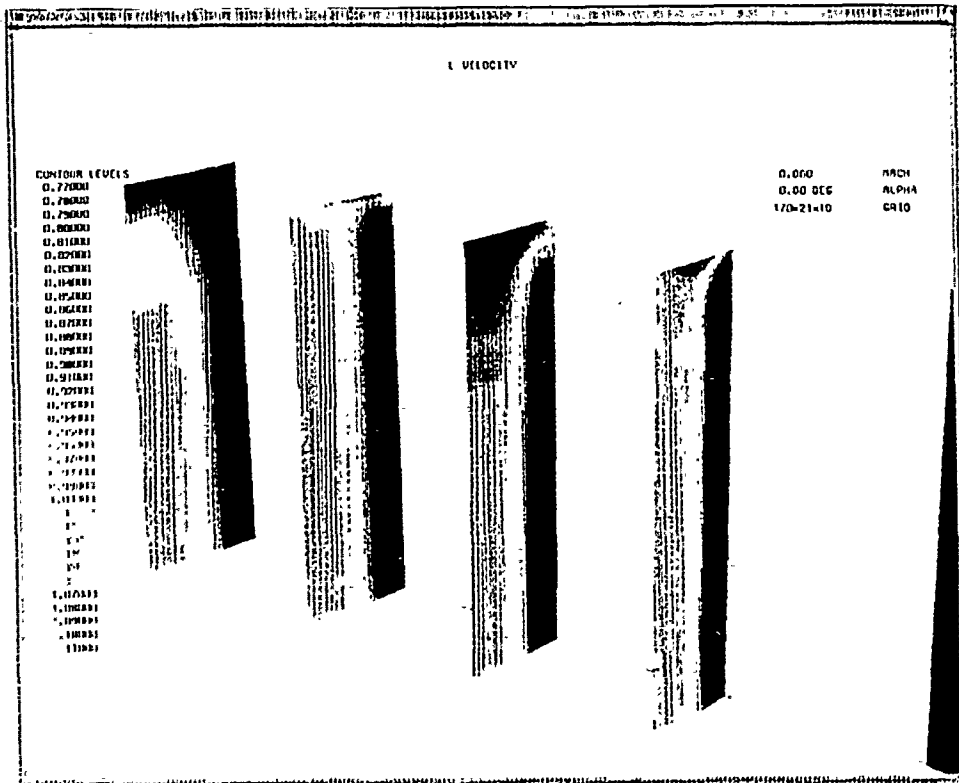


(b) crossflow wake centerplane velocity

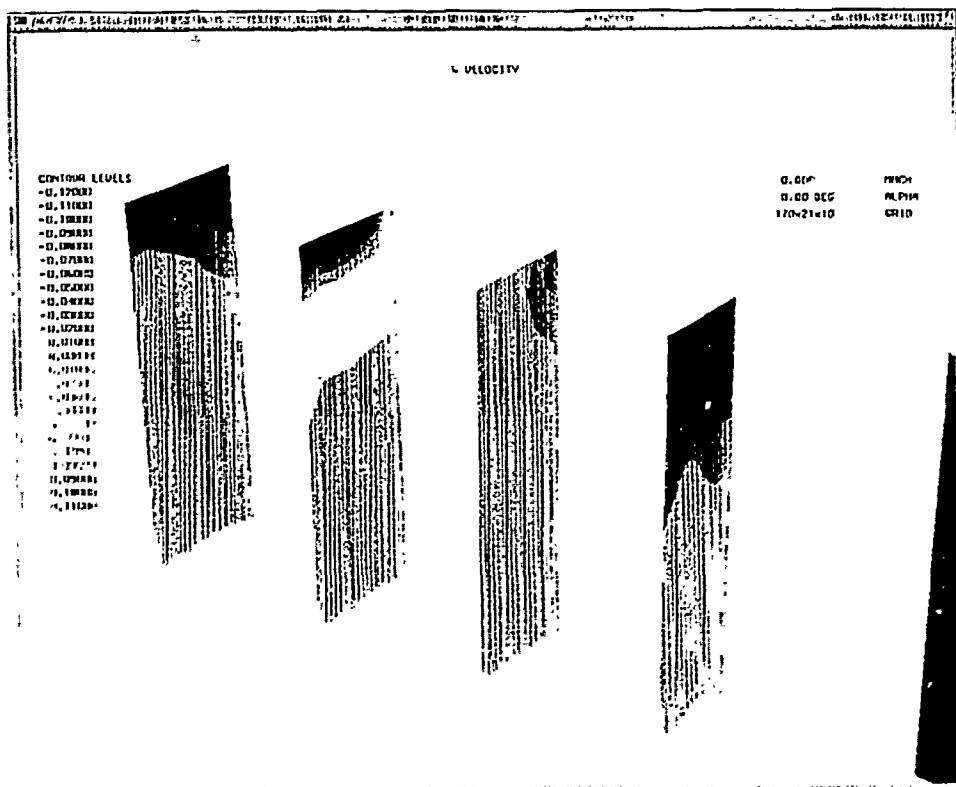


(c) streamwise displacement thickness

Figure 38. Global turbulent solution: $Ak = .11$.

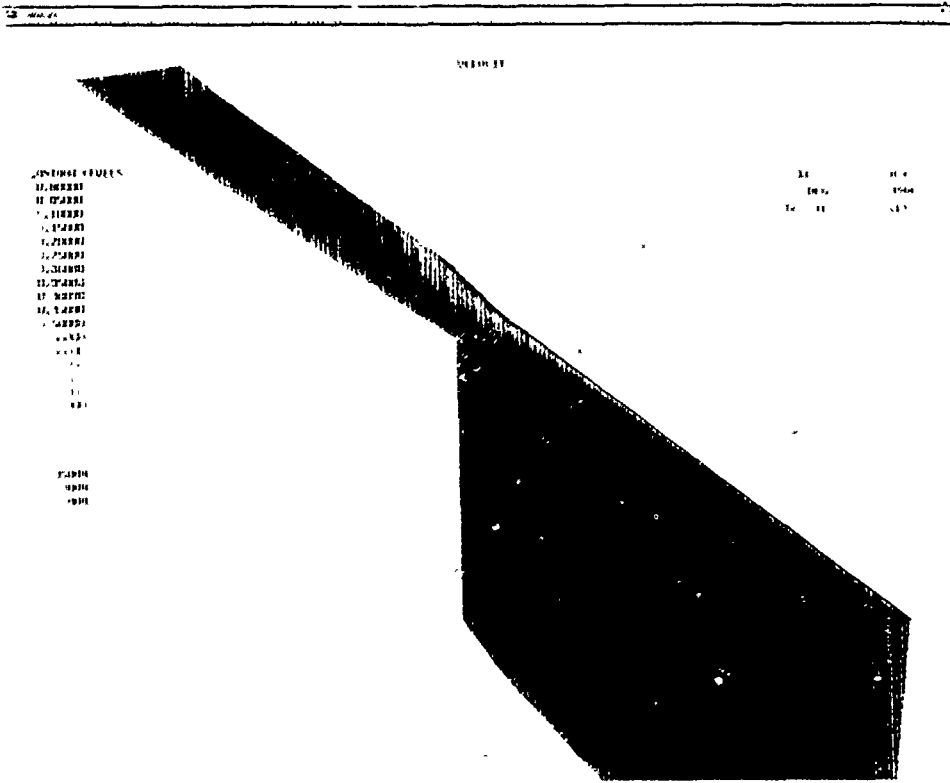


(a) axial velocity

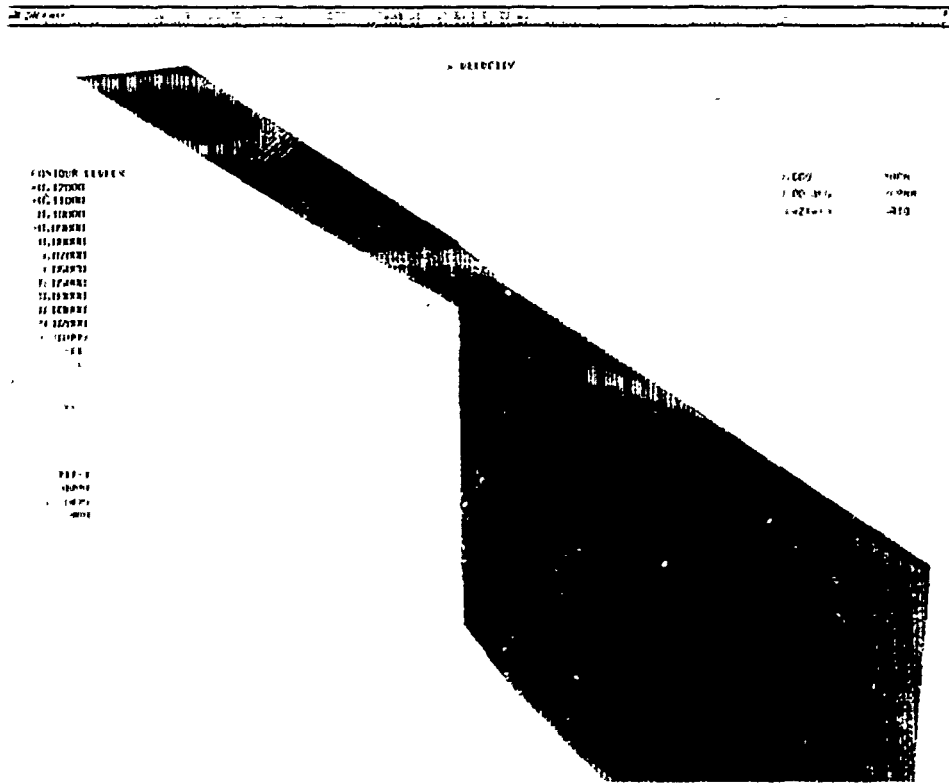


(b) crossflow velocity

Figure 40. Crossplane contours: near- and intermediate-wake regions.

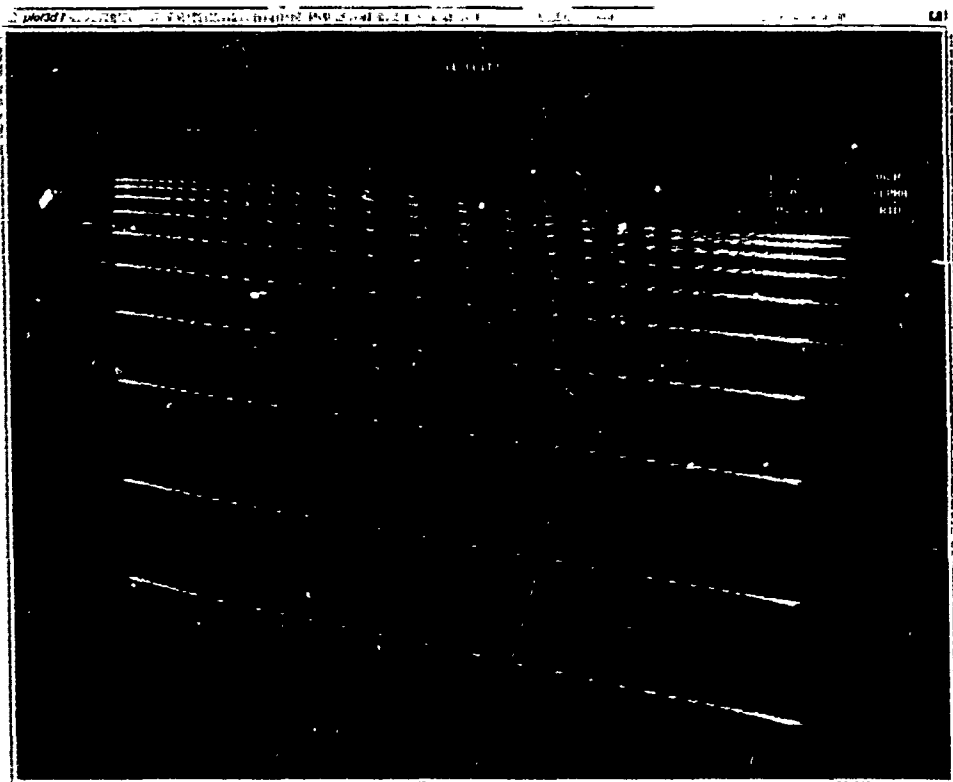


(a) axial velocity

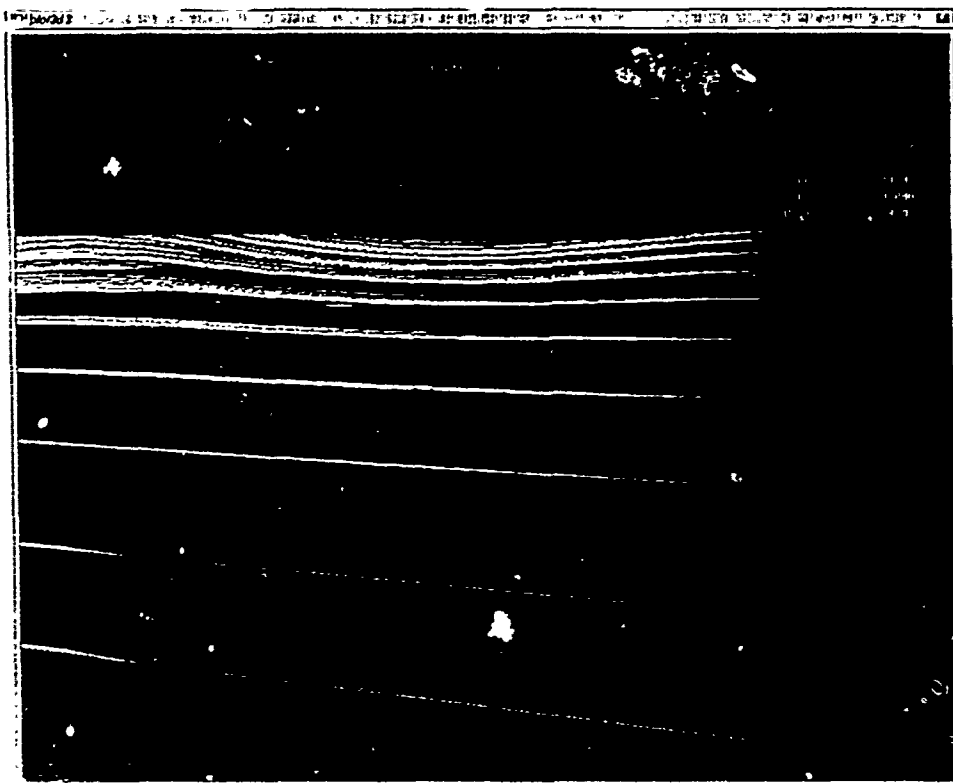


(b) crossflow velocity

Figure 41. Mean free-surface contours: boundary-layer and near- and intermediate-wake regions.

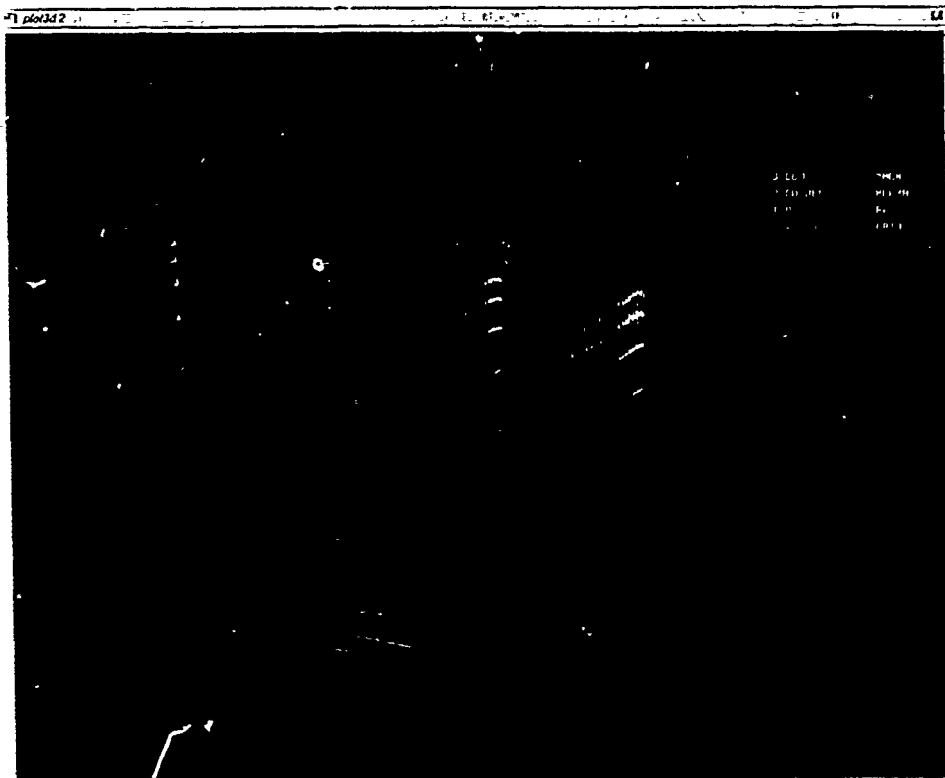


(a) velocity vectors

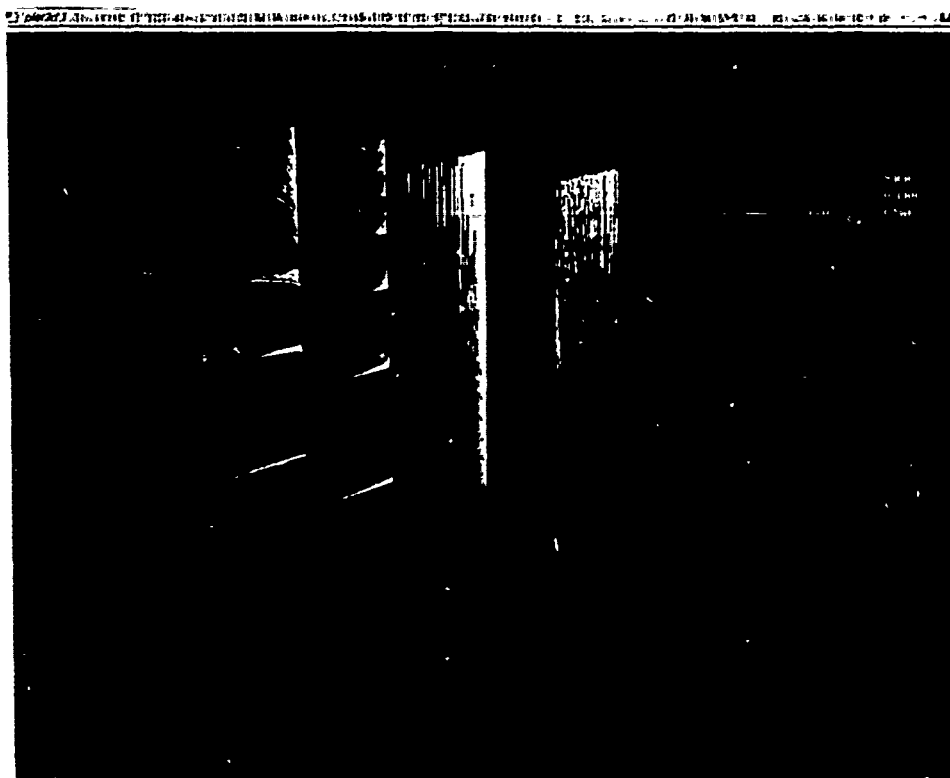


(b) streamlines

Figure 43. Plate and wake centerplane flow.



(a) velocity vectors



(b) streamlines

Figure 44. Crossplane flow.



(a) velocity vectors

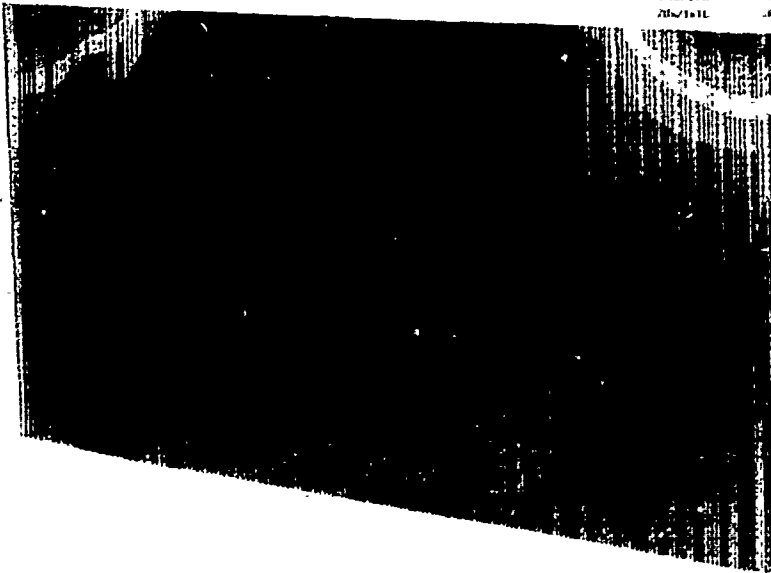


(b) streamlines

Figure 45. Mean free-surface flow.

INFORMATION REPORT

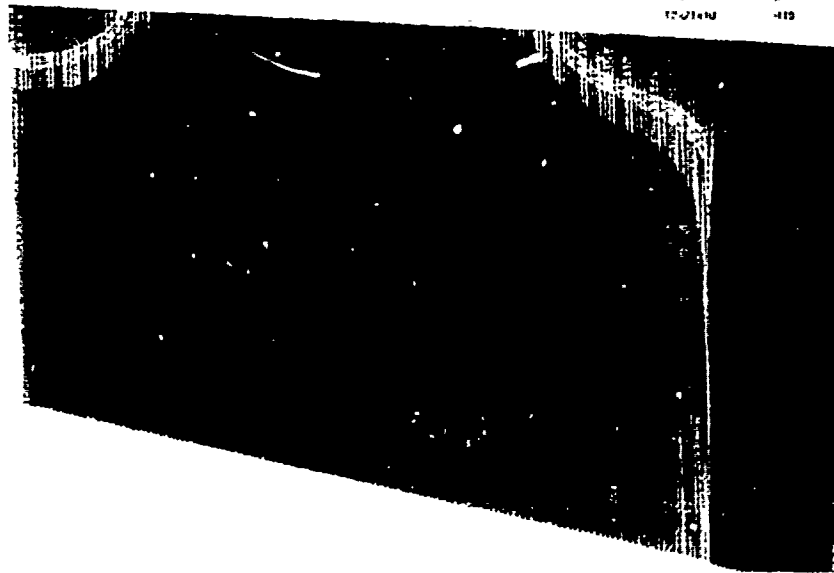
NO. 10000
NO. 10001
NO. 10002
NO. 10003
NO. 10004
NO. 10005
NO. 10006
NO. 10007
NO. 10008
NO. 10009
NO. 10010
NO. 10011
NO. 10012
NO. 10013
NO. 10014
NO. 10015
NO. 10016
NO. 10017
NO. 10018
NO. 10019
NO. 10020
NO. 10021
NO. 10022
NO. 10023
NO. 10024
NO. 10025
NO. 10026
NO. 10027
NO. 10028
NO. 10029
NO. 10030
NO. 10031
NO. 10032
NO. 10033
NO. 10034
NO. 10035
NO. 10036
NO. 10037
NO. 10038
NO. 10039
NO. 10040
NO. 10041
NO. 10042
NO. 10043
NO. 10044
NO. 10045
NO. 10046
NO. 10047
NO. 10048
NO. 10049
NO. 10050



(a) plate surface

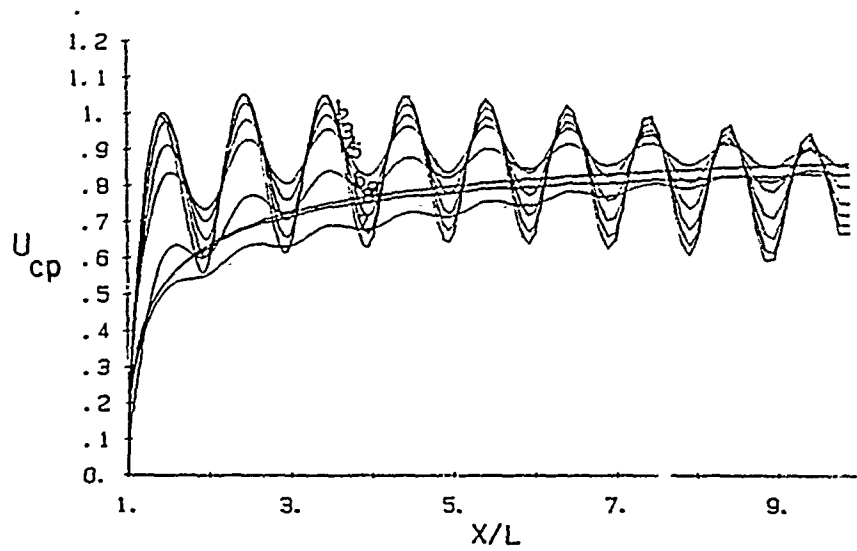
INFORMATION REPORT

NO. 10000
NO. 10001
NO. 10002
NO. 10003
NO. 10004
NO. 10005
NO. 10006
NO. 10007
NO. 10008
NO. 10009
NO. 10010
NO. 10011
NO. 10012
NO. 10013
NO. 10014
NO. 10015
NO. 10016
NO. 10017
NO. 10018
NO. 10019
NO. 10020
NO. 10021
NO. 10022
NO. 10023
NO. 10024
NO. 10025
NO. 10026
NO. 10027
NO. 10028
NO. 10029
NO. 10030
NO. 10031
NO. 10032
NO. 10033
NO. 10034
NO. 10035
NO. 10036
NO. 10037
NO. 10038
NO. 10039
NO. 10040
NO. 10041
NO. 10042
NO. 10043
NO. 10044
NO. 10045
NO. 10046
NO. 10047
NO. 10048
NO. 10049
NO. 10050

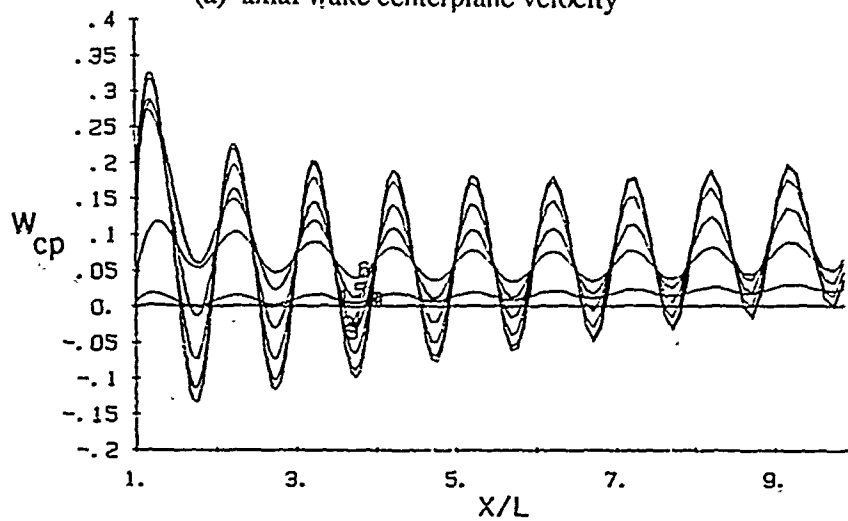


(b) wake centerplane

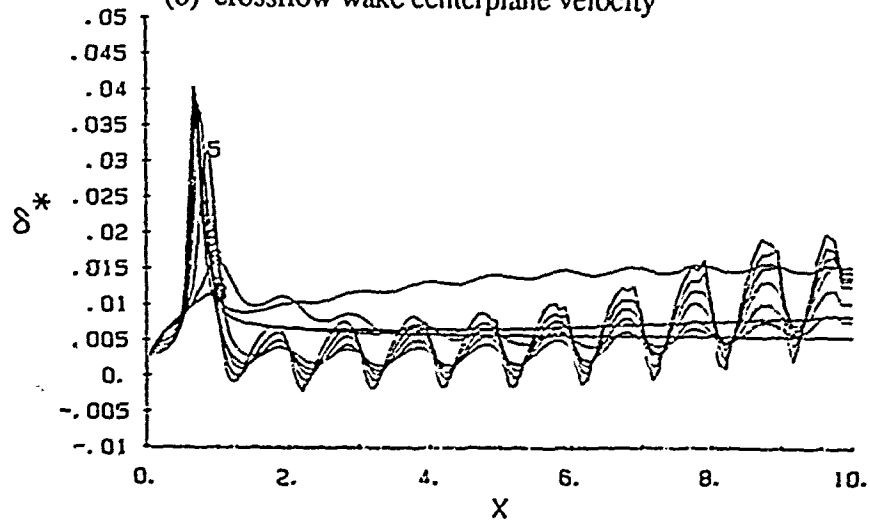
Figure 46. Pressure contours.



(a) axial wake centerplane velocity

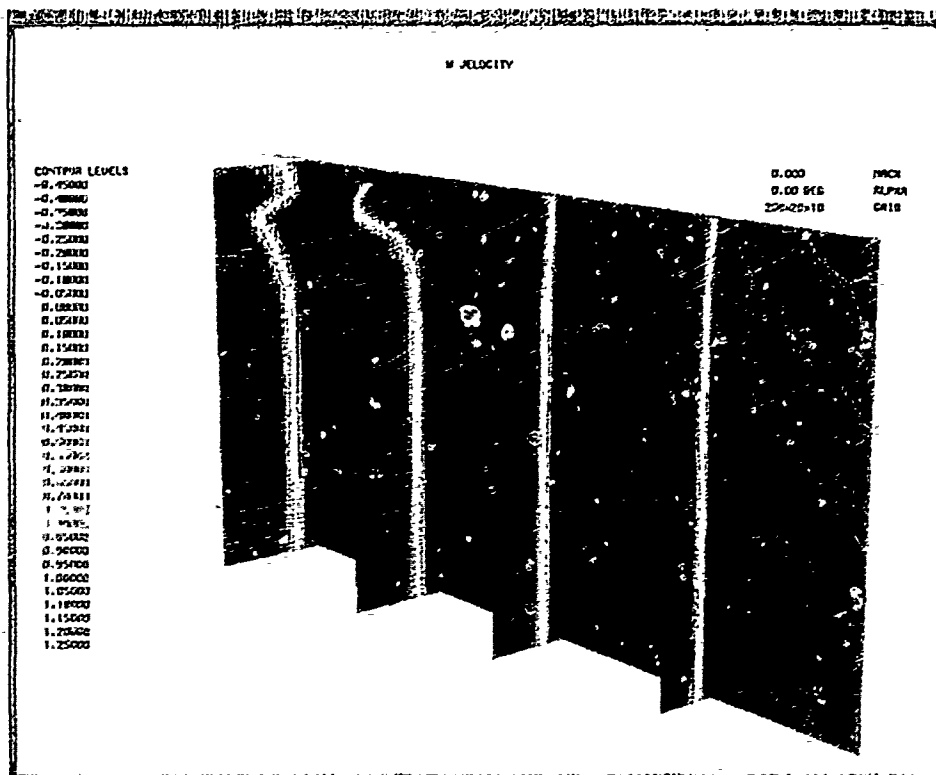


(b) crossflow wake centerplane velocity

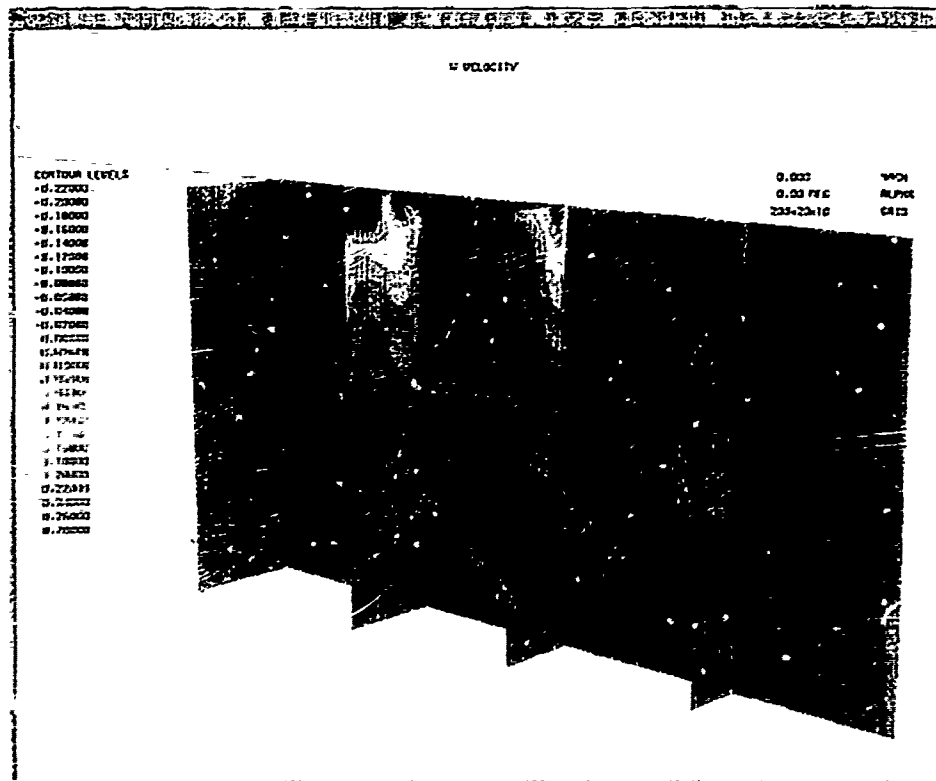


(c) streamwise displacement thickness

Figure 47. Global laminar solution: $Ak = .21$.

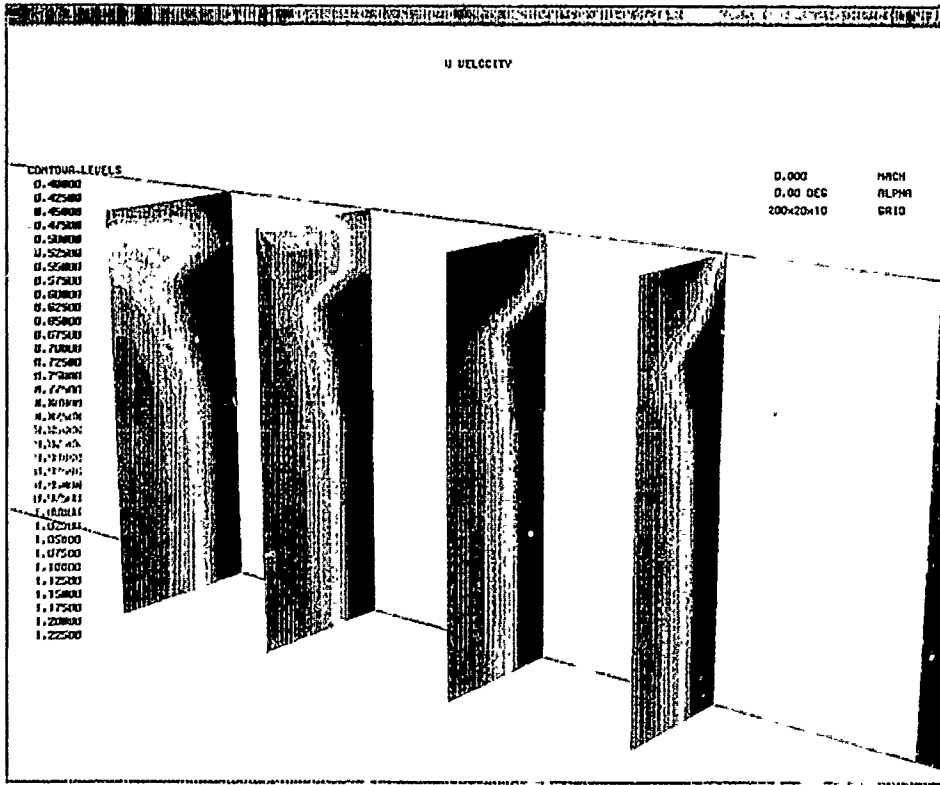


(a) axial velocity

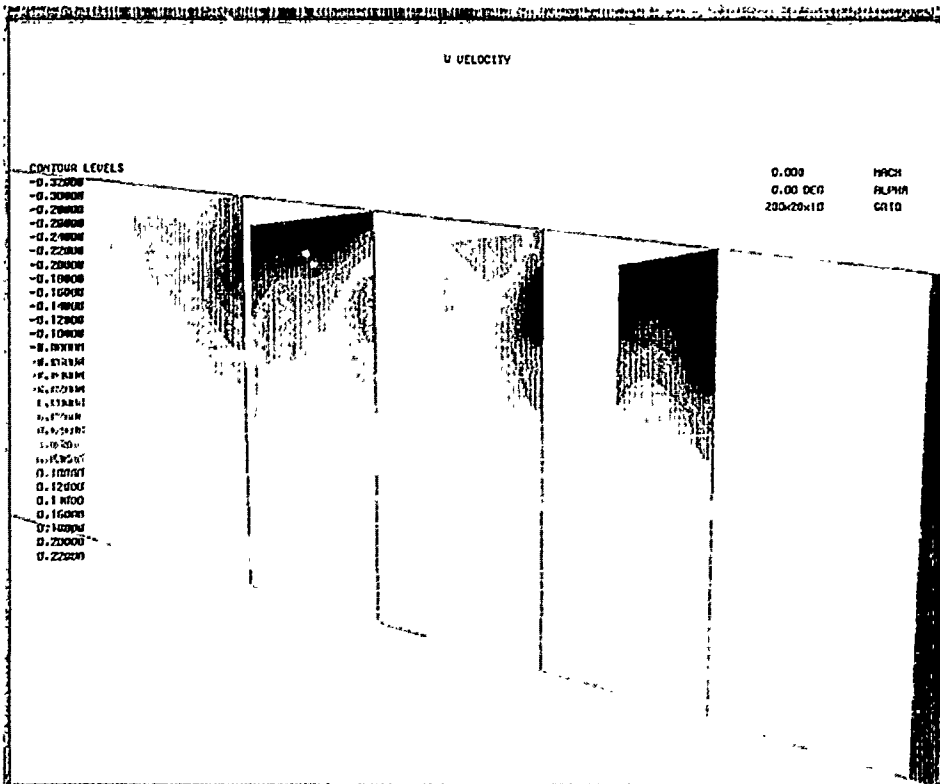


(b) crossflow velocity

Figure 48. Crossplane contours: boundary-layer region.

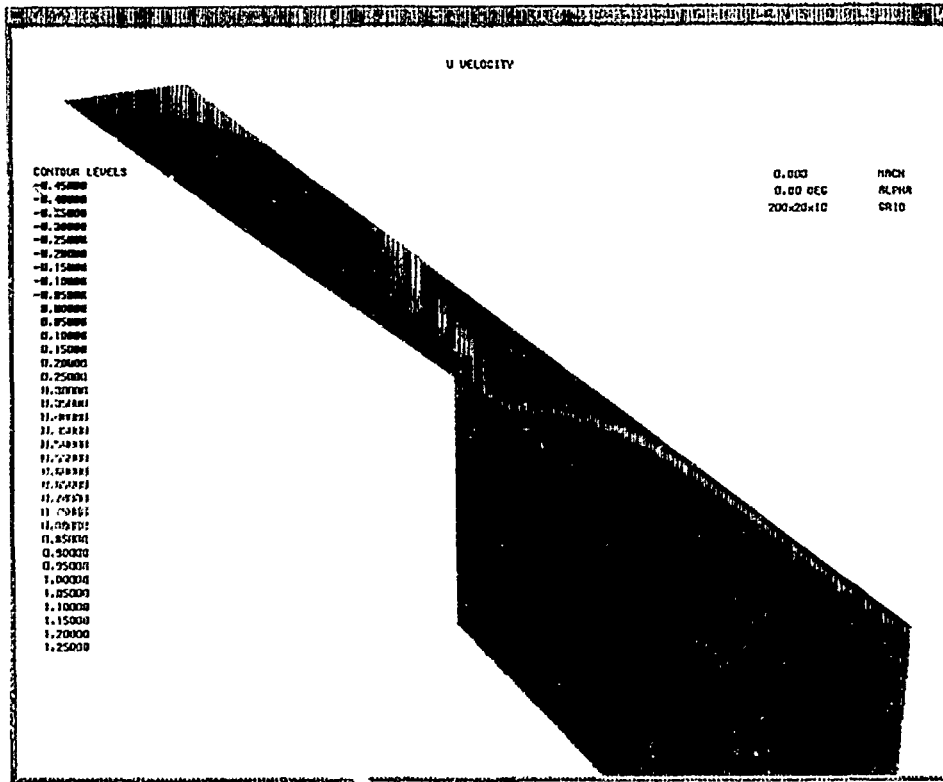


(a) axial velocity

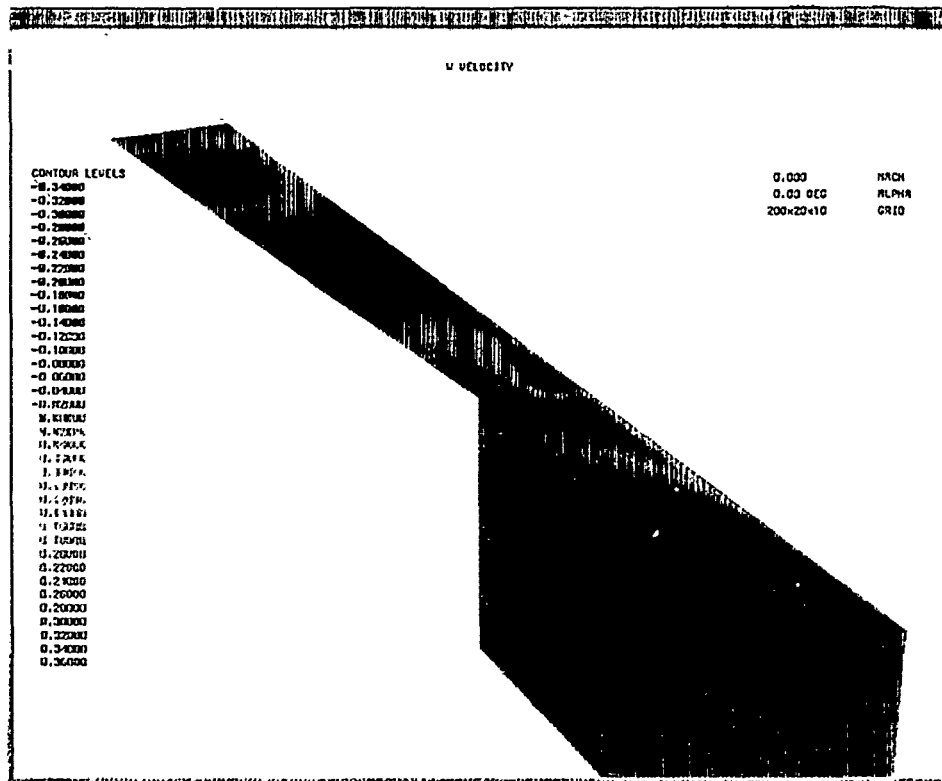


(b) crossflow velocity

Figure 49. Crossplane contours: near- and intermediate-wake regions.

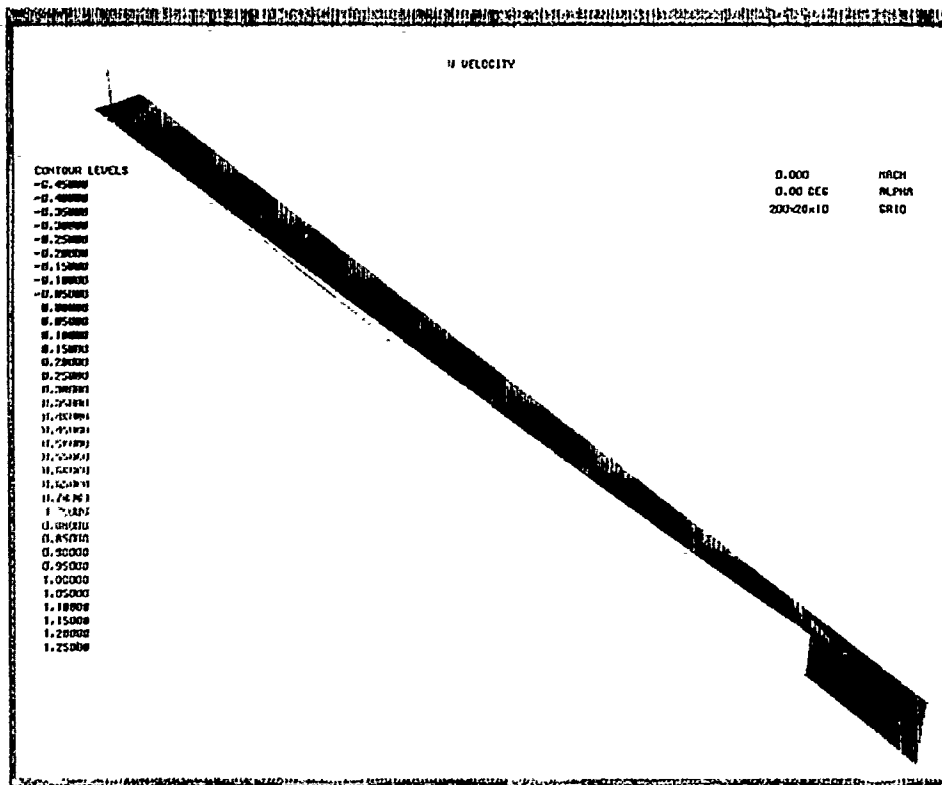


(a) axial velocity

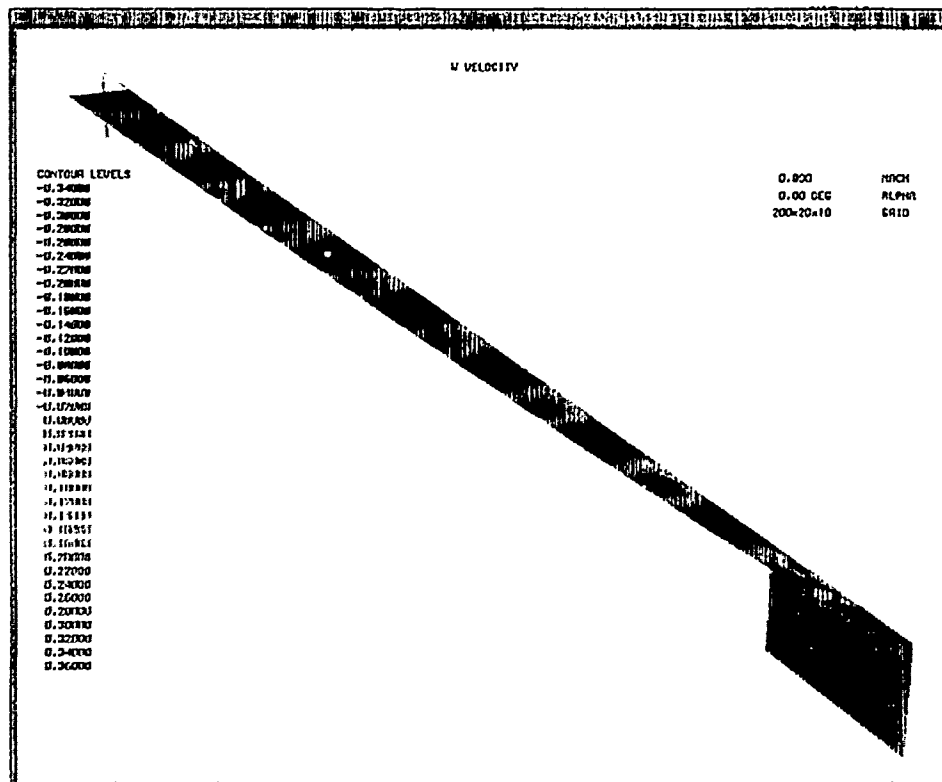


(b) crossflow velocity

Figure 50. Mean free-surface contours: boundary-layer and near- and intermediate-wake regions.

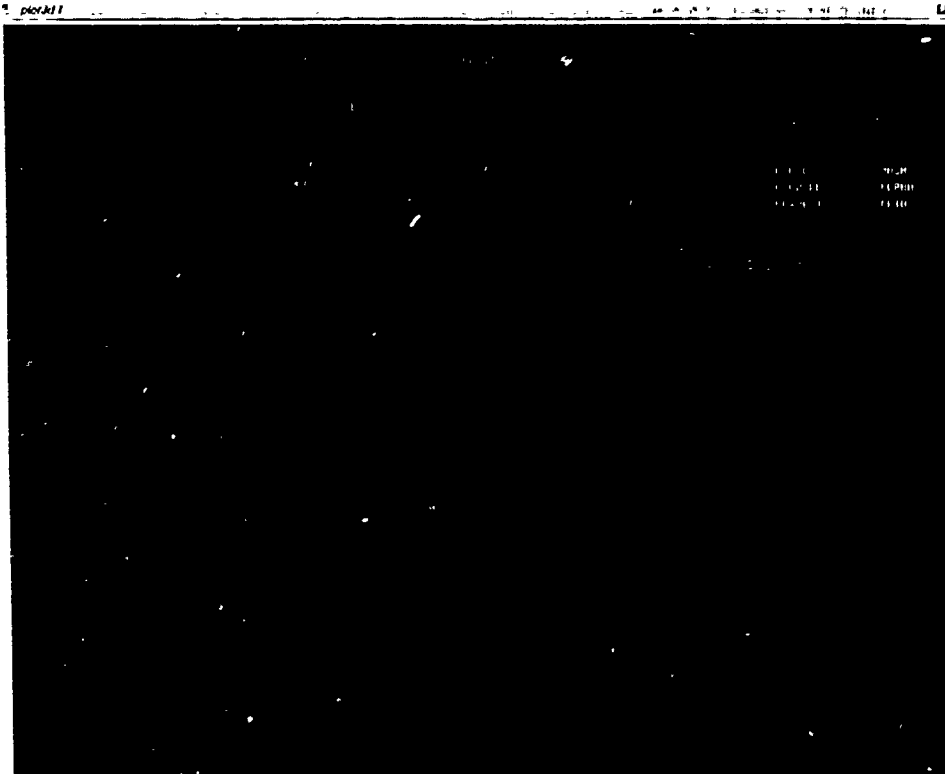


(a) axial velocity

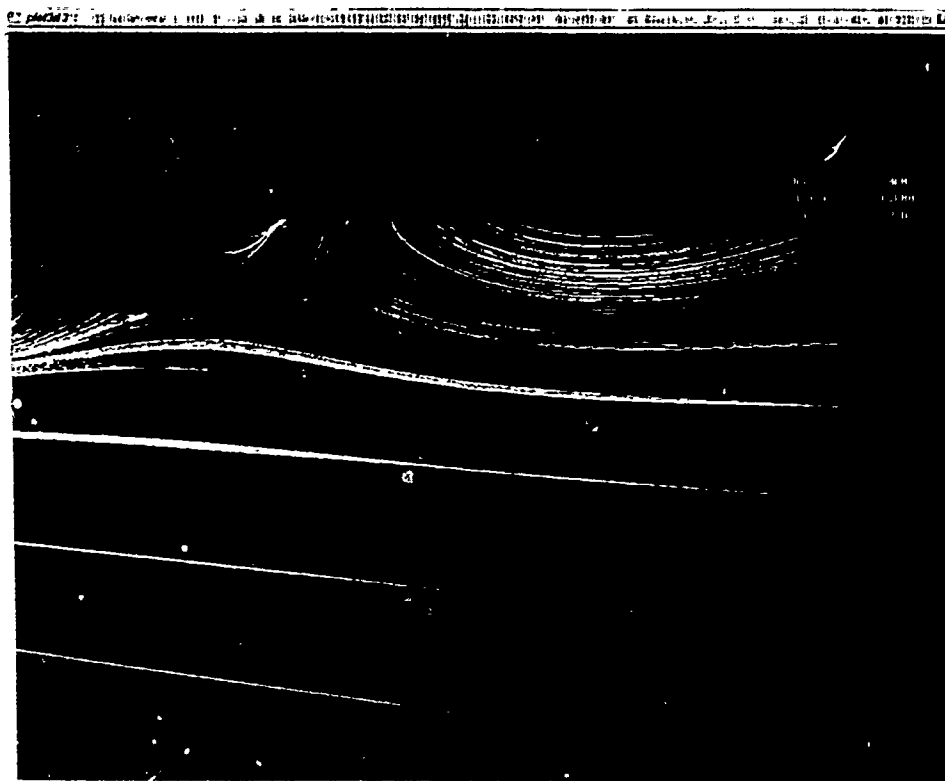


(b) crossflow velocity

Figure 51. Mean free-surface contours: complete solution domain.



(a) velocity vectors

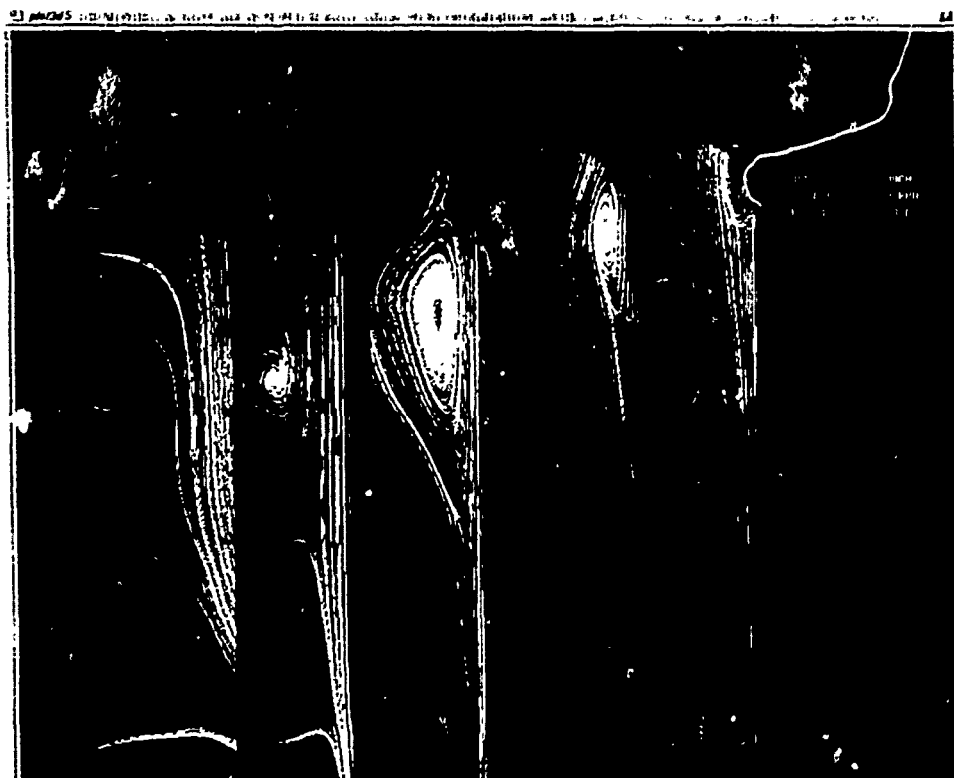


(b) streamlines

Figure 52. Plate and wake centerplane flow.

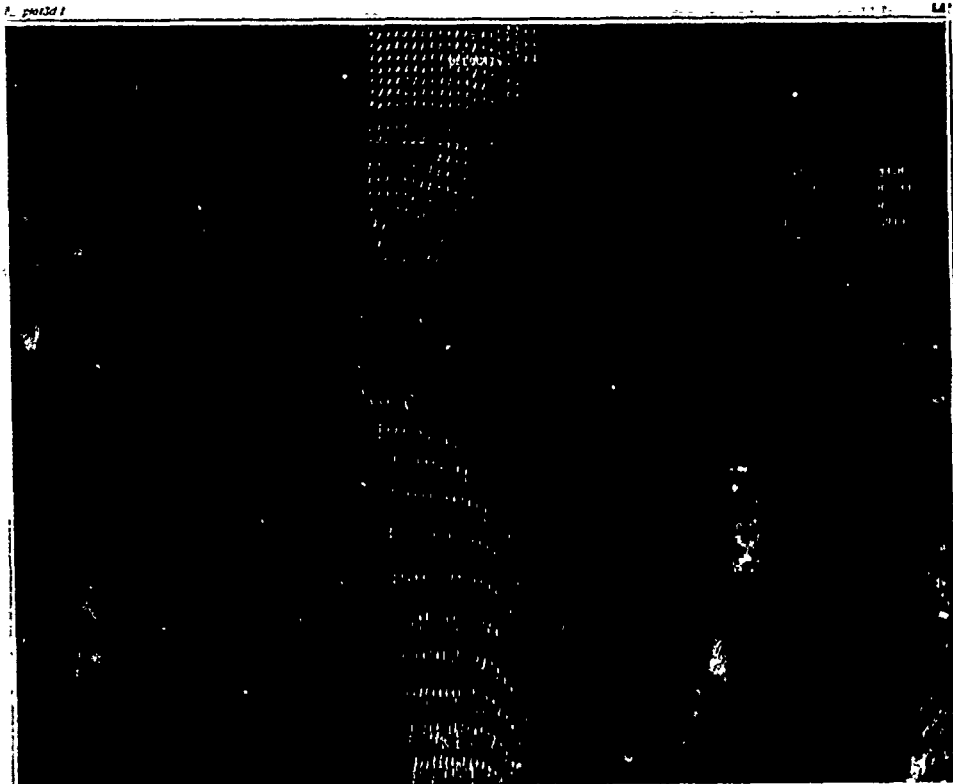


(a) velocity vectors

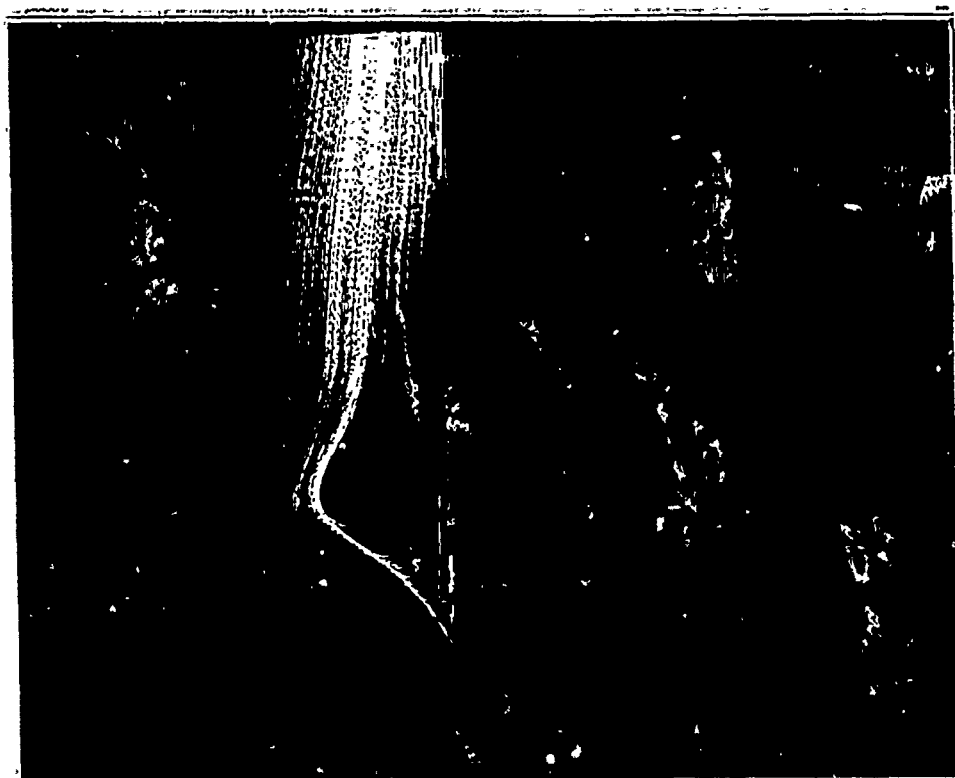


(b) streamlines

Figure 53. Crossplane flow.

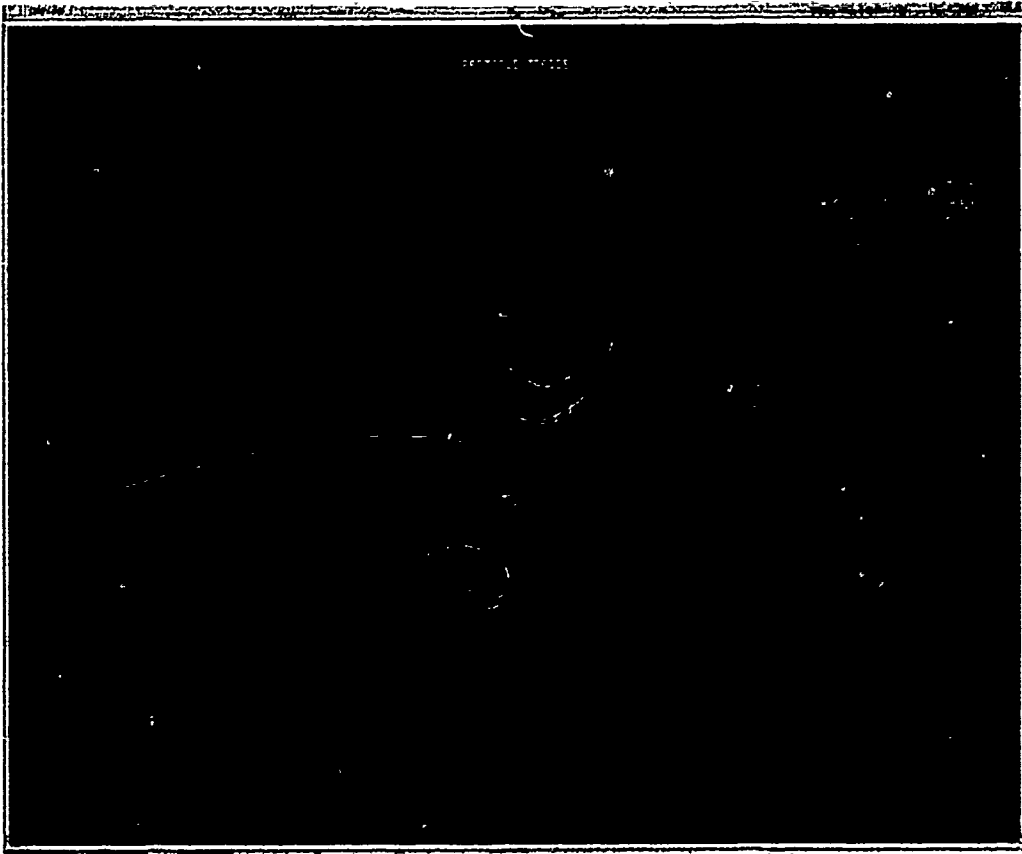


(a) velocity vectors

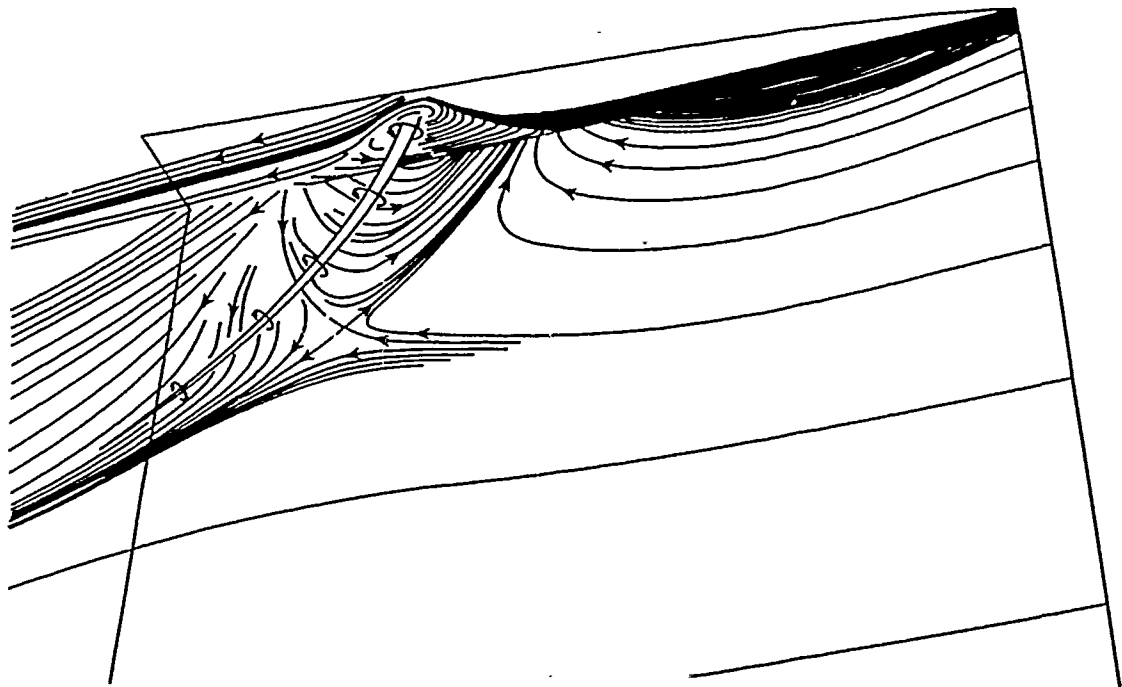


(b) streamlines

Figure 54. Mean free-surface flow.



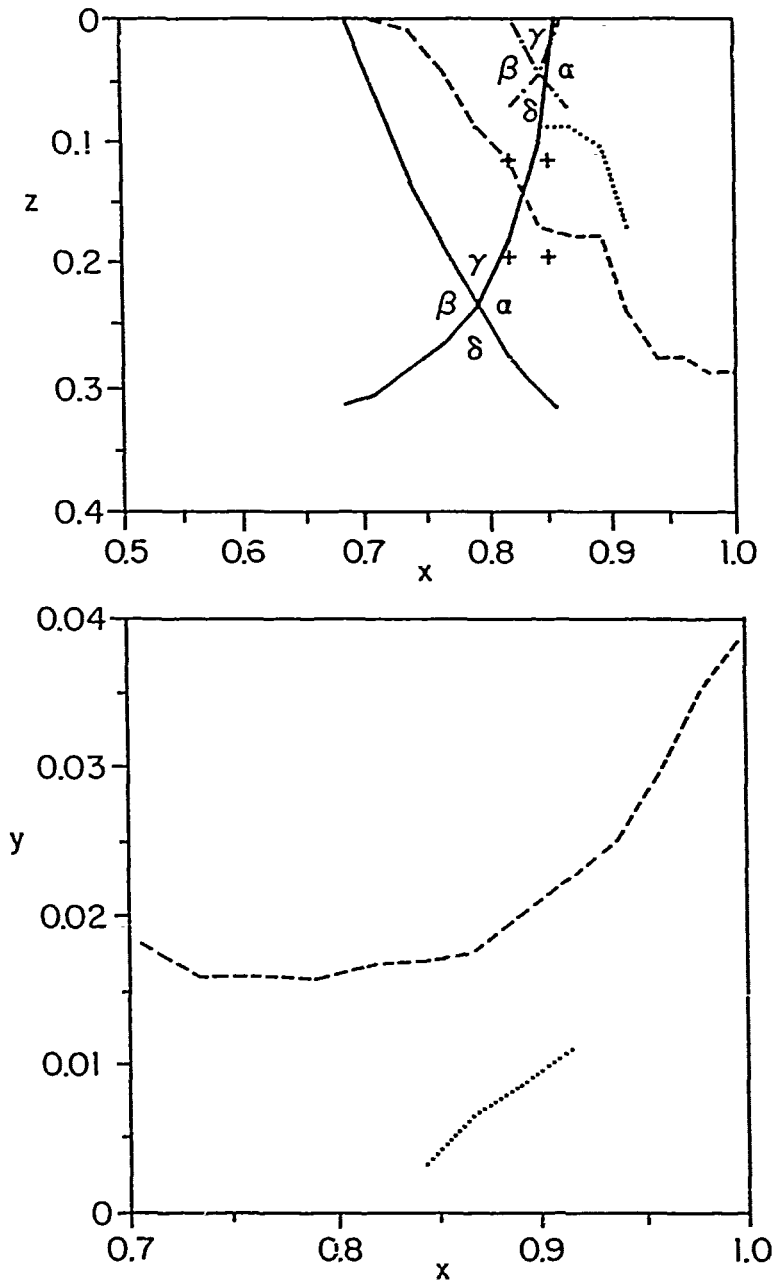
(a) Particle traces in separation region.



(b) Limiting streamlines on the plate and the free surface, and vortex skeleton near the separation point ($Ak=.21$).

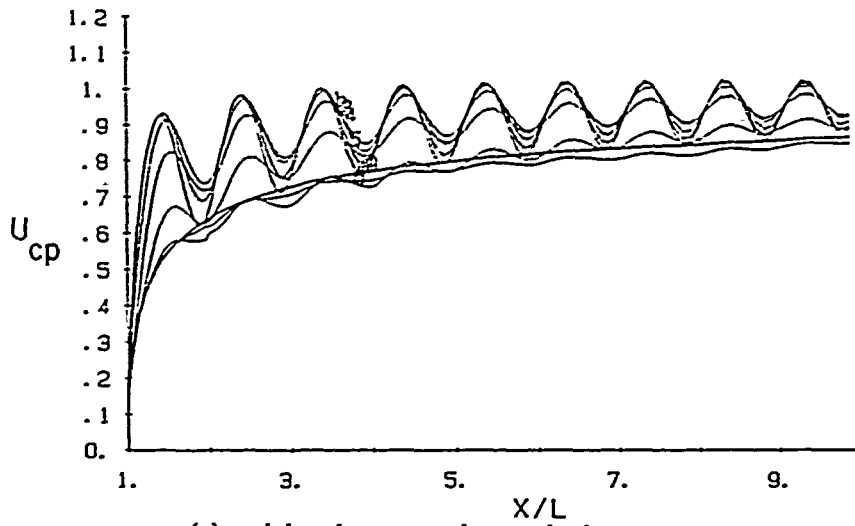
Figure 56. Flow pattern in separation region.

Ak	Vortex Center	Separation Line
0.11	- - - - -
0.21	- - - - -	—————
+	Locations for particle trajectories	

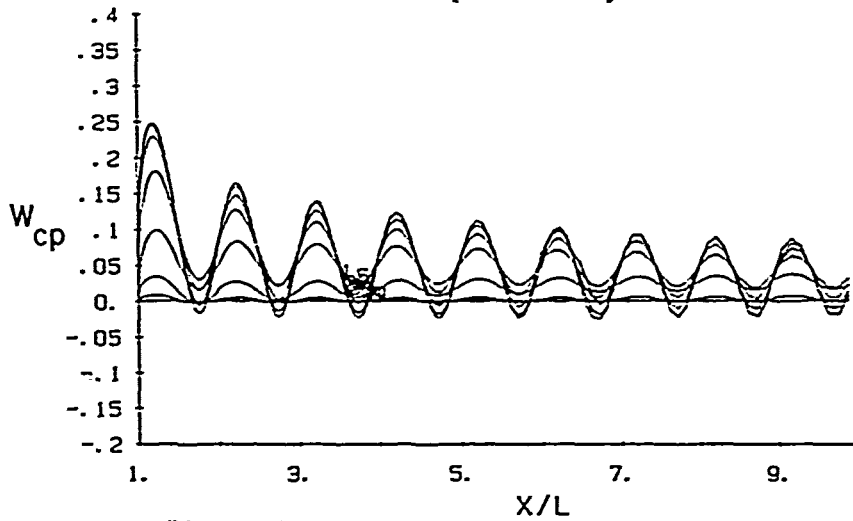


(c) Locations of separation lines, vortex center, and particle trajectories.

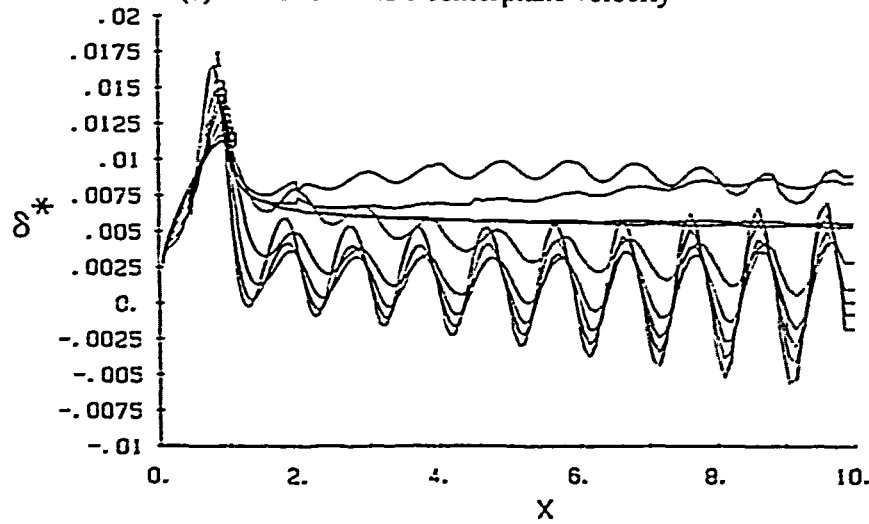
Figure 56. (concluded).



(a) axial wake centerplane velocity

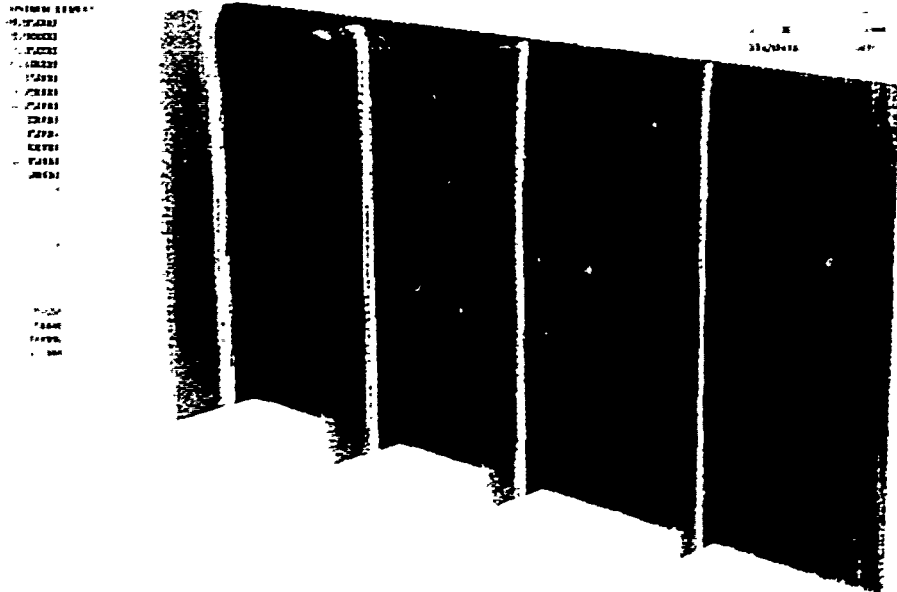


(b) crossflow wake centerplane velocity

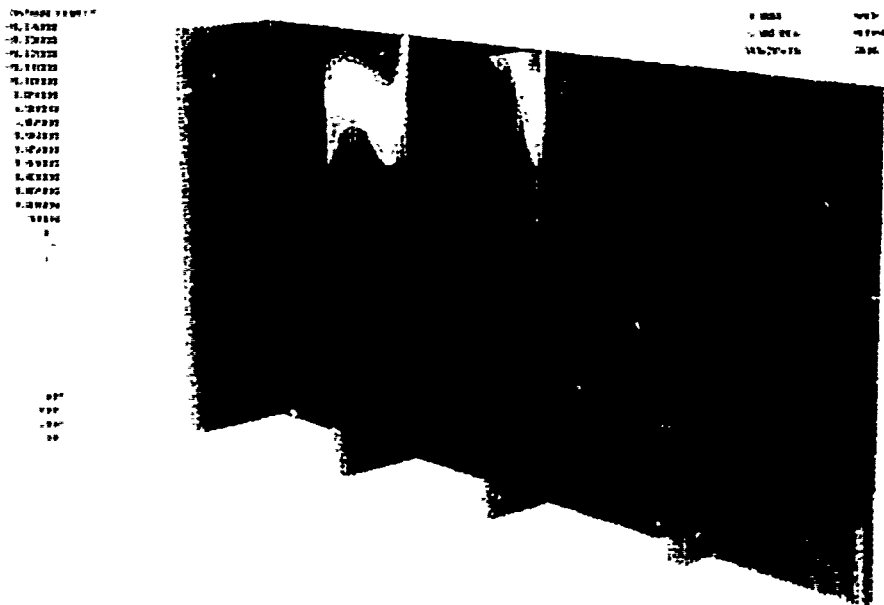


(c) streamwise displacement thickness

Figure 57 Global laminar solution: $Ak = .11$.



(a) axial velocity



(b) crossflow velocity

Figure 58. Crossplane contours: boundary-layer region.

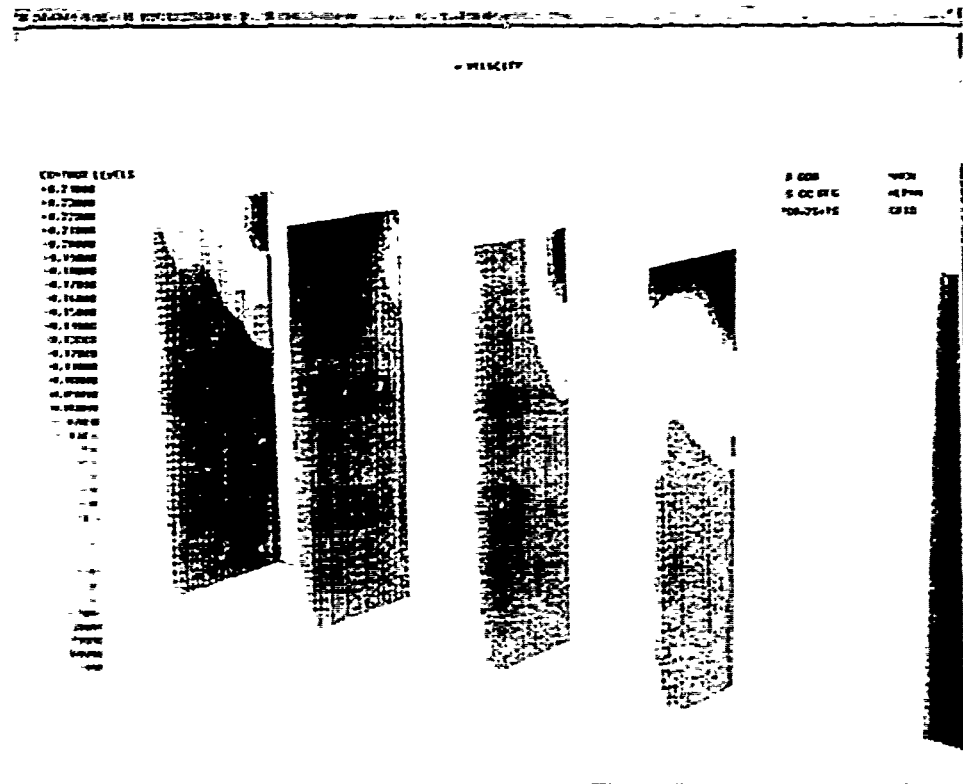
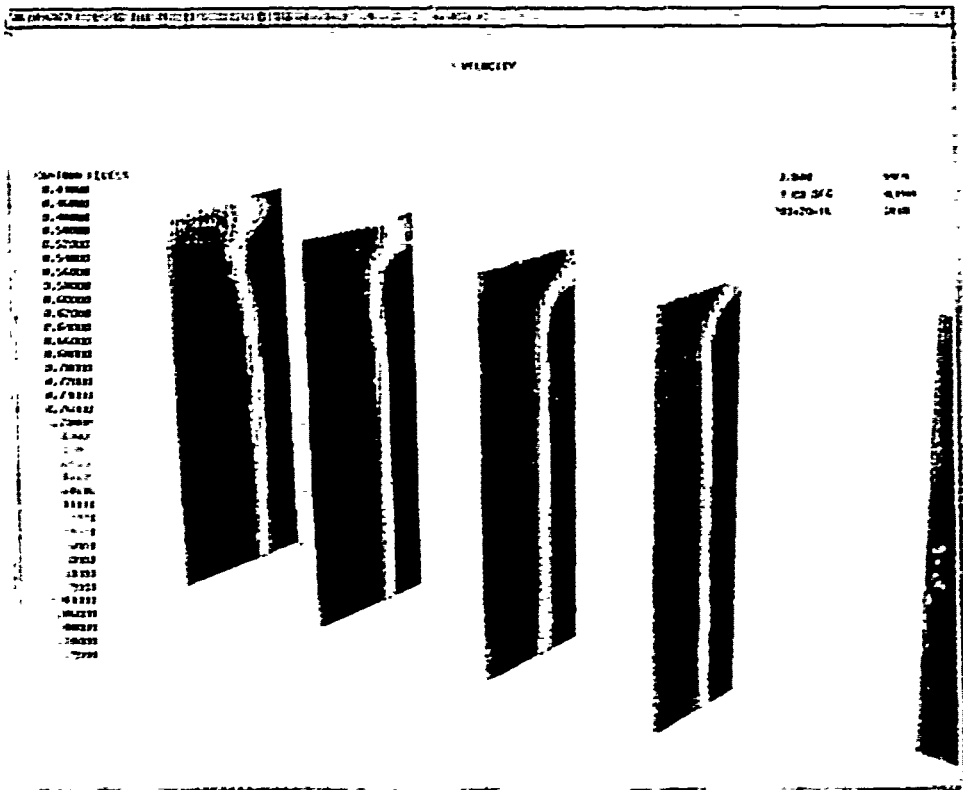
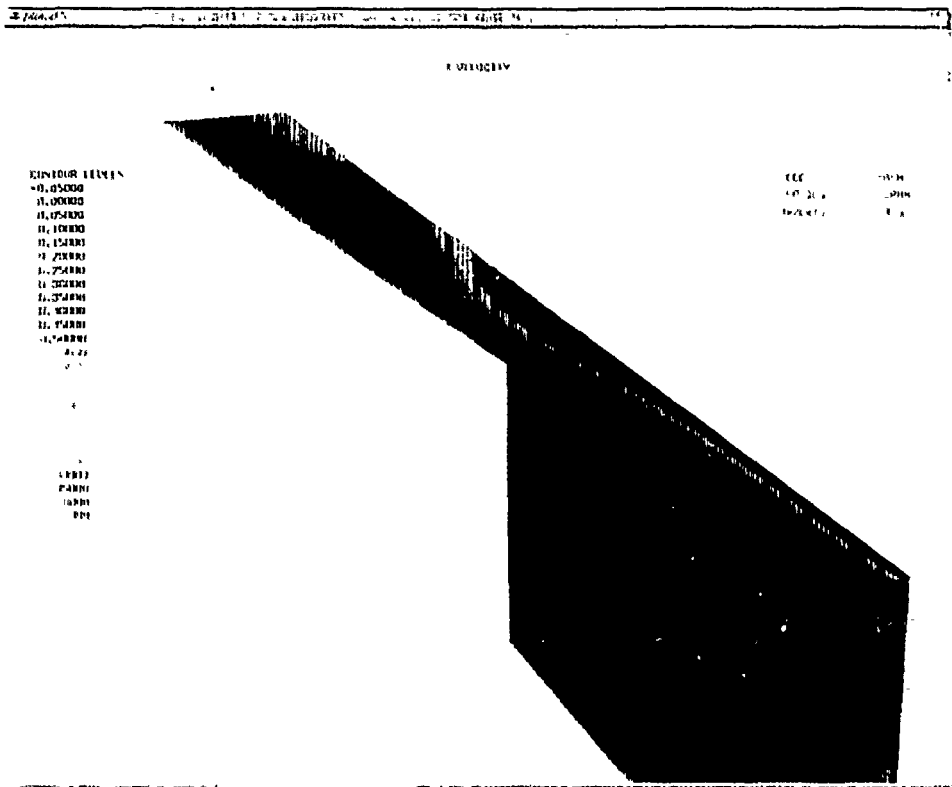
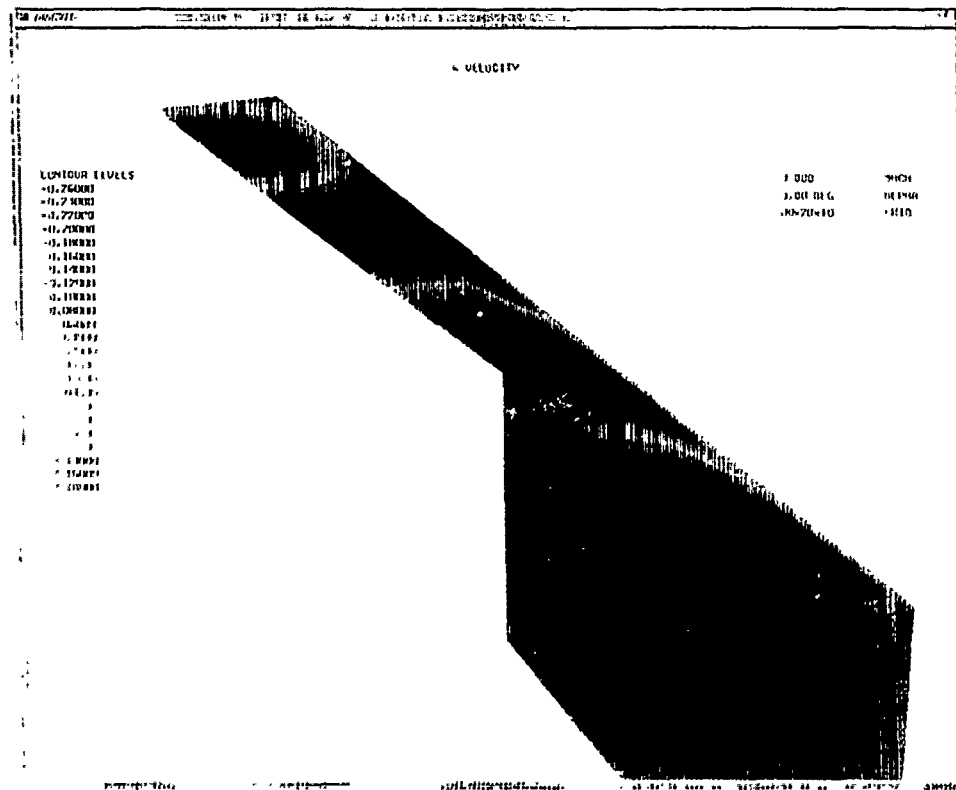


Figure 59. Crossplane contours: near- and intermediate-wake regions.

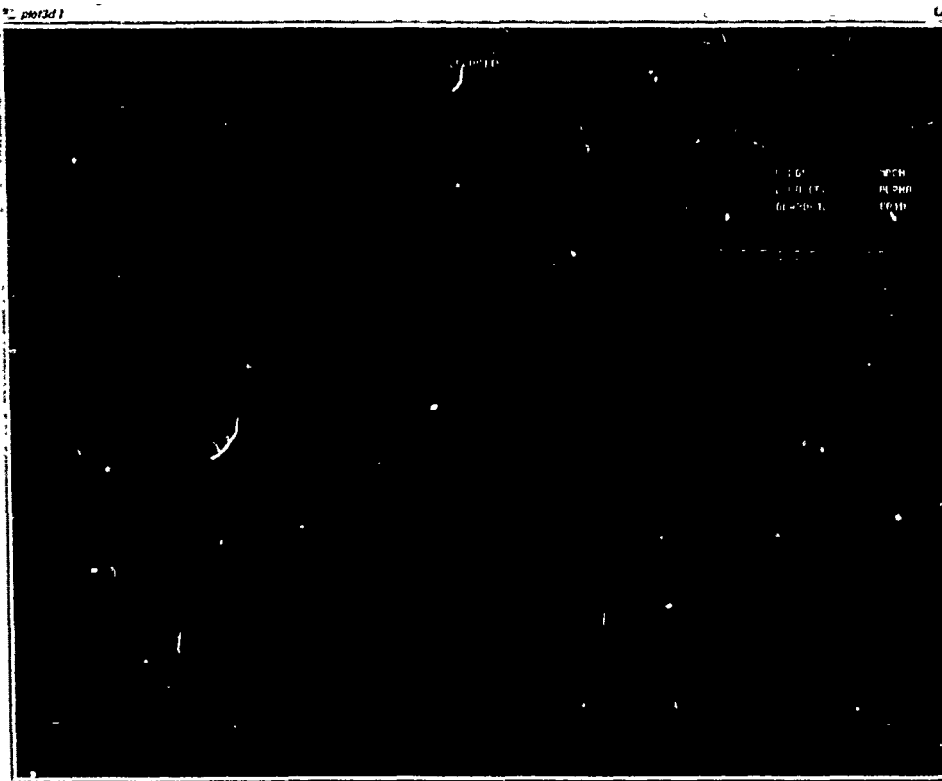


(a) axial velocity

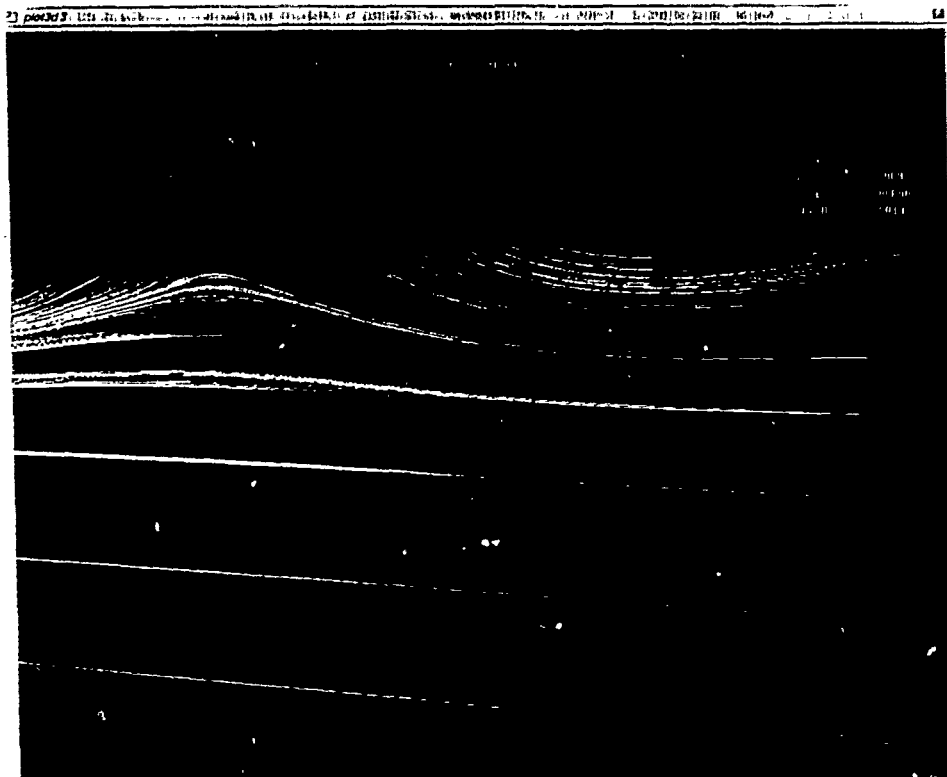


(b) crossflow velocity

Figure 60. Mean free-surface contours: boundary-layer and near- and intermediate-wake regions.

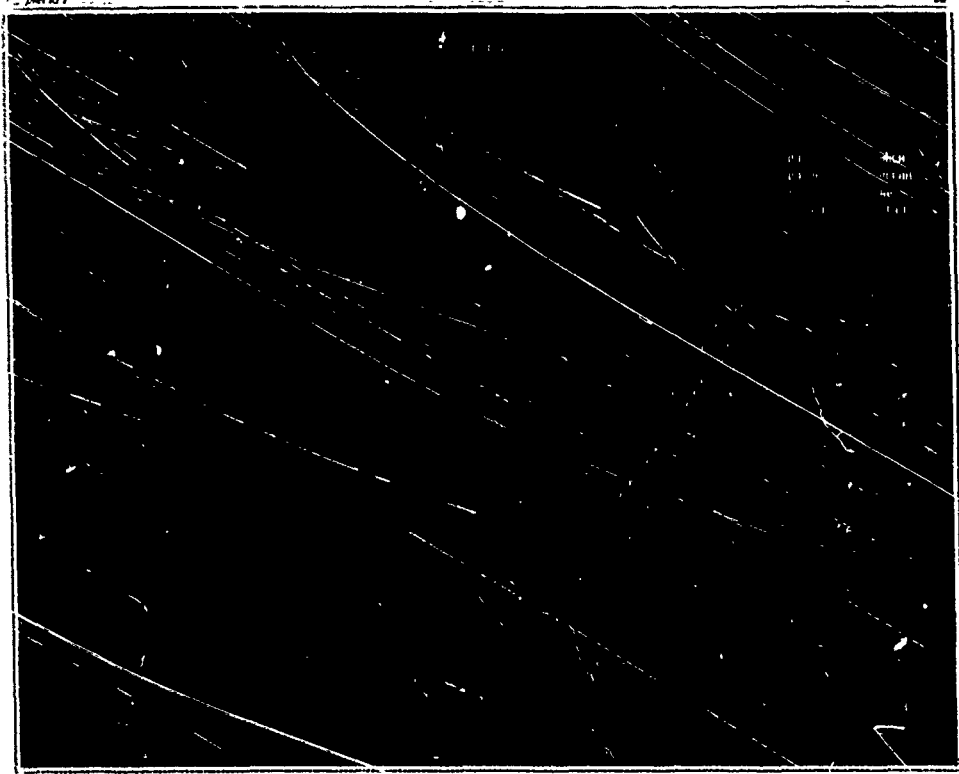


(a) velocity vectors

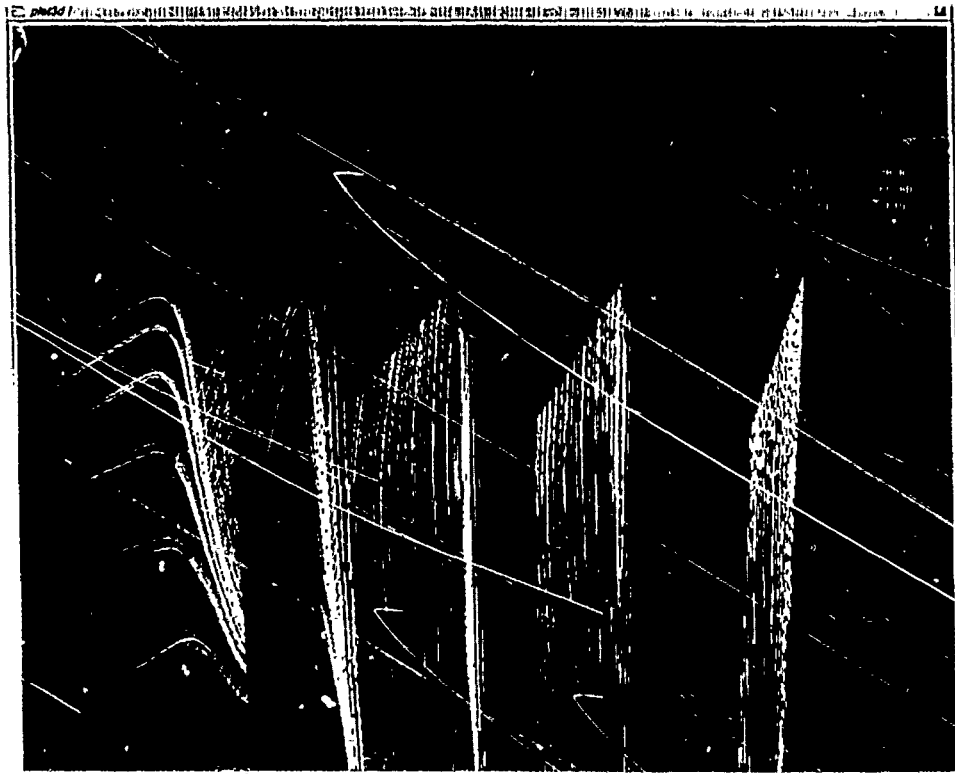


(b) streamlines

Figure 62. Plate and wake centerplane flow.

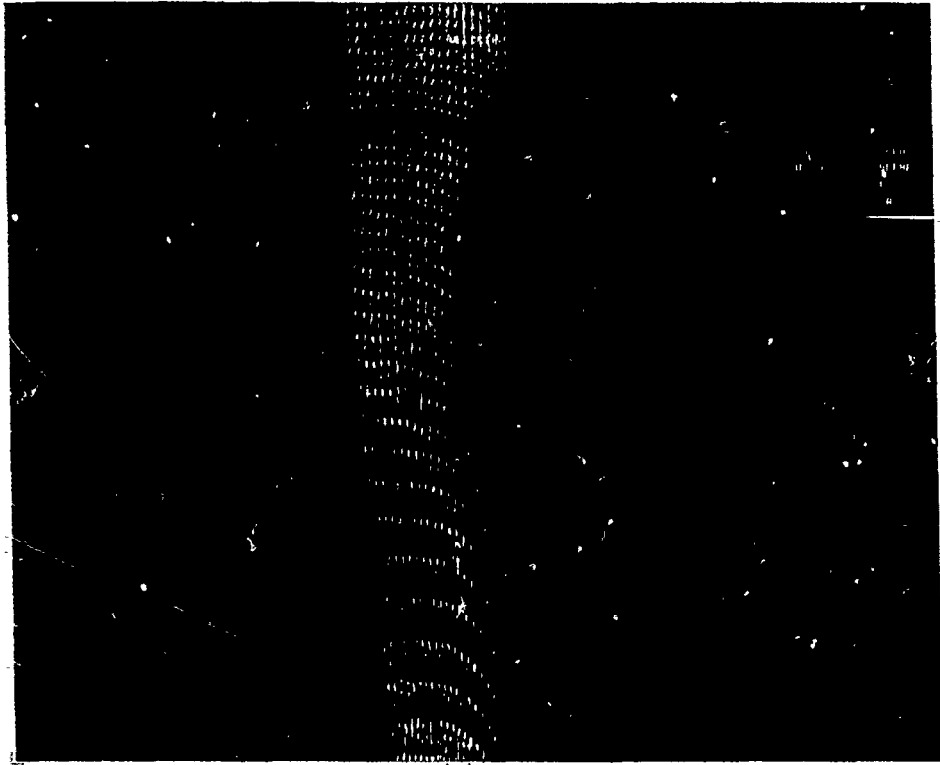


(a) velocity vectors

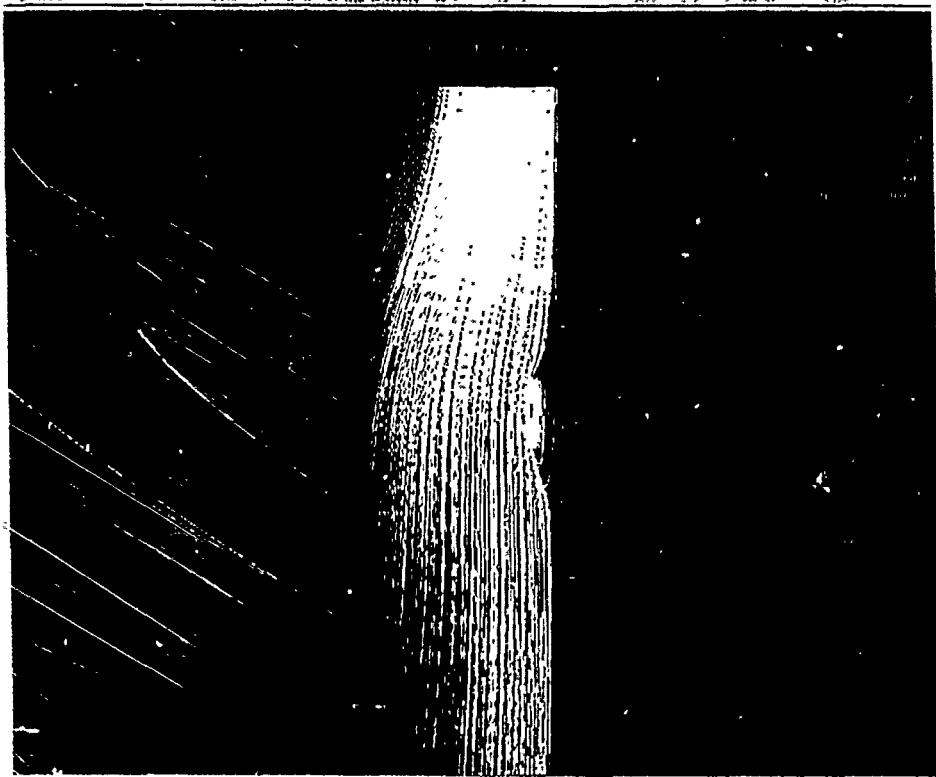


(b) streamlines

Figure 63. Crossplane flow.



(a) velocity vectors



(b) streamlines

Figure 64. Mean free-surface flow.

